Journal of Materials Chemistry A

ROYAL SOCIETY OF CHEMISTRY

REVIEW

View Article Online
View Journal | View Issue

Cite this: *J. Mater. Chem. A*, 2022, **10**, 475

Heterostructured hybrids of metal–organic frameworks (MOFs) and covalent–organic frameworks (COFs)

Chuanpan Guo, Fenghe Duan, Shuai Zhang, Linghao He, Minghua Wang, Junli Chen, Jianqiang Zhang, Qiaojuan Jia, Zhihong Zhang * and Miao Du *

Metal–organic frameworks (MOFs) and covalent–organic frameworks (COFs) with highly ordered crystalline structures show numerous advantages such as large surface areas, structural tunability, well-defined accessible pores, and thermo/chemical stability. Thus, combining different types of MOFs and COFs into one system can generate abundant MOF/COF-based hybrid nanomaterials with superior performances. In comparison to single MOFs or COFs, MOF/COF heterostructures show fantastic properties due to the synergistic effects of their different components. Accordingly, in recent years, MOF/COF-based heterostructures have received increasing attention and rapid advancements, exhibiting a broad range of potential applications in gas sorption and separation, catalysis, energy transfer, biomedicine, *etc.* Herein, the design principles, assembly mechanisms, synthetic approaches, and applications of different MOF/COF-based hybrids are summarized in detail. The current challenges and future perspectives for MOF/COF-based hybrids are also discussed. This review can provide deep insights into MOF/COF-based heterostructures, which will be helpful for the further development of these hybrid materials with advanced applications.

Received 16th July 2021
Accepted 23rd November 2021

DOI: 10.1039/d1ta06006f

rsc.li/materials-a

1. Introduction

Reticular chemistry focuses on the development of framework materials prepared by linking molecular building units *via* coordination or covalent bonding.[1–3] Highly ordered crystalline metal–organic frameworks (MOFs)[1] and covalent–organic frameworks (COFs)[2] have attracted interest due to their structural features and advantageous properties, such as large specific surface area, programmable structures, tunable pore size, and readily available building blocks.[4] Their applications have been explored in various fields, including gas adsorption or separation, electrocatalysis, photocatalysis, energy storage, ion batteries, biosensors, and controlled delivery.[5–8] Further, MOFs/COFs have unique features of tunable pore size and periodic pores, which allow the incorporation of heteroatoms/metal coordinating moieties in a periodic way. However, some challenges still exist including their synthesis and functionalization, development of new nanostructures, and application in industry.[9] For example, the instability of MOFs cannot meet the industry requirement of long lifetime of commercial products. Also, their commercialization requires their large-scale production with uniform properties, and the development of simple and green synthetic methods is a current challenge to achieve their mass production at a lower cost. Alternatively, COFs are rapidly expanding porous crystalline polymers that are constructed from organic building blocks *via* reversible covalent bonds and have gained increasing attention from scientists.[10] Two-dimensional (2D) or 3D COFs consisting of accessible nanoscale channels or pores with uniform size and tunability have been widely prepared.[11] Their channel structures and pore walls provide a well-defined nanospace as reaction centers, thus leading to vast applications, such as in photocatalysis,[10,12] bioimaging and therapy,[13] electrochemical energy storage and conversion,[14] and electrocatalysis.[15]

However, although great efforts have been focused on the preparation, nanostructure formation, and wide applications of MOFs and COFs, individually they cannot meet the specific demand in various fields due to their intrinsic features. For example, pristine MOFs show intrinsic deficiencies such as unsatisfactory stability and limited electrical conductivity and functionality.[16] Moreover, although COFs show enhanced chemical stability, their specific surface areas and degree of crystallinity are poor.[10] Therefore, the hybridization of MOFs and COFs has been intensively studied to obtain superior performances (Fig. 1). For instance, the good photoconductivity and/or fast charge transfer features of COFs can remedy poor conductivity of MOFs or can promote the separation ability of photogenerated electrons and holes in MOF/COF-based hybrids. Consequently, the photoelectrochemical and electrochemical properties are improved, and thus MOF@COF hybrids

College of Material and Chemical Engineering, Zhengzhou University of Light Industry, Zhengzhou 450001, P. R. China. E-mail: 2006025@zzuli.edu.cn; dumiao@zzuli.edu.cn

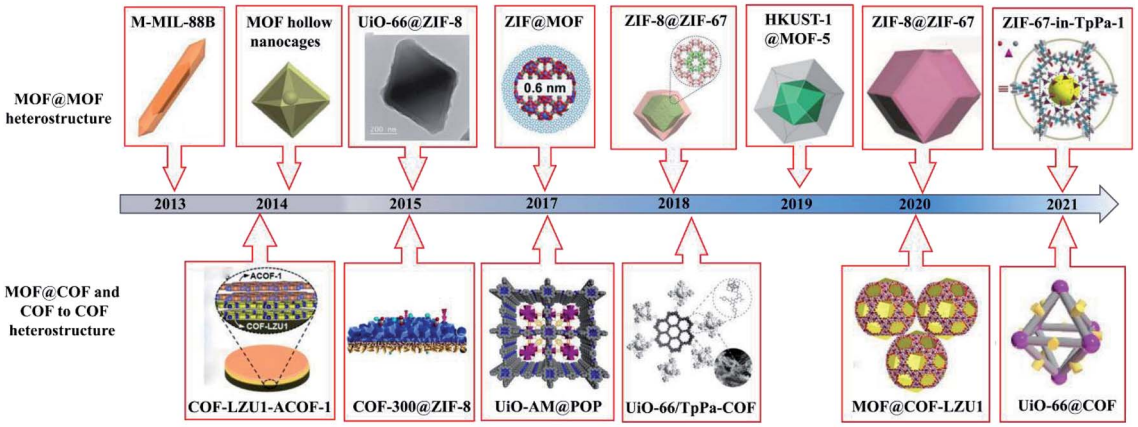

Fig. 1 Timeline of representative works reported on MOF/COF-based heterostructured hybrids.

can be employed for the construction of sensors to detect various targets. Moreover, the photocatalytic efficiency of MOF/COF-based hybrids also can be greatly enhanced, broadening their applications in the field of photocatalysis. Besides, MOF/COF hybrids possess an enhanced surface area and large pore volume due to the formation of quasi-micro-scaled pores at the interface between MOFs and COFs,[17,18] thus manifesting enhanced hydrogen uptake capacity in the field of energy storage. By integrating different functionalized MOF and COFs, various fantastic properties are generated due to the synergistic effects of each component for extensive applications in diverse fields. For instance, MOFs with large specific surface areas can serve as carriers for loading drugs, photosensitizers, and near infrared dyes, while some COFs with strong photothermal conversion or efficient reactive oxygen species can be explored as photothermal therapy (PTT) and photodynamic therapy (PDT) agents. These hybrids possess the merits of each component, showing synergistic effects such as chemotherapy, PTT, PDT, and imaging ability. Thereby, different types of MOF- and COF-hybrids[19–23] have also been developed to further widen their potential applications in gas storage and separation, catalysis, batteries, and biomedicine and biosensing.

According to the nanostructures and components, diverse MOF/COF-based heterostructures have been manufactured, including MOF-on-MOF (core–shell or layered structure), MOF@COF, and COF-to-COF (or COF@COF). This review outlines the recent advances on MOF/COF-based hybrids, including the classification, design principles, synthetic approaches, and applications of different MOF/COF-based hybrids (Fig. 2). Although there are many reviews on the design principles and methods for the synthesis of MOFs and COFs, the heterostructures of MOFs/COFs have rarely been explored. Haldar *et al.*[24] reviewed the hierarchical assemblies of MOF-on-MOF heterostructures, in which the layer-by-layer (LBL) and liquid-phase epitaxy (LPE) approaches for the preparation of surface-anchored MOF thin films and one-pot synthesis methods for these hierarchically designed structures, as well as their applications were discussed. In addition, Liu's group discussed the current advancements on the combination of MOFs and COFs,[25] in which only MOF@COF composites, ranging from their synthesis to enhanced applications, were provided. Zhang *et al.* also reviewed crystalline porous materials for electrochemical energy storage application, which summarized several hybridization techniques according to the dimensionality of hybridization.[26] Recently, a similar review was reported by Chen *et al.*, which focused on the synthetic approaches for MOF/COF hybrids and their applications.[16] Herein, a comprehensive overview of the nanostructure formation, synthesis approaches, and diverse applications of these hybrids is provided with particular focus on the following aspects: (1) the classification of MOF- and COF-related hybrids with specific nanostructures (Section 2), (2) the design principles and approaches for the synthesis of MOF- and COF-related hybrids (Section 3), (3) the detailed applications and functions of MOF- and COF-based hybrids (Section 4), and (4) the present challenges and future prospects for these hybrids (Section 5). This work aims to review the development progress,

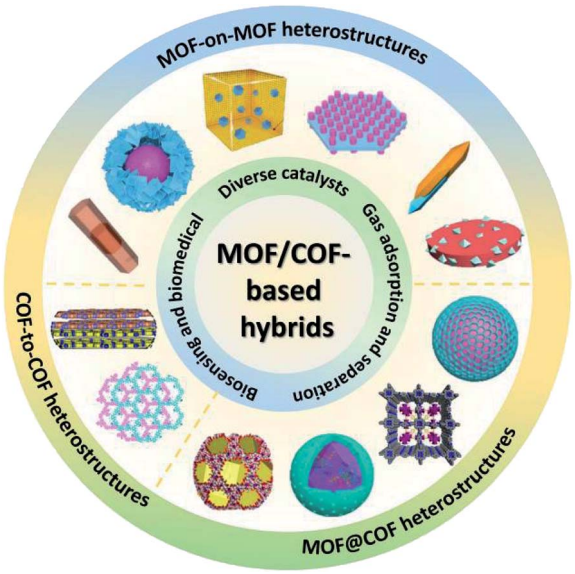

Fig. 2 Classifications and applications of MOF/COF-based hybrids.

state-of-the-art designs of hybrid nanostructures, synthetic strategies, and different applications of MOF- and COF-related hybrids to provide insights into the construction of MOF/COF hybrids and deep understanding in this field.

2. Heterostructures and hybrid types of MOFs/COFs

Hybridizing diverse types of MOFs/COFs is a promising strategy to manipulate their compositions and structures and precisely tune their basic properties (such as structural flexibility, ordered pores, high surface area, and chemical functionality). MOF/COF-based heterostructures and hybrids with precise heterostructures tend to efficiently provide vast possibilities to extend their applicability.[27,28] The following discussion focuses on the construction mechanism of different types of heterostructured MOF/COF-based hybrid materials.

2.1 MOF-on-MOF heterostructures

MOF-on-MOF hybrid materials are generated by introducing various organic ligands after crystal nucleation,[29] which can conjugate two or more different types of MOFs into one whole MOF-on-MOF hybrid material. Generally, these hybrids include two categories of architectures, namely one MOF fully enclosed by another MOF (called core–shell MOF@MOF) and one MOF grown on another MOF surface in an isotopic/anisotropic manner (called layered MOF-on-MOF). Usually, in the notation for MOF@MOF heterostructures, that on the left is the core MOF and that on the right is the grown MOF. The introduction of different MOF crystals has been extensively applied to form different types of core–shell MOF@COF heteroepitaxial crystals, while maintaining the intrinsic features of MOF crystals.[30] As early as 2009, Sakata and Kitagawa's group synthesized a core–shell MOF@MOF hybrid using the epitaxial growth approach.[31] In 2015, Yamauchi's group developed core–shell ZIF-8@ZIF-67 nanohybrids through a seed-mediated growth method.[32] Subsequently, great efforts have been devoted to developing diverse ZIF@ZIF heterostructures.[32–34] Coordinating the lattice of the second metal building unit with that of the first MOF core is essential in the construction of MOF@MOF hybrids.[35] For example, MIL (Materials of Institute Lavoisier) MOFs, ZIF (Zeolitic Imidazolate Framework), PBAs (Prussian blue analogs), and other types of nanoMOF nanostructures are usually used as the core and embedded within a second MOF layer.[36] Core–shell MOF-on-MOF heterostructures can combine the superior properties of their core and shell MOFs and substantially overcome the shortcomings of single MOFs.[37] Their enhanced synergistic selective performance can be designed through the lattice choice and synthetic route for application in catalysis, sorption or separation, and molecular recognition.[38] Therefore, these materials often exhibit specific features that differentiate them from individual MOFs.

Further, layered MOF-on-MOF structures are prepared using the initial MOF layer as a substrate, on which another MOF grows *in situ*. Heterostructured and layered MOF-on-MOF can be synthesized *via* the liquid phase epitaxial and vapor phase growth methods. In 2017, Eddaoudi's group reported a synthetic strategy to precisely control the epitaxial growth of an MOF-on-MOF film, *i.e.*, ordered hierarchical Cu-tbo-MOF-5 on HKUST-1 structure.[39] Takahashi's group presented a strategy for the macroscopic length scale precise alignment of multiple layers of MOF-on-MOF films, which were fabricated by epitaxially matching the interface. An oriented $Cu(OH)_2$ film acted as the substrate to form the first $Cu_2(BPDC)_2$ (BPDC = biphenyl-4,4′-dicarboxylate) MOF layer *via* a "one-pot" approach. Then, the second $Cu_2(BPYDC)_2$ (BPYDC = 2,2′-bipyridine-5,5′-dicarboxylate) MOF was deposited *via* liquid-phase epitaxy.[40] Simultaneously, the layered MOF-on-MOF thin film was achieved *via* van der Waals interactions, favoring the formation of highly oriented MOF-on-MOF thin films.[41] Hence, layered MOF-on-MOF heterostructures provide a good opportunity to construct MOF films with a controllable layer thickness, good orientation and crystallinity.

MOFs with similar lattices can easily form MOF@MOF hybrids. In 2012, Oh's group developed a series of MOF@MOF heterostructures, including MIL-68@MIL-68–Br, e-MIL-88B@Ga-MIL-88, MIL-68@MIL-68–X, MIL-88B@MIL-88A, In-MIL-68@MOF-NDC, MIL-68@MIL-68–Br, and MIL-68@MIL-68–X (X = NO_2 or NH_2).[42] With the development of synthetic approaches for MOF@MOF heterostructures, MOFs with diverse lattice crystals also can be conjugated to form hybrids such as MOF-801@Ni-MOF-74,[43] HKUST-1@MOF-5, UiO-67@HKUST-1, HKUST-1@IRMOF-18, UiO-66@MIL-88B(Fe), UiO-67@MIL-88C(Fe),[35] PCN-68@MOF-5, and UiO-66@ZIF-8,[44] and other types of Zn-MOF-on-Zr-MOF[45] and Fe-MOF-on-Tb-MOF[46] through the MOF-on-MOF strategy.

2.1.1 MIL-based MOF-on-MOF. A series of MOF-on-MOF heterostructures, including Fe–MIL-88B@Ga–MIL-88, MIL-68@MIL-68–X, MIL-68@MIL-68–Br, MIL-88B@MIL-88A, and In–MIL-68@MOF-NDC, has recently been designed and synthesized *via* the anisotropic growth method. In 2012, Oh's group prepared MOF-on-MOF heterostructures using Fe–MIL-88B, In–MIL-88B and Ga–MIL-88B. The 3D hexagonal Fe–MIL-88B nanorods were comprised of FeO_6 octahedral trimers, which were connected to the building block of BDC (BDC = 1,4-benzenedicarboxylate) (Fig. 3a). The resulting Fe–MIL-88B then served as a template for the preparation of the secondary MOF. Subsequently, the Fe–MIL-88B@M-MIL-88B heterostructure was prepared by consecutively growing secondary metal clusters (H_2BDC and $M(NO_3)_3$, $M = Ga^{3+}$ or In^{3+}) using the solvothermal method, resulting in multiple functional and modulated properties.[47] They also synthesized the core–shell MIL-68@MIL-68-Br, where the MIL-68 template was initially synthesized, followed by isotopically growing MIL-68–Br (Fig. 3b).[42] Owing to the similar nanostructures of the first MIL-68 and the MIL-68–Br layer, the core–shell MIL-68@MIL-68–Br hybrid was obtained. The detailed characterizations revealed that using the crystalline MIL-68 resulted in the formation of an MIL-68–X shell on the MIL-68 surface. However, the MIL-68–X structures showed poor crystallinity when the template was not used. By contrast, the enhanced crystallinity of MIL-68–X remarkably improved their porosities and surface areas. Especially, MIL-68–NH_2 with high crystallinity had a substantially larger surface

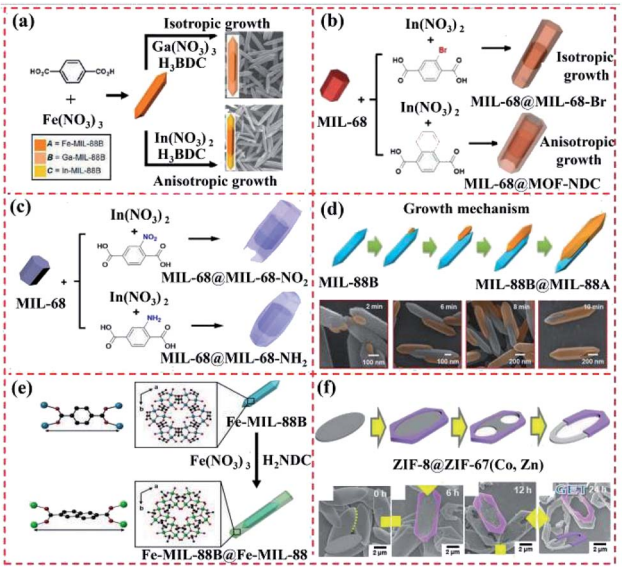

Fig. 3 Structure of MIL-MOF-based core–shell MOF-on-MOF or layered MOF-on-MOF heterostructure. (a) Heterometalation of Fe-MIL-88B@M-MIL-88B heterostructure (core–shell-type hybrid A@B and layer-type hybrid C/A/C) using Fe-MIL-88B nanorods as the seeds. Reproduced from ref. 47 with permission from the American Chemical Society, Copyright 2012. (b) MIL-68@MIL-68–Br and MIL-68@MOF-NDC obtained by isotropic and anisotropic growth with the 3D hexagonal-structured MIL-68 as the template. Reproduced from ref. 42, with permission from the American Chemical Society, Copyright 2016. (c) MIL-68@MIL-68-X (X = NO_2 or NH_2) hybrid-induced growth on 3D hexagonal-structured MIL-68. Reproduced from ref. 48 with permission from the American Chemical Society, Copyright 2018. (d) Mechanism for the unbalanced MOF-on-MOF growth of MIL-88A on the MIL-88B template for the production of the lopsided core–shell of MIL-88B@MIL-88A. Reproduced from ref. 49 with permission from The Royal Society of Chemistry, Copyright 2019. (e) Tip-to-middle MOF-on-MOF growth of the core–shell hybrids of single-shelled Fe-MIL-88B@Fe-MIL-88C and double-shelled Fe-MIL-88B@Ga-MIL-88B@Fe-MIL-88C. Reproduced from ref. 50 with permission from the American Chemical Society, Copyright 2020. (f) Formation of ZIF-8@ZIF-67(Co, Zn) rings using the MOF-on-MOF method *via* three preparation steps, including growth of 3D ZIF on a ZIF-L surface, partially etching the 2D ZIF-L template, and transforming the 2D ZIF-L into a 3D ZIF. Reproduced from ref. 51 with permission from Wiley, Copyright 2020.

area than that with low crystallinity. A similar result was obtained for MIL-68@MIL-68–X (X = NO_2 or NH_2), which was prepared (Fig. 3c) by reacting H_2BDC–NO_2 with $In(NO_3)_3$ with the help of the crystalline MIL-68, resulting in the oriented growth of MIL-68–NO_2 on the surface of MIL-68.[48]

Moreover, Oh's group developed the MIL-88B@MIL-88A heterostructure through the unbalanced MOF-on-MOF growth method (Fig. 3d). Given their similar 3D hexagonal structure but mismatched cell parameters, the preparation of MIL-88A on MIL-88B gave rise to an atypical MIL-88B@MIL-88A with an off-centered core. Nano-sized hexagonal MIL-88B rods with a 3D hexagonal structure were synthesized, and then used as a template to grow MIL-88A and form the core–shell MIL-88B@MIL-88A hybrid.[49]

Based on previous work, Oh's group constructed a core–shell MOF hybrid using the isotropic or anisotropic growth approach (Fig. 3e). The MIL-88B and MIL-88C nanostructures exhibited different chemical structures and/or cell lattices on the MIL-88B surface. Ga–MIL-88B was isotopically prepared on the Fe–MIL-88B template surface and also formed a core–shell MOF hybrid. Moreover, the core–shell hybrids of single-shelled Fe–MIL-88B@Fe–MIL-88C and double-shelled Fe–MIL-88B@Ga–MIL-88B@Fe–MIL-88C were prepared *via* the growth of Fe–MIL-88C on the MIL-88B core. The basic characterization revealed the change in the chemical structures and component during the growth of the MOF-on-MOF hybrids, thus showing the applicability of the unique tip-to-middle anisotropic growth approach and the unprecedented self-adjustment and self-reversion of the MOF cell lattices. All these effects finally led to the formation of the core–shell MOF@MOF hybrid *via* anisotropic growth.[50] Besides these MOF-on-MOF heterostructures, Oh's group developed novel ZIF-8@ZIF-67(Co, Zn) rings using the MOF-on-MOF method *via* three preparation steps, including the growth of 3D ZIF on a ZIF-L surface, partially etching the 2D ZIF-L template, and transforming the 2D ZIF-L into a 3D ZIF (Fig. 3f). The core–shell MOF@MOF rings and plates were modulated by changing the three steps.[51] In 2020, an MIL-88B-on-UiO-66 hybrid phase was prepared.[52] The atypical-shaped NPs were composed of eight precisely aligned 3D hexagonal rods grown on the eight faces of one octahedron. Apparently, these core–shell MIL-MOF@MIL-MOF heterostructures were prepared using two MOFs with the same lattice crystals. Thus, the exploration of the potential applications of these well-designed MOF-on-MOF hybrid materials will be promising in the near future.

2.1.2 ZIF-based MOF-on-MOF. The isomorphism of some ZIFs can boost heterogeneous nucleation, whereas the fast addition of precursors is unfavorable for the heterogeneous nucleation induced by seeds. A series of ZIF@ZIF heterostructures have been prepared using the MOF-on-MOF strategy, showing great potential and wide applications in diverse fields. In 2015, Kang *et al.* provided an engineering strategy to obtain core–shell ZIF-L@ZIF-8 nanocomposites *via* the preparation of ZIF-8 crystals on ZIF-L nanosheets (Fig. 4a). The functionality of ZIF-8 was introduced into the ZIF-L@ZIF-8 hybrids.[53] Zhang *et al.* developed uniform double-layered core–shell ZIF-67@ZIF-8 and ZIF-8@ZIF-67 crystals, as well as three-layered core–shell ZIF-67@ZIF-8@ZIF-67 and ZIF-8@ZIF-67@ZIF-8 crystals. In this case, the core diameter and shell thickness were strictly modulated using different seed sizes and molar feeding ratios of Zn^{2+}/Co^{2+}, respectively (Fig. 4b).[54] Guo *et al.* investigated different core–shell ZIF-67@ZIF-8/67 nanocrystals, which were also obtained by modulating the core/shell thickness ratio, depending on the intervals after the initial addition of Co^{2+} (Fig. 4c). Only nanostructured hybrids of ZIF-67 and ZIF-8 were obtained, and it was found that agglomerates with an irregular shape were formed when Zn^{2+} ions were added first due to their inferior nucleation activity. When Co and Zn ions were introduced in the solution initially, a homogeneous distribution of these two metals was obtained at a high Co/Zn ratio, while a gradient from Co-rich cores to Zn-rich shells was formed at a low Co/Zn ratio.[55] Ghalei's group prepared nano-sized core–shell ZIF-67@ZIF-8 crystals using ZIF-67 as the core and ZIF-8 as

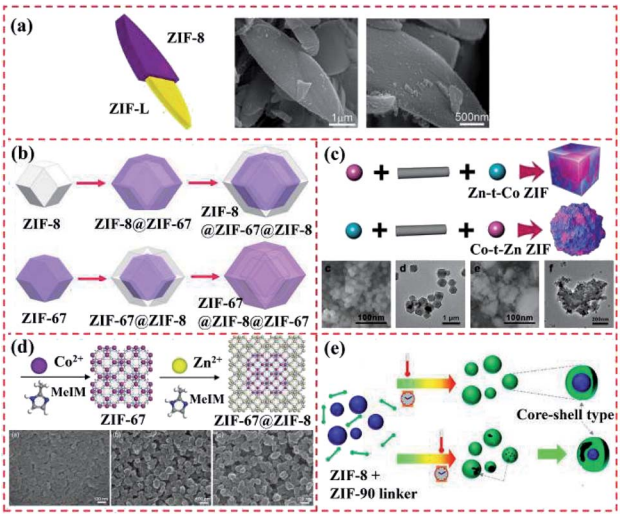

Fig. 4 Structure of ZIF-based core–shell MOF-on-MOF hybrid. (a) Illustration and SEM images of ZIF-L@ZIF-8 core–shell nanocomposite. Reproduced from ref. 53 with permission from the American Chemical Society, Copyright 2015. (b) Synthetic scheme for the preparation of core–shell ZIF-8@ZIF-67 crystals, core–shell ZIF-8@ZIF-67@ZIF-8 crystals, core–shell ZIF-67@ZIF-8 crystals, and core–shell ZIF-67@ZIF-8@ZIF-67 crystals. Reproduced from ref. 54 with permission from the American Chemical Society, Copyright 2016. (c) Core–shell ZIF-67@ZIF-8/67 with tunable core/shell thickness. Reproduced from ref. 55 with permission from Wiley, Copyright 2017. (d) Synthesis of nanosized core–shell ZIF-67@ZIF-8 crystals *via* seed-mediated growth and their loading in polyimide and Pebax 1657 for gas separation. Reproduced from ref. 56 with permission from Wiley, Copyright 2020. (e) Schematic mechanism for the synthesis of ZIF-8@ZIF-90 *via* solvent-assisted linker exchange. Reproduced from ref. 57 with permission from the American Chemical Society, Copyright 2017.

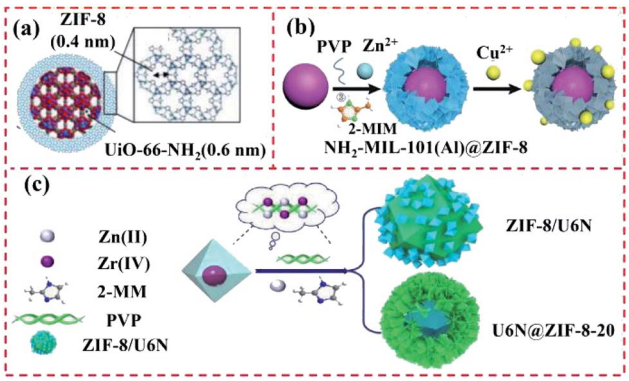

Fig. 5 Structure of the heterostructures of hybrids of ZIFs with other types of MOFs. (a) ZIF-8@UiO-66–NH_2 hybrid using UiO-66–NH_2 and ZIF-8 as the core and shell. Reproduced from ref. 58, with permission from the American Chemical Society, Copyright 2017. (b) Schematic illustration of the fabrication of core–shell NH_2–MIL-101(Al)@ZIF-8 nanoflower for the simultaneous detection and removal of Cu(II). Reproduced from ref. 59 with permission from The Royal Society of Chemistry, Copyright 2018. (c) Illustration of the preparation of U6N@ZIF-8 and ZIF-8/U6N. Reproduced from ref. 36 with permission from Elsevier, Copyright 2020.

the shell (Fig. 4d), which were embedded in polyimide and Pebax 1657 substrates.[56] Krishna *et al.* studied the differences in the structures and mechanisms for the synthesis of the mixed-linker ZIF by manufacturing a series of ZIF-8-90 hybrids (Fig. 4e).[57] The results revealed the feasibility of integrating diverse ZIFs with a similar linker for the construction of MOF@MOF and MOF-on-MOF hybrids.

It is difficult to precisely control the synthesis of MOFs with different ligands and morphological structures are owing to their high surface energy. These types of MOF@MOF heterostructures are usually synthesized *via* surfactant-mediated overgrowth to reduce their surface energy. Zhuang *et al.* synthesized uniform and solid UiO-66@ZIF-8 particles with diverse crystalline structures and chemical components with the aid of a surfactant called cetyltrimethylammonium bromide (CTAB). A similar Pd–UiO–NH_2@ZIF-8 hybrid was also synthesized and used as a catalyst, where UiO-66–NH_2 NPs were applied as the core MOF to load Pd NPs and ZIF-8. Consequently, the Pd–UiO–NH_2@ZIF-8 hybrid demonstrated remarkable molecular sieving behaviour.[44] Song *et al.* developed the ZIF-8@UiO-66–NH_2 hybrid using UiO-66–NH_2 and ZIF-8 as the core and shell, respectively, for boosting transport pathways and molecular sieving properties. The ZIF-8 layer was synthesized over the external UiO-66–NH_2 surface *via* the LBL solution deposition method and the UiO-66–NH_2 core was sequentially added to the preparation system of ZIF-8 (Fig. 5a). During LBL processing, the amino group of UiO-66–NH_2 enabled it to be covalently bonded with other MOF and ZIF precursors.[58] Furthermore, Zhang *et al.* reported the preparation of a core–shell NH_2–MIL-101(Al)@ZIF-8 nanoflower *via* the internally extended growth method in the presence of polyvinyl pyrrolidone (PVP) (Fig. 5b). NH_2–MIL-101(Al) nanospheres were used as the core, while ZIF-8 was utilized as the shell.[59] According to the above-mentioned examples, PVP with a long-chain can endow different MOFs with the ability of uniform growth by reducing their surface energy.[60] For instance, Xiong *et al.* prepared two types of UiO-66–NH_2@ZIF-8-20 and ZIF-8/UiO-66–NH_2 heterostructures by using PVP as a regulator, where ZIF-8 changed from a dodecahedron to a lamellar direction growth (Fig. 5c).[36]

2.1.3 PBA-based MOF-on-MOF. Different types of Prussian blue (PB) and PBAs have been employed in different fields, such as clean energy, catalysis, biomedicine, and biosensing,[61] owing to their nano-scaled size, good compatibility with other layers, and multifarious functionality. PB or PBA NPs have been conjugated with diverse nanomaterials and MOFs. Wang *et al.* developed core–shell PB@ZIF-8 NPs as an excellent drug delivery system for loading doxorubicin (DOX) for cancer treatment. An electronegative surface was first formed by modifying PB with poly(sodium-4-styrenesulfonate), which was then attracted to the positively charged Zn^{2+} ions of ZIF-8, thus forming the ZIF-8 shell. The formation of isolated and coated ZIF-8 NPs was mainly due to homogeneous and heterogeneous nucleation, respectively. When the precursor concentration was low, NP-induced heterogeneous nucleation occurred easier than homogeneous nucleation because the synthetic system only

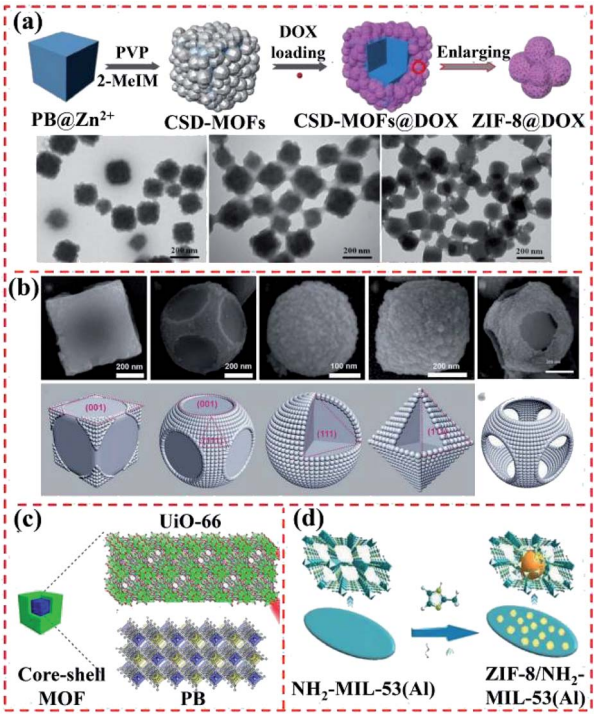

Fig. 6 Structure of PBA-based MOF@MOF heterostructures. (a) Schematic illustration of procedure for the synthesis of PB@ZIF-8. Reproduced from ref. 62 with permission from Ivyspring International Publisher, Copyright 2017. (b) Fe^{3+}-modulated shape control of PBA@PBA. Reproduced from ref. 63 with permission from The Royal Society of Chemistry, Copyright 2018. (c) PB as the core for the growth of a porphyrin-doped UiO-66 MOF. Reproduced from ref. 64 with permission from the American Chemical Society, Copyright 2020. (d) ZIF-8/NH_2–MIL-53(Al) obtained by anchoring ZIF-8 on 2D NH_2–MIL-53(Al) nanoplates. Reproduced from ref. 65 with permission from Elsevier, Copyright 2019.

needed to overcome a low energy barrier. Hence, small ZIF-8 crystal nuclei were obtained on the PB nanocube surface, thereby forming uniform ZIF-8 shells. When the precursor concentration was high, homogeneous and heterogeneous nucleation simultaneously and competitively occurred, resulting in the coexistence of isolated and coated ZIF-8 NPs. Small ZIF-8 NPs with an irregular shape were prepared *via* homogeneous nucleation at a high precursor concentration (Fig. 6a).[62] Yu *et al.* proposed a one-pot method for the synthesis of core–shell PBA@PBA nanostructures using an ion-modulation strategy (Fig. 6b), where Fe^{3+} was used as the indicator. A certain amount of Fe^{3+} ions underwent a partial phase transition to form new PBA NPs, which were epitaxially grown onto the original PBA core. The charge transfer band between ligand-to-metal was excited, resulting in charge transfer from CN^- to Fe^{3+}, thus causing a phase change occur. Subsequently, charges were provided from Mn^{II} to CN^-. Afterward, the phase transition between the cubic-phase PBA and tetragonal-phase PBA resulted in the conversion of the nanostructure and morphology from a cube to octahedron. Although the lattice was distorted, similar crystallographic parameters were observed in the Mn^{II}-NC-Fe^{III} and Mn^{III}-NC-Fe^{II} phases. Thus, this led to the growth of the shell MOF on the core MOF through the epitaxial growth method.[63] Moreover, a PB MOF and a porphyrin-doped UiO-66–TCPP MOF (TCPP = 5,10,15,20-tetrakis(4-carboxyphenyl)porphyrin) were used as the core and shell, respectively, to develop a novel core–shell MOF hybrid. Due to the defects present in the UiO-66 network, porphyrin ligands were introduced into the UiO-66 crystal. The outer surface of the PB MOF was modified with PVP, in which the oxygen in the carbonyl group of PVP bound with the Zr ions of UiO-66. The formed Zr–O bonds remarkably enhanced the further growth of the MOF over the PB surface. Consequently, the core–shell PB@MOF hybrid was prepared by using PB modified with PVP as a crystal nucleus (Fig. 6c).[64] Also, using PVP as an activator, the ZIF-8/NH_2–MIL-53(Al) hybrid was

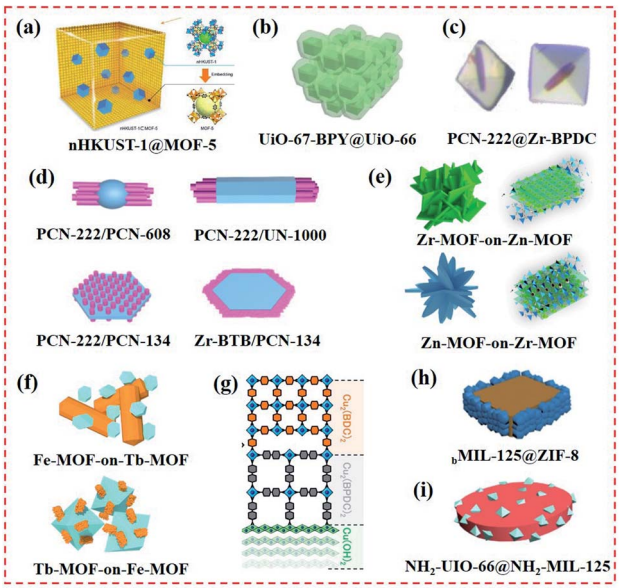

Fig. 7 Structure of MOF-on-MOF heterostructures. (a) nHKUST-1 ⊂ MOF-5 structure formed by embedding nanocrystalline HKUST-1 (nHKUST-1) in MOF-5 crystals. Reproduced from ref. 66 with permission from the American Chemical Society, Copyright 2015. (b) Core–shell UiO-67–BPY@UiO-66. Reproduced from ref. 67 with permission from Elsevier, Copyright 2019. (c) Core–shell MOFs (PCN-222@Zr-BPDC) with mismatching lattices by epitaxial growth. Reproduced from ref. 30 with permission from the American Chemical Society, Copyright 2018. (d) Selective epitaxial growth of PCN-222 nanorods on 0D PCN-608 nanoparticle, 1D UN-1000 nanorod, and 2D PCN-134 nanoplate. Reproduced from ref. 68 with permission from the American Chemical Society, Copyright 2020. (e) Two MOF-on-MOF of Zn-MOF-on-Zr-MOF and Zr-MOF-on-Zn-MOF hybrids. Reproduced from ref. 45 with permission from Elsevier, Copyright 2018. (f) Bimetallic core–shell Tb-MOF-on-Fe-MOF and Fe-MOF-on-Tb-MOF nanostructures formed by Tb-MOF nanorod and hexagon-structured Fe-MOF. Reproduced from ref. 46 with permission from Elsevier, Copyright 2019. (g) Multiple layered MOF-on-MOF films using liquid-phase epitaxy. Reproduced from ref. 40 with permission from Wiley, Copyright 2019. (h) Selective growth of ZIF-8 on the side {110} facets of $_b$MIL-125. Reproduced from ref. 69 with permission from The Royal Society of Chemistry, Copyright 2020. (i) NH_2–UiO-66(Zr) @NH_2–MIL-125(Ti) nanohybrid. Reproduced from ref. 70 with permission from Wiley, Copyright 2017.

obtained because of the pre-concentration effect of ZIF-8 adsorbing the 2D NH_2–MIL-53(Al) surface (Fig. 6d).[65]

2.1.4 Other types of MOF-on-MOF. Various core–shell MOF@MOF hybrids are often prepared through a stepwise approach, where the MOF core is firstly generated and further explored as a template for growing the shell.[36] Aiming at the full combination of the shell and core components, lattice matching is necessary. However, this increases the difficulty in the development of synthetic methods to meet the requirement of lattice-matching for core–shell MOF@MOF nanohybrids. In addition to ZIFs and PBs, other types of MOFs have been utilized for the synthesis of MOF-on-MOF. Kang's group synthesized a core–shell "nHKUST-1(nHKUST-1) ⊂ MOF-5" structure by introducing MOF-5 into HKUST-1 hybrids (Fig. 7a). This specific nanostructure resulted in new interfaces between the MOF core and MOF shell, producing different properties from their MOF parents. Specifically, MOF-5 [$Zn_4O(BDC)_3$] was embedded in the nanocrystalline HKUST-1 to construct the "nHKUST-1 ⊂ MOF-5" heterostructure, which encapsulated guest molecules.[66] Similarly, Kwon *et al.* combined the metal clusters of one MOF with organic linkers of a second MOF to form a series of single crystalline MOF@MOF hybrids.[35] Gong *et al.* presented a core–shell UiO-67–BPY@UiO-66 nanostructure by combining UiO-66 and UiO-67–BPY (Fig. 7b).[67] Moreover, Zhou's group prepared a core–shell PCN-222@Zr-BPDC structure *via* a one-pot synthetic method (Fig. 7c). PCN-222 and Zr–BPDC both exhibited mismatched lattices. TCPP on PCN-222 bound strongly with Zr^{4+}, thus affording fast and homogeneous crystal nucleation. However, a longer time was needed for crystal formation with BPDC (BPDC = biphenyl-4,4′-dicarboxylate) than TCPP under similar experimental conditions. When the seed crystal was used as the core for preparing the second MOF, heterogeneous nucleation occurred faster than its homogenous counterpart. Accordingly, the core–shell PCN-222@Zr-BPDC hybrid was synthesized by binding Zr^{4+} ions with H_4TCPP and H_2BPDC.[30] Apparently, these hierarchical MOF heterostructures can only be formed using MOF seeds prepared with diverse building blocks and morphologies for matching the secondary MOF lattice and allowing them to be grown epitaxially on the MOF seed surface with low lattice mismatch. This technique was verified by Zhang's group. Different types of MOF nanostructures such as 0D PCN-608 NPs, 1D NU-1000 nanorods, and 2D PCN-134 nanoplates were used as diverse seeds for the epitaxial growth of PCN-222 nanorods (Fig. 7d).[68]

In addition to the development of core–shell MOF@MOF heterostructures, other types of MOF-on-MOF nanohybrids have been developed using various methods. In our previous work, two types of ZnZr-based MOFs, namely, Zn-MOF-on-Zr-MOF and Zr-MOF-on-Zn-MOF heterostructures, were developed *via* the MOF-on-MOF method by varying the addition sequence of the precursors and organic ligands (Fig. 7e). The obtained Zn-MOF-on-Zr-MOF hybrid exhibited a hierarchical decussated foliate, while the Zr-MOF-on-Zn-MOF hybrid showed a multilayered structure.[45] Two core–shell Tb-MOF-on-Fe-MOF and Fe-MOF-on-Tb-MOF nanostructures were also synthesized, displaying different nanostructures from their parent MOFs (Fig. 7f).[46] KenIkigaki *et al.* provided an oriented MOF film using a one-pot method, followed by combining two different MOF layers with epitaxial-matched lattices using the LBL approach (Fig. 7g). Precisely oriented $Cu_2(BPYDC)_2$ films were prepared as the upper MOF layer. The incorporated bipyridine linker in the oriented MOF lattice produced metal salts and ions.[40] Xu's group developed a TCPP-on-Cu–HHTP (HHTP = 2,3,6,7,10,11-hexahydrotriphenylene) thin film *via* van der Waal forces.[41] Liu *et al.* designed and developed MOF-on-MOF heterostructures using a site-specific epitaxial-growth strategy. For this system, two tetragonal MIL-125(Ti)-based MOF nanostructures with cake- and box-like morphologies (named $_c$MIL-125 and $_b$MIL-125, respectively) were used as the templates, and ZIF-8 was explored as the guest (Fig. 7h).[69] Gu *et al.* systematically developed a novel NH_2–UiO-66(Zr)@NH_2–MIL-125(Ti) nanohybrid, which overcame the restriction of matching lattices for the two MOFs (Fig. 7i). With the help of PVP, NH_2–MIL-125(Ti) and NH_2–UiO-66(Zr) were integrated into an MOF-on-MOF nanohybrid and showed distinct morphologies and crystal structures.[70]

2.2 MOF@COF heterostructures

Although many individual MOFs and COFs have been synthesized and applied in diverse fields, their exploration and applications are less than satisfactory due to the limited types and monotonous structures. The MOF/COF-based hybrids obtained by combining different types of MOFs and COFs can produce multifunctional porous MOF@COF heterostructures.[71] To date, the growth of MOF@COF nanohybrids mainly depends on the formation of an imine bond (–C═N–) between the reserved –NH_2 groups of MOFs and aldehydes present on COFs *via* a condensation reaction.[72] In particular, UiO-MOFs and MIL-MOFs are often employed for the fabrication of MOF@COF heterostructures because of their good chemical stability, flexible synthetic strategies, multifunctional properties, and good crystallization.[73] Moreover, COF nanospheres can also serve as the core, and MOF layers synthesized around them *via* covalent bonds to obtain core–shell MOF@COF heterostructures.[74] In this part, the current MOF@COF nanohybrids are summarized according to their MOF type.

2.2.1 UiO-based MOF@COF. Diverse UiO-66 and UiO-like MOFs can be combined with nanomaterials to enhance their potential applications in various fields.[75] A series of UiO-66-based MOF@COF heterostructures was synthesized *via* the covalent binding of the functional groups on MOFs or COFs.[76] Zheng *et al.* synthesized a nanoscale UiO-AM@COF composite using UiO-type NMOFs as self-templates (Fig. 8a). An amine-based porphyrin molecule, tetrakis(4-aminophenyl)$_{21}H,_{23}H$-porphine (H_2P), and various functional-substituted terephthalaldehydes have been employed as linking ligands to obtain diverse MOF/COF bearing imine groups and regular 2D networks. The size distribution and surface morphology of UiO-AM@COF were feasibly modulated by changing amine positions on the exterior of the UiO-AM seed and the used ratios of H_2P and terephthalaldehyde. Consequently, after chemical modification with MOF/COF, the obtained NPs exhibited high

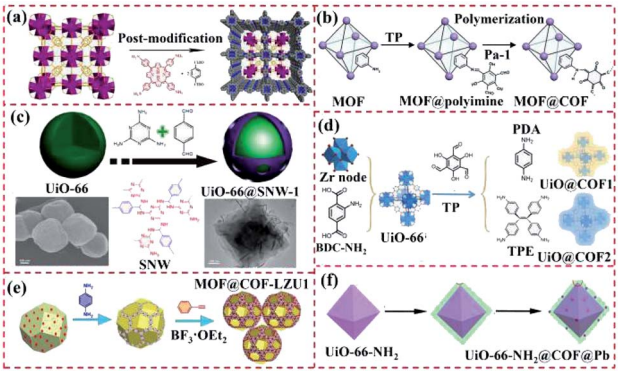

Fig. 8 Structure of UiO-based MOF@COF heterostructures. (a) Reproduced from ref. 77 with permission from the American Chemical Society, Copyright 2017. (b) Reproduced from ref. 78 with permission from Elsevier, Copyright 2018. (c) Reproduced from ref. 79 with permission from the American Chemical Society, Copyright 2018. (d) Reproduced from ref. 80 with permission from the American Chemical Society, Copyright 2020. (e) Reproduced from ref. 72 with permission from Wiley, Copyright 2020. (f) Reproduced from ref. 84 with permission from the American Chemical Society, Copyright 2020.

crystallization, well-dispersed size distribution, and integrated pore, similar to that of UiO-AM.[77] In 2018, Zhan *et al.* and Cheng *et al.* prepared NH_2–UiO-66/TpPa-1-COF composites by covalently linking NH_2–UiO-66 on the surface of the TpPa-1 COF. TpPa-1-COF was synthesized by reacting *p*-phenylenediamine (PDA) and 1,3,5-triformylphloroglucinol (Tp) (Fig. 8b). The results revealed that NH_2–UiO-66 particles were uniformly distributed on the surface of TpPa-1-COF.[78] Qi *et al.* reported a new MOF@POP composite (UiO-66@SNW-1) comprised of Lewis acid sites (Zr clusters in UiO-66) and Brønsted base sites (amino groups in SNW-1) (Fig. 8c). Thereby, these functional groups served as a superior bifunctional catalyst. The results revealed that the UiO-66 crystals were embedded in the SNW-1 layer, leading to the formation of a rough UiO-66 surface.[79] Yao and co-workers developed a UiO-66@COF-2 hybrid material for eliminating aggregation-caused quenching and enhancing the emission of COFs (Fig. 8d). UiO-66–NH_2 crystals were selected as the MOF core, while the –NH_2 group on UiO-66–NH_2 could be tightly bonded for the synthesis of a COF-2 layer with 2,4,6-benzenetricarbaldehyde and tetra-amino-tetraphenylethylene *via* a Schiff base reaction. Consequently, the UiO-66 core could improve the fluorescence of the bulky COFs, and also boost the sensing selectivity for adenosine triphosphate (ATP) owing to the high affinity of Zr^{4+} toward the phosphate group.[80] Chen *et al.* provided a novel core–shell NH_2–UiO-66@TFPT–DETH heterostructure photocatalyst (DETH, hydrazine monomer and TFPT, aldehyde monomer). Herein, the TFPT–DETH COF was explored as the outer layer because of its good stability. For the preparation of the heterostructure, the TFPT monomer was anchored on the surface of NH_2–UiO-66, thus forming NH_2–UiO-66@TFPT *via* the Schiff-base reaction between the aldehyde group and amino group on NH_2–UiO-66. After the pre-coated TFPT molecules were added, DETH and TFPT were exclusively *in situ* polymerized on the NH_2–UiO-66 surface to form the core–shell NH_2–UiO-66@TFPT–DETH heterostructure.[81] Peng *et al.* prepared an aza-MOF@COF hybrid material, where the dispersion of the UiO-66–NH_2 crystals was improved by adding PVP to easily coat the imine-linked COF. The porous aza-MOF@COF hybrid was synthesized using the following three steps: the surface modification of UiO-66–NH_2 with 1,3,5-benzenetricarboxaldehyde (BTCA), producing UiO-66–CHO, the *in situ* growth of the COF layer on UiO-66 through condensation between the aldehydes on UiO-66–CHO and PDA, and the modification of MOF@COF-LZU1 *via* the aza-Diels–Alder reaction (Fig. 8e).[72] Similar to UiO-66, Hf-MOF can be prepared through the coordination of $Hf_6O_4(OH)_4$ clusters with organic ligands. Zheng *et al.* synthesized an Hf-UiO-AM@POP-PEG nanocomposite (POP: porous-organic polymer) *via* the growth of tetrakis(4-aminophenyl)-21*H*,23*H*-chlorin (TAPC), terephthalaldehyde and PEG5k-NH_2 on the outer surface of NH_2–Hf-UiO-66 (Hf-UiO-AM).[82]

For MOF@COF hybrids, their MOF component can efficiently modulate their quality, surface morphology, optical performance, and catalytic properties. The N heteroatoms in COFs endow them high ability for binding Pd or Pt species.[83] Zhu *et al.* provided a new UiO-66–NH_2@COF@Pd hybrid using UiO-66–NH_2 as the core and the covalently linked COF as the shell. Here, Pd nanoclusters (~0.8 nm) were successfully confined in UiO-66–NH_2@COF. The obtained UiO-66–NH_2@-COF@Pd had high porosity, good stability and large specific surface area (Fig. 8f). The prepared UiO-66–NH_2@COF@Pd hybrid had a hierarchical porous structure and was loaded with abundant Pd nanoclusters. The strong synergism of each component of the hybrid led to excellent catalytic performances.[84]

2.2.2 MIL-based MOF@COF. MOF crystals often bear a functional amino group (such as NH_2–MIL-68, NH_2–MIL125(Ti) MOF, and NH_2–MIL-101(Fe)), which can covalently link with the carboxyl or aldehyde groups in the building blocks of COFs, thus leading to the tight binding of MOFs and COFs (Fig. 9a).[85] Hence, developing the series of NH_2–MIL-MOF@COF hybrids can remarkably extend their potential applications. Zhang's group prepared NH_2–MIL-68@TPA-COF and explored it as an effective photodegradation catalyst (Fig. 9b). After NH_2–MIL-68 was modified with tris(4-formylphenyl) amine (TFPA), TPA-COF was synthesized around the NH_2–MIL-68(CHO) surface by linking TFPA and tris(4-aminophenyl)amine (TAPA) *via* a feasible condensation synthesis method to produce the NH_2–MIL-68@TPA-COF hybrid material. Given the rod-like morphology of NH_2–MIL-68, the obtained NH_2–MIL-68(CHO) exhibited a similar surface morphology.[74] In addition, Ti-based MOFs exhibit superior photocatalytic ability because of their high chemical stability, redox ability, and photocatalytic performances.[86,87] In this regard, NH_2–MIL-125(Ti)-based MOF@COF hybrids show promising applications. Sun *et al.* developed a Pd-doped core–shell MOF@COF hybrid using TiATA and the 2D imine-based COF-LZU1 as the core and shell, respectively, (Pd/TiATA@LZU1). NH_2–MIL-125(Ti) allowed the direct growth of the COF shell without a modification step, followed by the doping of Pd NPs. The MOF@COF hybrid had an octahedral shape similar to TiATA, where the TiATA surface in the MOF@COF hybrid was coated by COF nanosheets.[88] He

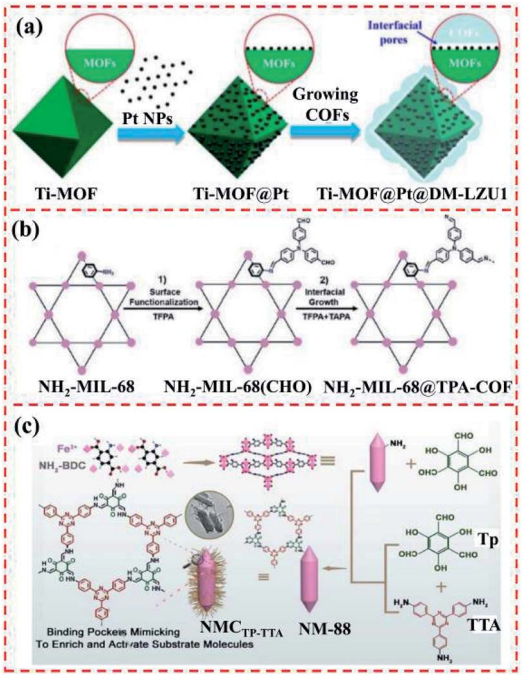

Fig. 9 Structure of MIL-MOF-based MOF@COF heterostructures. (a) Reproduced from ref. 85 with permission from the American Chemical Society, Copyright 2020. (b) Reproduced from ref. 74 with permission from Wiley, Copyright 2017. (c) Reproduced from ref. 91 with permission from Wiley, Copyright 2020.

et al. also prepared a variety of MOF/COF hybrids by separately integrating NH_2–MIL-53(Al), NH_2–UiO-66(Zr), and NH_2–MIL-125(Ti) with TTB–TTA (a COF synthesized from 4,4′,4″-(1,3,5-triazine2,4,6-triyl) tribenzaldehyde (TTB) and 4,4′,4″-(1,3,5-triazine-2,4,6-triyl) trianiline (TTA)) layer. The obtained MOF@COF inherited the merits of both MOFs and COFs.[89] Cai *et al.* developed stable core–shell NH_2–MIL-101(Fe)@NTU-COF composites, where NH_2–MIL-101(Fe) was employed as the core owing to its large surface area, good stability, and feasible modification. The growth of NTU-COF was controlled around NH_2–MIL-101(Fe) by forming an imine group and boroxine ring between 4-formylphenylboronic acid (FPBA) and 1,3,5-tris(4-aminophenyl)-benzene (TAPB). Consequently, condensation occurred between 2-aminoterephthalic acid and FPBA, leading to the covalent linking of FPBA to the NH_2–MIL-101(Fe) surface. The residual $-B(OH)_2$ groups in FPBA were then applied as active sites for the synthesis of NTU-COF. Subsequently, this reaction resulted in strong binding between NH_2–MIL-101(Fe) and NTU-COF.[90] Actually, a nature-inspired MOF@COF nanozyme was constructed (denoted as $NMC_{TP\text{-}TTA}$) using NH_2–MIL-88B (Fe) as a model nanozyme, while $COF_{TP\text{-}TTA}$ was grown around NH_2–MIL-88B (Fe) (Fig. 9c).[91] Lv *et al.* synthesized a ternary MIL-88B@COF-200@10%PANI (polyaniline) composite with a double p–n heterojunction *via* a self-assembly strategy. The spherical COF-TPA/TPB was fabricated by compositing with SiO_2. Subsequently, it was added during the procedure for the synthesis of MIL-88B, thus gaining MIL-88B@COF hybrids. Furthermore, these hybrids were introduced into a certain amount of PANI solution, assembling MIL-88B@COF@PANI composites with significant photocatalytic activity.[92]

2.2.3 Other types of MOF@COF. Besides covalent binding at the interface between amino-functionalized MOFs and COFs bearing aldehyde groups for the development of core–shell nanostructured MOF@COF hybrids, other types of MOF@COF composites have been prepared *via* hydrogen bonds and π–π stacking. Fu *et al.* developed a ZIF-8@COF-300 composite membrane, where COF-800 was synthesized using terephthalaldehyde and tetra-(4-anilyl)methane as monomers *via* a condensation reaction (Fig. 10a). The polyaniline layer was first coated on an SiO_2 disk, followed by the surface modification of polyaniline with terephthalaldehyde. Free C=O groups then reacted with tetra-(4-anilyl)-methane to produce a uniform COF-300 layer. Subsequently, hydrogen bonds were formed between terephthalic acid and the amine groups on COF-300, thus boosting the integration of the ZIF-8 top layer.[93]

In addition to hydrogen bonds, the coordination binding between the zinc cation and amine group can enhance the binding of the COF and MOF components. In our previous work, a Co-MOF was synthesized over a terephthalonitrile-derived nitrogen-rich network surface, thus leading to the formation of the Co-MOF@TPN-COF hybrid. $Co(NO_3)_2 \cdot 6H_2O$ and 2-methylimidazole were used to prepare Co-MOF, and terephthalonitrile was polymerized over the Co-MOF surface (Fig. 10b). The proposed Co-MOF@TPN-COF displayed the advantages of MOFs and COFs, such as abundant nitrogen-related groups and excellent conductivity.[94] Gao and co-workers constructed core–shell PCN-222-Co@TpPa-1 hybrid materials *via* strong π–π stacking to overcome their disadvantages and produce a synergistic effect, which afforded multifunctional properties (Fig. 10c). The obtained core–shell PCN-222-Co@TpPa-1 exhibited good stability and superior catalytic activity.[71] Moreover, the Ce-MOF@MCA nanohybrid was

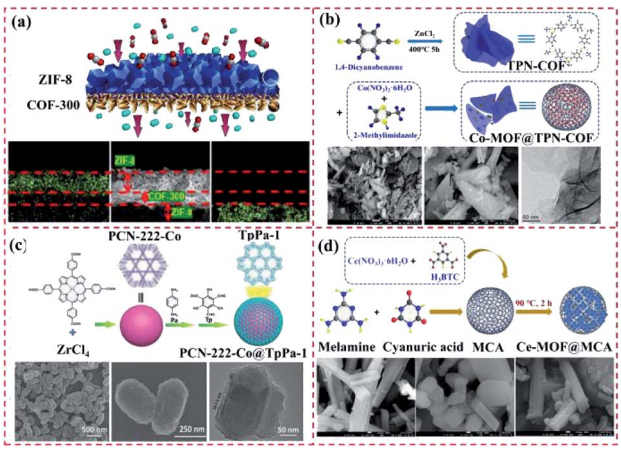

Fig. 10 Structure of other types of MOF@COF. (a) Reproduced from ref. 93 with permission from the American Chemical Society, Copyright 2016. (b) Reproduced from ref. 94 with permission from Elsevier, Copyright 2018. (c) Reproduced from ref. 71 with permission from The Royal Society of Chemistry, Copyright 2019. (d) Reproduced from ref. 95 with permission from Elsevier, Copyright 2018.

synthesized *via* the COF-on-MOF strategy, where MCA was prepared by reacting melamine and cyanuric acid (Fig. 10d).[95]

2.3 COF-to-COF heterostructures

Imine-, azine-, hydrazone- and enamine-linked COF frameworks can be combined with other types of COFs and MOFs and serve as sieving membranes. Although COF membranes have been investigated, continuous progress on this area is highly restricted. In 2018, Fan *et al.* constructed a bilayer COF-to-COF membrane, which was prepared by synthesizing a 2D-COF layer over the another type of 2D-COF layer. The 2D-COFs of imine-linked COF-LZU1 and azine-linked ACOF-1 were used as building blocks due to their hexagonal pore structure.[96] Ying *et al.* developed cationic TpEBr and anionic TpPa-SO_3Na nanosheets, where the two building blocks with opposite charges were assembled to form an ultrathin membrane architecture. Consequently, different effects were integrated, forming ultrathin compact layers.[97]

3. Design principles and synthetic approaches

High surface energy is often generated at the interfaces between different MOFs or COFs because of their various morphologies.[98] Hence, suitable methods to prepare core–shell MOF-on-MOF and other types of MOFs- or COFs-based heterostructures must be explored (Fig. 11). Among the diverse preparation methods, seed-mediated growth, epitaxial and internally extended growth, and ligand exchange are usually used for the synthesis of core–shell MOF-on-MOF heterostructures. Anisotropic growth and induced growth, internal and epitaxial growth, and template methods are also applied for the development of other types of MOF-on-MOF heterostructures. The interfacial design strategy, one-step synthesis method, and *in situ* polymerization approaches have been explored for MOF@COF hybrids. Temperature-swing solvothermal synthesis and LBL assembly methods are appropriate for the construction of COF-to-COF hybrids. This work provides the design principles and reviews the synthetic approaches that correspond to the classifications of MOF/COF-based hybrids with different nanostructures and morphologies.

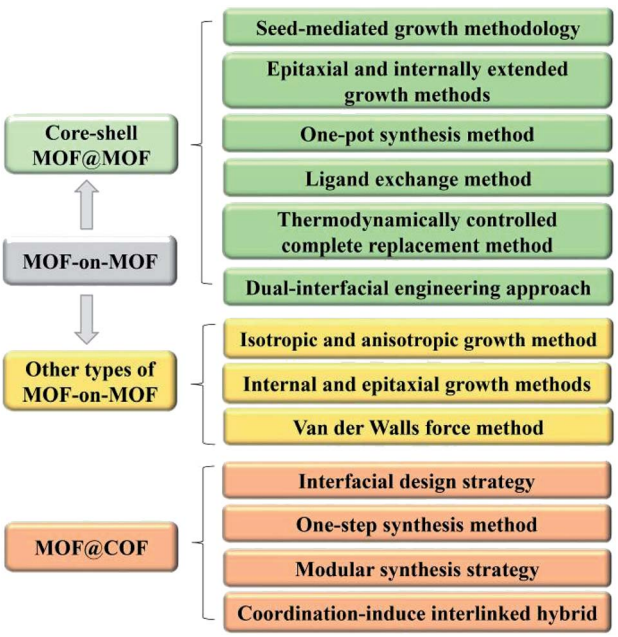

Fig. 11 Synthetic approaches for diverse heterostructures of MOF/COF-based hybrids.

3.1 MOF-on-MOF heterostructures

Owing to the well-defined and modulated heterocompositions and heterostructures of MOF-on-MOF nanohybrids, they have been explored as efficient platforms to overcome the inherent shortcomings in basic performances of their components (*e.g.*, poor chemical stability, structural stability, and crystallinity) and realize desirable and applicable properties (*e.g.*, reactivity, functionality, and thermodynamic stability).[42,99] Growing a secondary MOF shell on an MOF core can efficiently form complex heterostructures that protect the inner MOF cores and afford functional domains of the MOF shell in MOF hybrid materials. Different strategies for the fabrication of core–shell MOF@MOF heterostructures have been developed, such as seed-mediated growth, one-pot synthesis, epitaxial and internally extended growth, ligand exchange, and surfactant-mediated overgrowth. As an alternative method, the synthesis method of MOF-on-MOF hybrids shows potential in constructing well-defined MOF hybrids with a heterogeneous interface between two different MOFs. Generally, two MOFs with lattice matching of their cell parameters are often used for the preparation of core–shell MOF-on-MOF hybrids by growing the second MOF using the isotropic growth method. Furthermore, MOF-on-MOF hybrid materials are obtained by anisotropically growing the second MOF on the template MOF with mismatched cell parameters. These methods for the synthesis of MOF-on-MOF hybrids will be discussed in the following sections.

3.1.1 Core–shell MOF@MOF

3.1.1.1 Seed-mediated growth methodology. During the seed-induced growth procedure, the introduction of seed crystals in the starting preparation system of MOFs can accelerate their crystallization rate significantly. However, the traditional seed-induced growth approach for the preparation of core–shell MOF@MOF hybrids often has shortcomings, such as the possible nucleation of the shell MOF in solution and seed aggregation,[37] thus leading to structural incompleteness and reduction in the desired performances for the hybrids. In 2015, Yamauchi's group prepared core–shell ZIF-8@ZIF-67 hybrids using the seed-mediated growth method, in which ZIF MOFs were synthesized *via* the coordination reaction between diverse metal clusters and imidazole-related ligands. ZIF-8 crystals were explored as the core, while ZIF-67 was used as the shell. ZIF-8 seeds with a uniform size of approximately 50 nm were prepared *via* the coordination of Zn^{2+} ions and 2-methyl-1*H*-imidazole (MeIm) using PVP as the capping agent. Co^{2+} ions

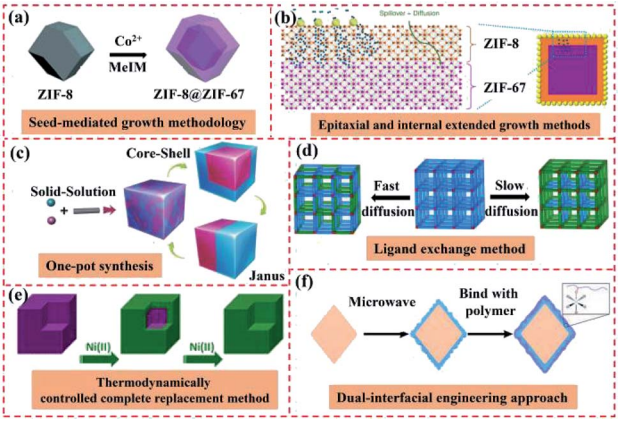

Fig. 12 Schematic illustration of the synthesis of core–shell MOF@MOF nanohybrids. (a) Reproduced from ref. 104 with permission from The Royal Society of Chemistry, Copyright 2017. (b) Reproduced from ref. 107, with permission from Springer, copyright 2018. (c) Reproduced from ref. 55 with permission from Wiley, Copyright 2017. (d) Reproduced from ref. 111 with permission from the American Chemical Society, Copyright 2017. (e) Reproduced from ref. 113 with permission from the American Chemical Society, Copyright 2012. (f) Reproduced from ref. 43 with permission from the American Chemical Society, Copyright 2020.

were then adsorbed on the ZIF-8 seed *via* coordination binding with the MeIm units, which were exposed on the surface. The ZIF-67 shell grew continuously over the ZIF-8 surface. The thickness of the ZIF-67 layer increased with an increase in the ratio of Co^{2+}/Zn^{2+}.[100–102] A series of mixed matrix membranes of the core–shell ZIF-67@ZIF-8 (ref. 56) and ZIF-L@ZIF-67 (ref. 103) has also been obtained using a similar method. Many reports focused on the core–shell ZIF-8@ZIF-67 hybrids,[100–102,104] ZIF-67@ZIF-8 (ref. 56 and 105) and other types of core–shell MOF@MOF[18,106] were obtained *via* the seed-mediated growth methodology (Fig. 12a). For these core–shell MOF@MOF heterostructures, ZIF-based crystals are often used as the seeds, whereas similar lattice ZIF networks are explored as the core. However, the preparation steps for the seed-mediated growth methodology are complicated, the production yield is low, the seeds tend to agglomerate, and pollution is generated by the residue from seed synthesis. Furthermore, lattice matching of the two MOF components is usually needed for the preparation of the core–shell MOF@MOF hybrids to ensure the alignment of the building units of the MOF core and MOF shell. Thus, these disadvantages greatly limit the construction of core–shell MOF hybrid materials using this method, hampering their extensive applications.

3.1.1.2 Epitaxial and internally extended growth. Core–shell MOF@MOF hybrids with the same ligand length and topological structure are usually easily integrated, where the second MOF shell can be grown over the MOF core surface *via* the internally extended growth method. For example, core–shell structured ZIF-8@ZIF-67 and ZIF-67@ZIF-8, and other Matryoshka-type $(ZIFs@)_{n-1}ZIFs$ (*e.g.*, tri-, tetra-, penta-, hexa-,hepta- and octa-layered ZIFs) were obtained by stepwise (batch-wise) liquid-phase epitaxial growth (Fig. 12b). The ZIF cubes were firstly prepared as the core crystals, and then added to a fresh solution containing metal ions, linkers, and CTAB surfactant, resulting in heterogeneous nucleation on the ZIF core *via* vertically epitaxial growth owing to the matched lattice parameters.[107]

For the core–shell MOF@MOF hybrid materials prepared using two MOFs with different ligands and morphological structures, it is difficult to precisely control the regular epitaxial growth owing to their high surface energy. These types of MOF@MOF heterostructures are usually synthesized *via* surfactant-mediated overgrowth. Surfactants, such as CTAB and PVP, can efficiently modulate the formation of MOF@MOF heterostructures by lowing their surface energy.[44] Therefore, the conformation and orientation of MOFs on solid surfaces can be sustained by using cationic surfactant capping agents despite their minimal structural similarity. Tsung's group developed even UiO-66@ZIF-8 heterostructures. As is known, ZIF-8 and UiO-66 have distinct chemical structures and morphologies. Zn clusters and imidazolate were found in the ZIF-8 crystals and $Zr_6O_4(OH)_4$ clusters and dicarboxylate linkers were present in UiO-66. With assistance from CTAB, homogeneous ZIF-8 outer layers were generated on homogeneously distributed UiO-66 crystals, thus forming the UiO-66@ZIF-8 hybrid.[44] A core–shell NH_2–MIL-101(Al)@ZIF-8 nanoflower was also prepared *via* an internal extended growth mode under PVP regulation. PVP molecules with long-chains were aligned along the [001] plane direction because of the high surface density of Cu(II). The efficient capping of PVP in the [001] plane greatly improved the formation of ZIF-8 from polyhedra to nanosheets by lowering its surface energy.[59] Moreover, diverse core–shell or striped hetero Ln-MOF crystals have been synthesized *via* the anisotropic epitaxial growth method. Monometallic LIFM-18/19(Eu) crystals were prepared using TMPBPO and Eu nitrate through a simple diffusion method, followed by immersion in an acetone/water mixture solution (v/v = 3/1) containing saturated $Tb(NO_3)_3 \cdot 3H_2O$ and TMPBPO. The second layer was propagated around the original core crystal due to the slow diffusion of acetone, thus forming a bimetallic hierarchical Eu@Tb-MOF hybrid.[108]

In addition to the use of surfactants, oriented hierarchical MOF heterostructures can also be constructed by dedicatedly choosing MOF seeds with similar ligands as the second MOF to match the crystal lattice. This leads to the epitaxial growth of the second MOF over the MOF seed with a small lattice mismatch. As shown in Fig. 13, three different 0D PCN-608 NPs and 1D NU-1000 nanorods, and 2D PCN-134 nanoplates were applied as templates for epitaxially growing PCN-222 nanorods. Depending on the size, shapes, and dimensionalities of these MOF cores, three different types of MOF heterostructures were achieved owing to the lattice mismatch between PCN-222 and the MOF seeds by selective epitaxial growth.[68]

3.1.1.3 One-pot synthesis. Among the different preparation approaches, one-pot synthesis is the most convenient to combine the multiple functionalities and performances of each component in a single platform, and thus is often applied to prepare MOF@MOF heterostructures.[63] The core–shell MOF@MOF hybrids with structural integrity constructed *via* the one-pot synthesis method[109] can remarkably avoid the possibility

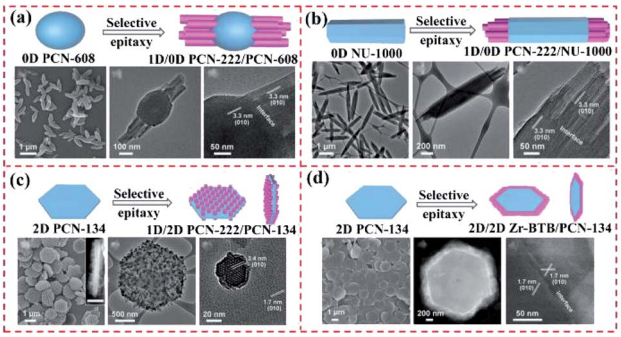

Fig. 13 Scheme of the synthesis of (a) 1D/0D PCN-222/PCN-608, (b) 1D/1D PCN-222/NU-1000, (c) 1D/2D PCN-222/PCN-134 and (d) 2D/2D Zr-BTB/PCN-134 heterostructures. Reproduced from ref. 68 with permission from the American Chemical Society, Copyright 2020.

of producing a new surface and reduce the requirements of incipient surface energy. As shown in Fig. 12c, Guo *et al.* proposed the prototypical bimetallic ZIF-8/ZIF-67 heterostructures within a single MOF crystal due to distinct reaction kinetics, leading to partial distribution of different metals during the formation of the MOF.[55] Similar sizes of metal ions readily were adapted to blend in the same porous framework. Uniform distributions of the two metals in the ZIF-8/ZIF-67 heterostructures were obtained at a high Co/Zn ratio of Co^{2+} and Zn^{2+} ions in the initial solution. The ZIF-8/ZIF-67 heterostructures were observed at a low Co/Zn ratio concentration gradient from Co-rich cores to Zn-rich shells. When Co^{2+} was added initially, the core–shell ZIF-67@ZIF-8/67 hybrids were produced, and their core/shell thickness was modulated by the reaction time interval. In contrast, when Zn^{2+} was introduced initially, only irregular aggregates were produced because of the low nucleation capability of Zn^{2+}.

In addition to the ZIF-8/ZIF-67 heterostructures obtained from MOFs with the same morphology and similar sizes, core–shell MOF@MOF nanostructures have also been obtained *via* the one-pot synthesis method using MOFs with diverse crystal lattices. Zhou's group developed the PCN-222@Zr-BPDC hybrid *via* one-pot synthesis. The individual components of PCN-222@Zr-BPDC displayed mismatching lattices. The strong binding interaction between TCPP and metal cations resulted in fast homogeneous nucleation. By contrast, BPDC with low connectivity often took longer for the preparation of crystals than TCPP under similar conditions. However, heterogeneous nucleation occurred faster than its homogenous counterpart because the seed crystal was used as a core for growing the second MOF.[30] Besides the ZIF@ZIF and PCN@UiO core–shell structures, monodisperse MOF@MOF comprised of two PBAs was also prepared *via* the one-pot synthesis strategy.[63]

3.1.1.4 Ligand exchange. The post-synthesis ligand exchange method (PSE) exhibits some intrinsic advantages, such as operational simplicity, widespread generality, and thus extensive applications.[110] PSE is typically performed by incubating MOF crystals in a solution containing another pure ligand in the presence of a suitable solvent (DMF or water). Two possible structures of the core–shell and uniformly distributed MOF@MOF heterostructures can be constructed using this technique. A homogeneous and mixed organic building blocks was achieved, in which ligand diffusion in the MOF was faster than its exchange. When the diffusion in the MOF was slow or if the exchange was faster at the edges of the crystal, the core–shell MOF@MOF nanohybrid was obtained (Fig. 12d).[111] Moreover, the core–shell ZIF-67@Co-MOF-74 hybrid was constructed by exchanging the ligands on the ZIF-67 surface with 2,5-dihydroxyterephthalic acid (DHTP) molecules. During the preparation of this nanohybrid, DHTP molecules showed higher coordination ability than 2-MeIm. When adding ZIF-67, DHTP molecules competed with 2-MeIm on the surface of ZIF-67 to coordinate with cobalt, thus generating Co-MOF-74 on ZIF-67. Finally, a ZIF-67@Co-MOF-74 core–shell structure was achieved.[112]

3.1.1.5 Thermodynamically controlled complete replacement. Lah's group reported a series of highly porous isostructural MOF heterostructures through the thermodynamically controlled complete replacement method, which was achieved by soaking the thermodynamically more stable MOF seeds as the core in a metal ion solution in the presence of ligands with a potentially less stable framework (Fig. 12e). This new type of MOF heterostructures demonstrated uniformly transmetalated framework structures, illustrating the boosted framework stabilities. The core–shell heterostructures were selectively transmetalated by kinetically controlling the replacement of the framework metal ions with the second MOF grown on the external MOF shell.[113]

3.1.1.6 Dual-interfacial engineering approach. Interfacial compatibility in mixed-matrix membranes can be realized *via* a dual-interfacial approach for the fabrication of MOF@MOF hybrids.[114] Fig. 12f shows that the ultrathin MOF-74 layer was grown on the MOF core *via* the dual-interfacial engineering method. This layer was comprised two interfaces of MOF–MOF and MOF-polymer. Between them, the interface at the two MOFs, MOF–MOF, was formed due to the lattice matching between the two MOFs and was strongly integrated by the coordination bonds between the metal and ligand because of the chemical similarity of the two MOFs.[43] Apparently, among the methods for constructing diverse MOF@MOF hybrids, the seed-mediated growth methodology is feasible for the preparation of MOF@MOF heterostructures with a matched lattice, such as ZIF-based hybrids. Meanwhile, the epitaxial and internally extended growth methods are helpful for the development of MOF@MOF hybrids using various MOFs. In addition, the presence of a surfactant can lower the surface energy at the interface between two MOFs, thereby facilitating the formation of MOF@MOF hybrids from diverse ligands.

3.1.2 Other types of MOF-on-MOF. Besides the core–shell MOF@MOF heterostructures, other categories of MOF-on-MOF hybrids have also been constructed through unique synthetic methods, which are apparently different from that of the MOF@MOF hybrids.

3.1.2.1 Isotropic and anisotropic growth. Presently, several types of MOF-on-MOF nanohybrids, including In–MIL-88B-on-Fe–MIL-88, MIL-68@MIL-68–Br, MIL-68@MIL-68–X (X = NO_2 or NH_2), MIL-88B@MIL-88A, Fe–MIL-88B@Fe–MIL-88C, and

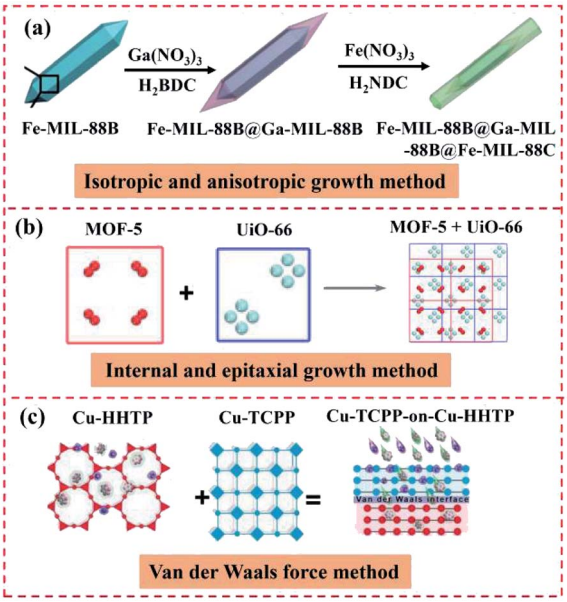

Fig. 14 Schematic illustration of the synthesis of MOF-on-MOF heterostructures. (a) Reproduced from ref. 47 with permission from the American Chemical Society, Copyright 2020. (b) Reproduced from ref. 35 with permission from Springer, Copyright 2019. (c) Reproduced from ref. 41 with permission from Wiley, Copyright 2019.

double-shelled Fe–MIL-88B@Ga–MIL-88B@Fe–MIL-88C, have been fabricated using isotropic or anisotropic growth and induced growth (Fig. 14a). Thus far, different MOF-on-MOF hybrid heteroparticles have been obtained by precisely modulating the isotropic and/or anisotropic nanoscale growth of various MOFs. Fe–MIL-88B, Ga–MIL-88B, and In–MIL-88B have been used for the heterometalation of MOF hybrids *via* the isotropic and anisotropic growth methods. Fe–MIL-88B nanorods with a hexagonal 3D structure were first prepared and explored as seeds for growing the secondary MOFs. The MOF-on-MOF heterostructure was obtained by hybridizing Fe–MIL-88B and M–MIL-88B (M = Ga or In).[47] MIL-68–Br and MOF-NDC (NDC stands for naphthalene-1,4-dicarboxylic acid) were isotropically and anisotropically grown on a microMIL-68. The isotropic growth of MIL-68–Br on the MIL-68 template led to the production of the core–shell-type MIL-68@MIL-68–Br.[42] The atypical lopsided core–shell of MIL-88B@MIL-88A has also been constructed *via* the unbalanced growth of an MOF-on-MOF hybrid. Although MIL-88A and MIL-88B had a large overall mismatch in their cell parameters because of the introduction of diverse organic linkers, the abnormal anisotropic MOF-on-MOF hybrid was obtained due to the analogous ab plane in the core and shell. Initially, nano-scale hexagonal MIL-88B rods were prepared, which then acted as a template to achieve the MIL-88B@MIL-88A hybrid by growing MIL-88A.[49] The MOF hybrid of the MIL-88B or MIL-88C structure was similarly gained *via* the isotropic or anisotropic preparation method because these two MOFs possessed different components and/or cell lattices. Ga–MIL-88B was isotopically grown on the Fe–MIL-88B core, showing well-matched cell lattices and different components. Fe–MIL-88C was also grown on MIL-88B with mismatched cell lattices and diverse structures, resulting in single-shelled Fe–MIL-88B@Fe–MIL-88C and double-shelled Fe–MIL-88B@Ga–MIL-88B@Fe–MIL-88C hybrids.[50] However, to date, the isotropic and anisotropic growth methods have only been used to prepare a series of MIL-based MOFs. Wide varieties of MOF@MOF heterostructures should be constructed in the near future.

3.1.2.2 Internal and epitaxial growth. To date, only a few core–shell MOF@MOF heterostructures have been obtained *via* the epitaxial growth method due to the picky designs of more than two MOFs with analogous crystal structures in one nanoparticle. Gu *et al.* used the internally extended growth method to prepare hierarchical MOF composites and overcome the restriction of the lattice matching. NH_2–UiO-66(Zr) and NH_2–MIL-125(Ti) were integrated to form the MOF-on-MOF heterostructure by implementing the internally extended growth method. NH_2–UiO-66(Zr) was interacted with the NH_2–MIL-125(Ti) precursors with the help of PVP. Consequently, the NH_2–MIL-125(Ti) nuclei were assembled with NH_2–UiO-66(Zr) to produce the hybrid.[70] Kim's group constructed MOF@MOF hybrids with matched interface configurations (Fig. 14b).[35] The results showed a MOF-5 crystal that had grown on the {111} planes of the octahedral HKUST-1, thus forming the HKUST1@MOF-5 hybrid. Zhang's group developed a novel MIL-88B-on-UiO-66 hybrid using the heteroepitaxial growth method.[52] Accordingly, coordination occurred between the linear linkers and coordinately unsaturated metal modes, giving a layer of coordinately unsaturated ligands by epitaxial growth.

3.1.2.3 van der Waals force method. As is known, van der Waals force can be freely used to combine different materials, differing from chemical bonding at the interface between two diverse materials. For instance, Cu-TCPP layers were deposited on semiconductive Cu-HHTP layers using van der Waals forces, forming oriented MOF-on-MOF thin films, which can overcome the lattice mismatching issue (Fig. 14c). Consequently, Cu-TCPP-on-Cu-HHTP thin films were obtained.[41]

3.2 MOF@COF heterostructures

Besides MOF-on-MOF heterostructures, integrating MOFs with COFs also can overcome the limitations of each component. A few methods have been explored for the hybridization of COFs and MOFs and showed extensive applications in diverse fields. The preparation methods of MOF@COF hybrids include interfacial design strategy, one-step synthesis method, modular synthesis strategy, and coordination-induced interlinked hybrid strategy, which will be discussed below.

3.2.1 Interfacial design strategy. The interfacial design strategy involves coating COF layers on size-selective MOF cores to construct MOF@COF hybrids.[78] Zhang's group developed core–shell NH_2–MIL-68@TPA-COF hybrid materials by controlling the synthesis of TPA-COF on NH_2–MIL-68 (Fig. 15a). The prepared NH_2–MIL-68 was functionalized with TFPA for the formation of NH_2–MIL-68(CHO). TPA-COF was then *in situ* formed on the NH_2–MIL-68(CHO) surface by covalent connection with TFPA and TAPA *via* condensation reaction. Hence, the

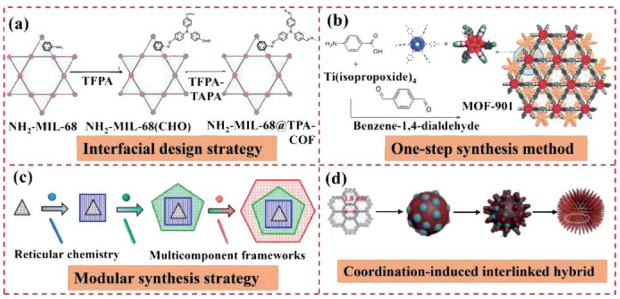

Fig. 15 Schematic illustration of the synthesis of MOF@COF heterostructures. (a) Reproduced from ref. 74 with permission from Wiley, Copyright 2018. (b) Reproduced from ref. 116 with permission from the American Chemical Society, Copyright 2016. (c) Reproduced from ref. 117 with permission from the American Chemical Society, Copyright 2020. (d) Reproduced from ref. 118 with permission from Wiley, Copyright 2019.

NH_2–MIL-68@TPA-COF hybrid was prepared.[74] The NH_2–UiO-66/TpPa-1-COF hybrid also was gained by combining NH_2–UiO-66 with TpPa-1-COF. For this preparation system, NH_2–UiO-66 was modified with slightly extra Tp and used as a template for the synthesis of TpPa-COF.[115] Furthermore, the size-selective MOF cores were coated with COF layers *via* an interfacial design strategy to improve the polymer-filler compatibility. For this, the UiO-66–NH_2 crystals were applied as the MOF component, and TpPa-1 was prepared *via* aldehyde-amine Schiff base reaction and irreversible enol-to-keto tautomerization.[89] For the synthesis of these MOF@COF hybrids, the amino-functional MOFs afforded efficient interface for binding the COF layer to fabricate excellent MOF@COF heterostructures.

3.2.2 One-step synthesis method. As mentioned in Section 3.1.1.3, integrating multiple functionalities into one system can lead to the generation of porous heterostructures. Yaghi's group prepared a crystalline 2D MOF@COF nanohybrid using a one-step synthesis strategy (Fig. 15b). $Ti_6O_6(OCH_3)_6(AB)_6$ (AB = 4-aminobenzoate) was connected with benzene-1,4-dialdehyde by imine condensation, which is the typical reaction for COFs.[116] The NUT–COF–1@NH_2–MIL101(Fe) heterostructure was synthesized by growing NUT–COF–1 on NH_2–MIL101(Fe) using the one-pot synthesis method *via* the formation of an imine group and boroxine ring. Thereby, the condensation between 2-aminoterephthalic acid and FPBA led to the covalent binding of FPBA to the NH_2–MIL-101(Fe) surface.[90] Additionally, the Hf-UiO-AM@MOF-PEG nanocomposite was also developed using the one-pot synthesis method by growing TAPC, terephthalaldehyde, and PEG5k-NH_2 on the surface of Hf-UiO-AM.[82]

3.2.3 Modular synthesis strategy. Small individual modules can be obtained by separating an integrated system and interchanging its components.[70] With this modular synthesis method, diverse structures have been obtained by feasibly changing the organic linkers (Fig. 15c). Zhou's group developed hierarchical MOF@COF structures by using the modular synthesis strategy. COF-303, which was synthesized *via* the reversible imine condensation between tetratopic aldehyde, tetrakis(4-formylphenyl)methane, and a ditopic amine, PDA, was first used as a template for growing the secondary shell MOFs. Finally, the multicomponent hierarchical COF-303@MOF-5 hybrid was prepared.[117]

3.2.4 Coordination-induced interlinked hybrid. Considering that the organic groups in the COF networks can tightly coordinate with the metal ions in MOFs (Fig. 15d), Sun *et al.* constructed a COF/Mn-MOF hybrid through the simple combination of a COF and MOF. Owing to the strong coordination reactivity of Mn ions, six-connected Mn centres in Mn-MOF were expanded to seven coordination with an additional linking for the electron-rich N atoms on the COF structure, leading to the formation of a COF/Mn-MOF hybrid.[118]

3.3 COF-to-COF heterostructures

Besides the methods of introducing functional groups in COFs and combining COFs with MOFs, COF-to-COF hybrids also have been developed to extend the application range of porous organic materials. To date, only two methods of temperature-swing solvothermal synthesis and LBL assembly have been applied for the development of COF-to-COF heterostructures (Fig. 16). Given that COF-LZU1 and azine-linked ACOF-1 have a similar conformation, the COF-LZU1-ACOF-1 bilayer membrane was fabricated through integration. COF-LZU1 was prepared *via* the reaction of 1,3,5-triformylbenzene with PDA, while ACOF-1 with high-crystallinity was synthesized by reacting TFB with hydrazine hydrate. Owing to the feasible preparation of COF-LZU1 *via* TFB and PDA, the COF-LZU1-ACOF-1 bilayer was easily synthesized through a facile temperature-swing solvothermal synthesis.[96] Zhao's group proposed the preparation of the TpEBr@TpPa-SO_3Na hybrid using two intrinsically charged ionic covalent–organic nanosheets with opposite charges and explored it as building blocks for the assembly of ultrathin membrane architectures with reduced apertures under the driving force of electrostatic attractive interaction.[97]

Diverse approaches can be explored for the construction of various types of MOF-on-MOF and MOF@COF heterostructures. For instance, the seed-mediated growth method is suitable for the synthesis of core–shell MOF@MOF hybrids using ligands with similar lattices. The one-pot synthesis method and epitaxially/internally extended growth method are beneficial for the preparation of MOF@MOF hybrids using different ligands. The isotropic and anisotropic growth methods are helpful for MOF-on-MOF hybrids that use ligands with a matched lattice. Furthermore, the functionality of MOFs is essential for the

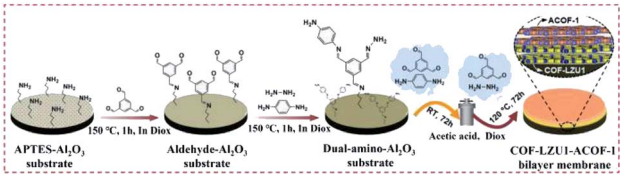

Fig. 16 Schematic illustration of the synthesis of COF-to-COF heterostructures. Reproduced from ref. 96 with permission from Wiley, Copyright 2018.

fabrication of MOF@COF to bind different layers into an integrated system. Choosing a suitable preparation approach is essential for the development diverse MOF/COF-based hybrids with different nanostructures. The utilization of surfactants is a feasible way to control the formation mechanism and behavior of MOF/COF hybrids.

4. Applications of MOF/COF-based heterostructures

Due to the efficient integration of different types of MOFs and COFs, the formed diverse MOF-on-MOF, MOF@COF, and COF-to-COF heterostructures often exhibit excellent crystal and structural performances, such as extended skeletons, large specific surface area, excellently electrochemical activity, and synergistic effect among their different components. Therefore, these MOF/COF-based heterostructures show practical applications in different fields, including catalysis, gas adsorption/separation, biosensing and biomedicine.

4.1 Catalysis

Various MOF/COF-based heterostructures have been developed as multifunctional catalysts, such as electrocatalysts, photocatalysts, photodegradation catalysts for pollutants and heavy metal ions, and molecular catalysts. According to their application field, these MOF/COF-based heterostructures are mainly classified into three categories, including photocatalysts for energy transfer, photodegradation catalysts, and molecular catalysts for organic synthesis (Fig. 17). In this section, the extensive and promising applications of these heterostructures will be highlighted and discussed.

4.1.1 Photocatalysts for energy transfer. Various photocatalysts such as MOFs,[119] COFs,[10] noble metals, carbon-based dots,[120] g-C_3N_4,[121] and Bi-based compounds[122] have been developed and used for energy transfer. Compared with conventional photocatalysts, MOFs and MOF-based hybrids exhibit some excellent merits, such as well-defined topology and porous nanostructure, which can greatly boost the transfer and diffusion of molecules and benefit the photo-induced reaction.[123] Because of porous nanostructure and large surface area of MOFs, large amounts of active catalytic sites are exposed and enhanced for catalytic reactions.[124] Concurrently, COFs and their related composites have been also utilized as efficient photocatalysts for driving diverse reactions, such as water splitting, organic reactions, hydrogen production, and water oxidation.[10] Compared with traditional semiconductors, COFs often demonstrate some advantages, such as designable nanostructure, large surface area, high chemical and thermal stability, and extended and π–π conjugated structures in-plane and in the stacking direction.[125] To date, various MOF/COF hybrids have been used to modulate their structure and functionalities, reserving their large surface area and high porosity and crystallinity, and thus showing vast applications in diverse catalytic fields.

MOF@COF hybrids inherit the advantages of their parent components, and thereby have wide potential applications as photocatalysts for driving diverse reactions.[115] Therefore, the good photoconductivity and/or fast charge transfer features of COFs can remedy the poor conductivity of MOFs.[126] Owing to the tunable features of both MOFs and COFs, chemical interactions can occur between them,[73] thus leading to some specific functionalities. This operation can avoid the removal of COF layers and result in a homogeneous integration, which can be

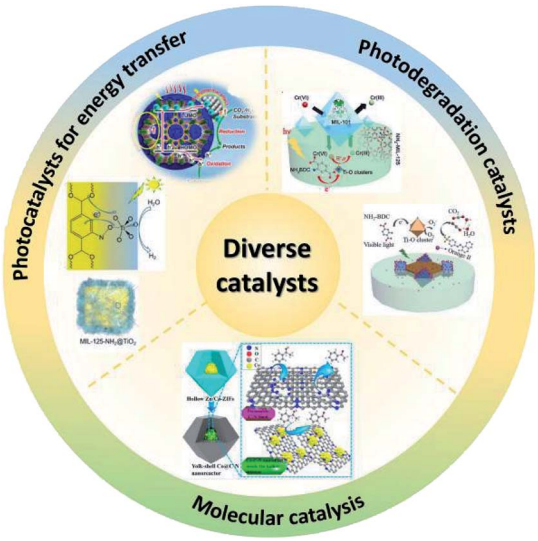

Fig. 17 Schematic diagram of MOF/COF-based hybrids as diverse catalysts.

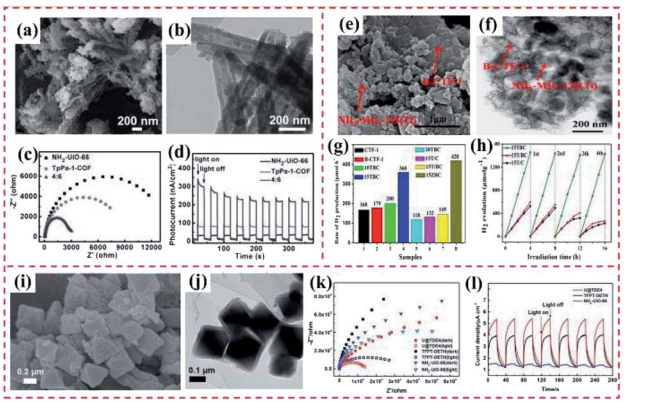

Fig. 18 (a) and (b) Scanning electron microscopy (SEM) and transmission electron microscopy (TEM) images of TpPa-1-COF and NH_2–UiO-66/TpPa-1-COF (4 : 6). (c) Electrochemical impedance spectroscopy (EIS) Nyquist plots of NH_2–UiO-66, TpPa-1-COF and NH_2–UiO-66/TpPa-1-COF (4 : 6) hybrid material. (d) Transient photocurrents measurements. Reproduced from ref. 115 with permission from Wiley, Copyright 2018. (e) SEM and (f) TEM image of 15TBC. (g) Rate of hydrogen evolution over the different samples under visible light irradiation. (h) Cycling runs of the as-prepared catalysts under visible light irradiation. Reproduced from ref. 73 with permission from Elsevier, Copyright 2019. (i) SEM and (j) TEM image of U@TDE4. (k) EIS Nyquist plots and (l) photocurrent density curves of NH_2–UiO-66, TFPT–DETH and U@TDE4 in 0.1 mmol L^{-1} Na_2SO_4 solution under visible light irradiation. Reproduced from ref. 81 with permission from The Royal Society of Chemistry, Copyright 2020.

explored as diverse photocatalysts. Lan's group provided an integrated porous NH_2–UiO-66/TpPa-1-COF hybrid with superior photocatalytic H_2 evolution under visible light (Fig. 18a–d). After modulation of its basic performances, the NH_2–UiO-66/TpPa-1-COF (4 : 6) hybrid displayed a high photocatalytic H_2 evolution rate of 23.41 mmol g^{-1} h^{-1}, 20-times higher than that of TpPa-1-COF. Because of its outstanding light absorbance ability, TpPa-1-COF in NH_2–UiO-66/TpPa-1-COF played a light-harvesting role upon visible light irradiation. The photogenerated electrons of TpPa-1-COF transferred from the valence-band (VB) to conduction-band (CB), which then further rapidly migrated to the CB of NH_2–UiO-66 *via* covalent bonding interaction, ensuring that the photogenerated electrons oppositely moved to holes. The efficiently separation of electrons in the CB of NH_2–UiO-66 reduced H^+ in the presence of a Pt co-catalyst.[115] Li *et al.* presented the hierarchical NH_2–MIL-125(Ti)/B-CTF-1 (15TBC), which displayed superior photocatalytic ability for hydrogen production, with a transfer rate over 15 wt% (15TBC) and maximum photocatalytic activity of 360 μmol h^{-1} g^{-1} under visible light irradiation (Fig. 18e–h). The good photocatalytic ability of the MOF/COF hybrids was attributed to the large amounts of amide bonds formed between B-CTF-1 and MOFs. These functional groups are essential for both the enhancement of charge separation and the improvement of photocatalysis stability. For this novel photocatalysis system, electrons and holes were generated from both NH_2–MIL-125(Ti) and B-CTF-1, providing a new photocatalysis strategy based on an MOF/COF hybrid.[73] Similarly, the NH_2–UiO-66@TFPT–DETH nanohybrid exhibited a high hydrogen evolution rate of 7178 mmol g^{-1} h^{-1}, which was 3-fold higher than that of TFPT–DETH. Electron–hole pairs were produced from both NH_2–UiO-66 and TFPT–DETH under visible light illumination (Fig. 18i–l). For this system, photogenerated electrons migrated rapidly from NH_2–UiO-66 CB to TFPT–DETH CB, while holes transferred in the opposite direction. The enhanced photocatalytic activity of the core–shell NH_2–UiO-66@TFPT–DETH heterostructure was mainly due to the synergistic effect originated from the NH_2–UiO-66@TFPT–DETH heterostructure, such as the extension of light absorption, the improvement in exaction dissolution and transfer, and high porous structures.[81]

Beside the exploration of photocatalysts for H_2 evolution based on MOF@COF, Guo reported core–shell ZIF-67@MOF (MOF = Co-MOF-74, Co-BDC, Co–NH_2BDC and Co-BTC) catalysts for driving water oxidation reaction under visible light. They revealed that the core–shell ZIF-67@Co-MOF-74 with an MOF shell of 50 nm showed the oxygen evolution production of 15 μmol after 8 min, while that of ZIF-67 and Co-MOF-74 was 9.8 and 11.8 μmol, respectively. The core–shell ZIF-67@Co-MOF-74 hybrid showed enhanced catalytic ability due to the following factors: (i) abundant crystal defects formed on the rough surface of the core–shell MOFs substantially improved the exposed metal centers and their sufficient contact; (ii) abundant-OH and –COO groups on the core–shell surface were helpful for adsorbing water molecules, leading to overall water splitting to produce oxygen; and (iii) the interface of the core–shell MOFs exhibited high conductivity, further boosting the electron transport and resulting in the separation of electrons and holes, which greatly inhibited charge recombination.[112]

Additionally, Lu *et al.* used the NH_2–MIL-125@TAPB-PDA hybrid as a good photocatalyst for selectively oxidizing alcohols. The results demonstrated that the addition of an appropriate content of COF greatly facilitated the electronic and optical performances, and thus improved the photocatalytic ability distinctly. The NH_2–MIL-125@TAPB-PDA-3 composite with a 20 nm-thick COF shell had the highest production (94.7%) of benzaldehyde, which was 2.5- and 15.5-times higher than that of NH_2–MIL-125 and COF, respectively. The excellently photocatalytic ability of the NH_2–MIL-125@TAPB-PDA-3 hybrid was ascribed to the boosted charge transfer between the two parts.[127] Based on the above discussion about the photocatalytic activity of MOF@COF heterostructures, it can be deduced that combining the two components of MOFs and COFs can greatly enhance their catalytic performance.

4.1.2 Photodegradation catalysts. Wastewater always contains some hazard components, which are toxic to human beings and cannot be completely degraded by conventional biochemical processes.[128] Thus, it is essential to develop the efficient techniques for treating wastewater, such as photocatalysis under visible-light.[129] Photocatalysis is usually used for degrading these compounds because of its low-cost and high efficiency.[130] In the photocatalysis technique, the key factor is the use of a photocatalyst, which can efficiently transfer solar energy into chemical energy, thus resulting in the degradation of pollutants.[131] Currently, different photocatalysts have been developed for degrading or removing pollutants from the aqueous environment such as TiO_2 and its composites, transition metal compounds, carbon nitrides, noble metals, and porous-organic frameworks.[10,132–134] Among them, the advantages of MOFs can endow them with superior photocatalytic performances.[135] MOFs not only can increase the reaction activity near by the catalytic active sites by selectively adsorbing molecules, but also can participate in the charge transfer process by modifying them with functional groups,[136,137] as well as being used as carriers for supplying photocatalytic active sites.[138] Currently, different types of MOFs and MOF-based composites have been developed for the photocatalytic treatment of pollutants and antibiotics.[138–141] However, some disadvantages of pure MOFs, such as their poor photosensitivity, low separation ability of electron–holes and photocorrosion problems, as well as their hydrophilic property can remarkably reduce their catalytic activity and reduce their structural stability in a humid environment.[142] Thus, these shortcomings of pure MOFs limit their further practical application for degrading pollutants. Although plenty of work has been devoted to the construction of MOF composites, their limited classes and complex preparations restrict their applications as photocatalysts. As previously mentioned, integrating various MOFs can combine the functionalities of different MOFs, thus enhancing their interfacial properties. The synergistic effect in different MOFs is helpful for enhancing target functions. Different MOF-on-MOF or MOF@COF heterostructures have been fabricated and utilized as the efficient photocatalysts for

Table 1 Photodegradation MOF/COF-based hybrid catalysts

Materials	Contaminant	Irradiation time (min)	Initial concentration (mg L^{-1})	Removal%	Adsorption capacity	Ref.
NH_2–MIL-101(Al)@ZIF-8	Cu(II)	—	10–250	—	526.74 mg g^{-1}	59
MIL-101@NH_2–MIL-125	Cr(VI)	120	10	72	—	70
Fe_3O_4@HKUST-1/MIL-100(Fe)	MB	180	20	>90	—	144
MIL-125@ZIF-8	Orange II	120	50	97.3	—	69
NH_2–MIL-68@TPA-COF	RhB	40	20	—	—	74
NH_2–MIL-125(Ti)/TTB-TTA	MO	20	10	>90	—	89
MOF-5/COF (M5C)	AO and RhB	8	5	>90	—	145

degrading various pollutants, such as heavy metal ions and organic dyes (Table 1).

4.1.2.1 Removal and photodegradation of heavy metal ions. Heavy metal ions (Cu(II), Cd(II), Cr(VI), and Pb(II)) in water bodies are seriously harmful to human beings. The high accumulation of heavy metal ions not only can remarkably destroy the natural ecosystem but also can lead to serious damage to human beings.[143] Recently, Zhang *et al.* reported core–shell NH_2–MIL-101(Al)@ZIF-8 nanohybrids and explored their use as an adsorbent of Cu(II) (Fig. 19a). Considering the high binding of the imidazole nitrogen in ZIF-8 with Cu(II), the proposed NH_2–MIL-101(Al)@ZIF-8 hybrid exhibited a high adsorption efficiency (526.74 mg g^{-1}) toward Cu(II). In addition, the fluorescence performance of NH_2–MIL-101(Al) demonstrated a Cu(II)-dependent change, resulting in a superior selective/sensitive sensing performance in a broad linear range (1.5–625 mM), showing a low detection of limit (LOD) of 0.17 mM for Cu(II) (Fig. 19b and c).[59] Additionally, it is essential to adsorb Cr(VI) from wastewater due to its high toxicity toward organisms.[146] Kitagawa's group proposed a novel MIL-101(Cr)@NH_2–MIL-125(Ti) heterostructure (Fig. 19d), where the synergy between the two pure MOFs was beneficial for enhancing the degradation of Cr(VI). The MIL-101(Cr)@NH_2–MIL-125(Ti) exhibited an adsorption capacity for Cr(VI) of 3.16 mg g^{-1}. Apparently, the presence of MIL-101(Cr) supplied additional mesoporous channels for boosting the adsorption of Cr(VI) in the internal microporous NH_2–MIL-125(Ti) (Fig. 19e). However, Cr(VI) was not degraded by the single MIL-101(Cr). As shown in Fig. 19f, 72% of Cr(VI) was dislodged from the solution by MIL-101(Cr)@NH_2–MIL-125(Ti) after 120 min under visible light irradiation, while only 47% of Cr(VI) was removed by NH_2–MIL-125(Ti). It also displayed the band-gap energy of MIL-101(Cr)@NH_2–MIL-125(Ti) was identical to that of the pure NH_2–MIL-125(Ti).[70]

4.1.2.2 Adsorption and photodegradation of organic pollutants. Organic dyes have been vastly applied in diverse industrial production fields. Also, water containing organic dyes is released to the aquatic environment, resulting in severe pollution.[147] Thus, the removal and treatment procedures of organic dyes from water systems are extremely significant for protecting

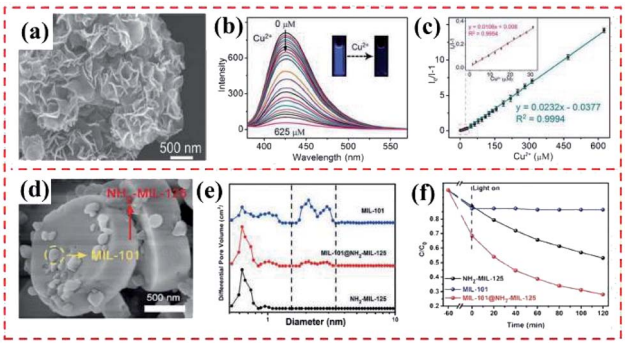

Fig. 19 (a) SEM image of NH_2–MIL-101(Al)@ZIF-8 core–shell nanoflower. (b) Fluorescence emission spectra of NH_2–MIL-101(Al)@ZIF-8 suspension (0.047 mM) upon the addition of various concentrations of Cu(II) under excitation at 325 nm. (c) Corresponding Stern–Volmer linear fitting curves of NH_2–MIL-101(Al)@ZIF-8 toward Cu(II) in a high concentration range. Reproduced from ref. 59 with permission from The Royal Society of Chemistry, Copyright 2018. (d) SEM image of typical MIL-101@NH_2–MIL-125 heterostructured hybrid crystal. (e) Pore width distribution based on the NLDFT model of MIL-101, NH_2–MIL-125, and MIL-101@NH_2–MIL-125. (f) Adsorption and photocatalytic degradation toward Cr(VI) with MIL-101, NH_2–MIL-125, and MIL-101@NH_2–MIL-125. Reproduced from ref. 70 with permission from Wiley, Copyright 2017.

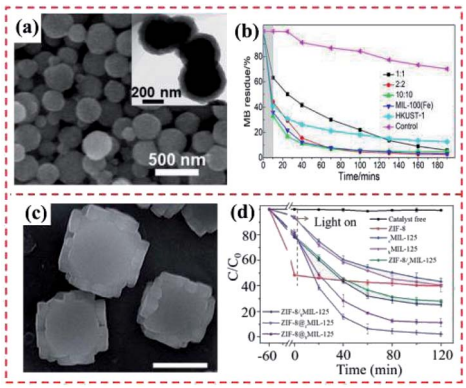

Fig. 20 (a) SEM and TEM images of the obtained Fe_3O_4@HKUST-1/MIL-100(Fe) (1 : 1) particles. (b) MB removal efficiency as a function of time with different types of hybrid materials. The shadowed area represents the experiments conducted in a dark environment. Reproduced from ref. 144 with permission from the American Chemical Society, Copyright 2019. (c) SEM images of $_b$MIL-125@ZIF-8. (d) Degradation efficiency of ZIF-8, $_c$MIL-125, $_b$MIL-125, $_c$MIL-125/ZIF-8, $_b$MIL-125/ZIF-8, $_b$MIL-125, $_c$MIL-125@ZIF-8 and $_b$MIL-125@ZIF-8. Reproduced from ref. 69 with permission from The Royal Society of Chemistry, Copyright 2020.

the environment and life.[148] Chen's group reported a series of hierarchically sandwiched Fe_3O_4@HKUST-1/MIL-100(Fe) hybrid materials and their application as photocatalysts to degrade methylene blue (MB) under visible light (Fig. 20a). In comparison with the individual or pristine MOFs, the obtained MOF-on-MOF hybrid demonstrated a substantially improved specific surface and small interior pore size. Meanwhile, the removal efficiency of MB by Fe_3O_4@HKUST-1/MIL-100(Fe) hybrid was comparable with pure Fe_3O_4@MIL-100(Fe) but with only half the layers (Fig. 20b).[144] Further, Liu *et al.* developed MIL-125@ZIF-8 heterostructures, where the high adsorption ability of ZIF-8 and the photocatalytic performance of MIL-125 were integrated (Fig. 20c). The developed MIL-125@ZIF-8 hybrid displayed a faster degradation rate of Orange II with a removal rate of 97.3% within 2 h under visible light irradiation, much higher than that of MIL-125 (54.6%) (Fig. 20d). The physically mixed ZIF-8/MIL-125 exhibited a much lower degradation efficiency in comparison to that of the MIL-125@ZIF-8 heterostructure, revealing the synergistic effect between MIL-125 and ZIF-8. These results verified that control over the site of ZIF-8 growth is vital for modulating the photocatalytic activity of MOF-on-MOF heterostructures.[69]

Besides the superior catalytic ability of MOF@MOF hybrids, there are many reports on the application of MOF@COF nanohybrids for the photodegradation of different pollutants. Zhang's group prepared a core–shell NH_2–MIL-68@TPA-COF hybrid material and employed it as an efficient photocatalyst for the visible-light driven degradation of rhodamine B (RhB) (Fig. 21a and b). Given that NH_2–MIL-68 possesses photocatalytic activity, NH_2–MIL-68@TPA-COF displayed a photocatalysis rate constant of 0.077 min^{-1}, 1.4-times higher than that of NH_2–MIL-68 (Fig. 21c and d). The detailed discussion on the basic characterization of the NH_2–MIL-68@TPA-COF nanohybrid revealed that the improved photocatalytic property of NH_2–MIL-68@TPA-COF was mainly ascribed to its large Brunauer–Emmett–Teller (BET) surface area and small band gap.[74] Further, He *et al.* prepared an NH_2–MIL-125(Ti)/TTB-TTA hybrid with outstanding photocatalytic activity. Specifically, NH_2–MIL-53(Al), NH_2–MIL-125(Ti) and NH_2–UiO-66(Zr) were utilized for doping TTB-TTA for the production of heterogeneous photocatalysts (Fig. 21e–g). Considering the well-matching band gaps between NH_2–MIL-125(Ti) and TTB-TTA, the obtained NH_2–MIL-125(Ti)/TTB-TTA hybrid illustrated remarkably photocatalytic activity for degrading methyl orange (MO) dye and colorless phenol under visible light irradiation owing to its intrinsic features of large surface area, porous nanostructure and high crystallinity. The self-photolysis of MO was very slight under visible light exposure in the absence of NH_2–MIL-125(Ti)/TTB-TTA, while the NH_2–MIL-125(Ti)/TTB-TTA catalyst showed a high photodegradation capacity toward MO (Fig. 21h and i). However, the photocatalytic activity of a physical mixture of NH_2–MIL-125(Ti) and TTB-TTA was inferior to that of NH_2–MIL-125(Ti)/TTB-TTA. This was mainly ascribed to the prominent role of the covalent binding in the NH_2–MIL-125(Ti)/TTB-TTA hybrid, which greatly enhance the transfer of photogenerated electrons.[89] An MOF-5/COF (M5C) hybrid was prepared *via* the hybridization of a zinc-based MOF and melamine-terephthaldehyde (Fig. 21j and k) and applied as a good sorbent to quickly and efficiently remove auramine O (AO) and RhB cationic dyes from aqueous media due to its combined forces. The obtained MOF-5/COF adsorbent displayed an adsorption efficiency of 17.95 and 16.18 mg g^{-1} for AO and RhB dyes, respectively, at pH 9.5. The results showed that AO and RhB molecules were planar, which were easily adsorbed by the MOF-5/COF hybrid *via* physisorption forces besides the MOF-5/COF cavities. Also, the AO and RB dyes were encapsulated in the cavities of MOF-5/COF and bound to MOF-5/COF through electrostatic interaction, hydrogen bonding, and van der Waals forces, as well as host–guest interactions with the MOF-5/COF cavities (Fig. 21l).[145]

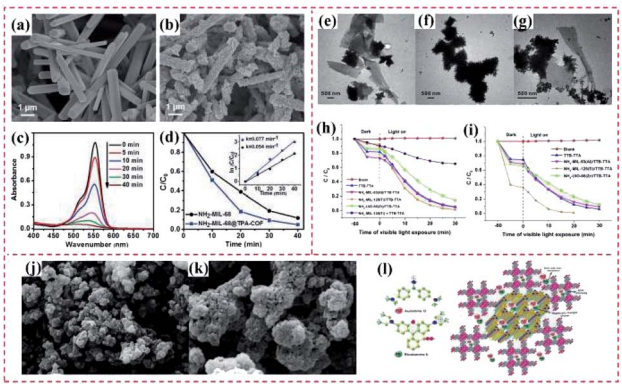

Fig. 21 SEM image of (a) NH_2–MIL-68 and (b) NH_2–MIL-68@TPA-COF. (c) UV-vis absorption spectra of RhB in the presence of NH_2–MIL-68@TPA-COF hybrid material upon visible light irradiation. (d) Comparison of photodegradation efficiencies of RhB in the presence of NH_2–MIL-68 and NH_2–MIL-68@TPA-COF. Reproduced from ref. 74 with permission from Wiley, Copyright 2018. TEM images of (e) NH_2–MIL-53(Al)/TTBTTA, (f) NH_2–MIL-125(Ti)/TTB-TTA and (g) NH_2–UiO-66(Zr)/TTB-TTA. (h) Photocatalytic degradation of MO (10 mg L^{-1}) over as-prepared photocatalysts under visible light irradiation. (i) Photodegradation of phenol (10 mg L^{-1}) over TTB-TTA, NH_2–MIL-53(Al)/TTB-TTA, NH_2–MIL-125(Ti)/TTB-TTA, NH_2–UiO-66(Zr)/TTB-TTA, and a physical mixture of NH_2–MIL-125(Ti) and TTB-TTA (NH_2–MIL-125(Ti) + TTB-TTA). Reproduced from ref. 89 with permission from Elsevier, Copyright 2019. (j) and (k) SEM images of M5C. (l) Interactions of the dyes with the adsorbent and proposed mechanism. Reproduced from ref. 145 with permission from the American Chemical Society, Copyright 2020.

Based on the above discussion, it can be deduced that only limited MOFs or COFs can be explored as photocatalysts for degrading pollutants or adsorbing the organic dyes or heavy metal ions. MIL-101(Cr), NH_2–MIL-125(Ti), NH_2–MIL-125(Ti), and MIL-100(Fe) are often integrated with other types of MOFs or COFs, showing improved photocatalytic activity. Thus, to further broaden the range of degradable pollutants, it is significant to develop some novel heterostructures based MOFs or COFs.

4.1.3 Molecular catalysis. Some noble metal catalysts, such as Au, Pt, Pd, and Ru, can be embedded within the pores of different MOFs and COFs, which can avoid the aggregation of these catalysts and improve their catalytic activity.[149] As mentioned previously, MOF-on-MOF and MOF@COF hybrids

Table 2 Molecular catalysis by MOF/COF-based hybrids

Catalyst	Substrate	Conversion (%)	Selectivity (%)	Time	Ref.
Pd@H–Zn/Co-ZIF	Ethylene hydrogenation	>80	>80	10 h	105
PCN-222(Fe)@Zr-BPDC	Epoxidation of alkenes	>99	—	12 h	30
PCN-222-Co@TpPa-1	Deacetalization-Knoevenagel condensation	99.3	—	10 h	71
UiO-67-BPY@UiO-66	Benzaldehyde	98	—	1 h	67
MOF-901	Polymerization of methyl methacrylate	87	—	18 h	116
UiO-66@SNW-1	Deacetalization-Knoevenagel condensation	99.6	99.6	12 h	79
MIL@NTU-1	Styrene oxidation	32	84	12 h	153
UiO-66–NH_2@COP@(2.34%)Pd	Hydrogenation of nitrobenzene	100	99.9	30 min	84
Ti-MOF@Pt@DM-LZU1	Hydrogenation of styrene	>99	>99	40 min	85

exhibit comprehensive performances, which can combine the advantages of different frameworks. Thereby, it can be expected that these heterostructures will display extensive applications in the molecular catalysis field (Table 2). Tsung' group prepared a homogeneous Pd–UiO–NH_2@ZIF-8 hybrid, where UiO-66–NH_2 served as the core MOF for the entrapment of Pd NPs, while ZIF-8 was conformably overgrown as the shell. Different hybrids, including Pd–UiO–NH_2 (before ZIF-8 overgrowth), Pd–UiO–NH_2@ZIF-8 (conformal shell), Pd–UiO–NH_2@ZIF-8 (fractured shell), and Pd–UiO–NH_2@ZIF-8 (synthesized in methanol in the presence of PVP) loading with Pd NPs (0.14 mg) were applied to analyze the catalytic activities for ethylene hydrogenation. The four samples showed comparable catalytic performances because ethylene molecule only had a small kinetic diameter of 2.5 Å, allowing ethylene to easily diffuse through UiO-66–NH_2 and ZIF-8. Afterward, the ethylene molecule was accessible to Pd owing to its smaller kinetic diameter than the aperture size of ZIF-8 (3.4 Å) and UiO-66 (6.0 Å). High catalytic efficiency was observed for Pd-UiO–NH_2 when cyclohexene hydrogenation was carried out. On the contrary, only negligibly catalytic activities of Pd–UiO–NH_2@ZIF-8 (conformal shell) and Pd–UiO–NH_2@ZIF-8 (methanol-PVP) were observed. This was owing to the fact that the kinetic diameter of cyclohexene (5.5 Å) was larger than that of ZIF-8. Thereby, the cyclohexene molecules could not penetrate the conformal ZIF-8 crystalline shell or large ZIF-8 microcrystals. However, substantial cyclohexene hydrogenation activity was achieved for Pd–UiO–NH_2@ZIF-8 (fractured shell), which was mainly ascribed to the potential diffusion pathway through the ZIF-8 shell of cyclohexene molecules caused by the boundaries between adjacent ZIF-8 crystallites.[44]

Given that epoxides are extensively applied in the production of diverse chemical raw materials and intermediates in many organic reactions, olefin epoxidation is a vital reaction.[150] However, although many transition-metal catalysts have been developed for catalytic epoxidation reactions, it is difficult to separate the product from the catalyst.[151] Recently, Zhou's group explored the preparation of PCN-222@Zr-BPDC hybrids with mismatching lattices, followed by their application as size-selective catalysts for olefin epoxidation, where the high porosity of the MOFs remarkably boosted the selectivity toward shape and size. In the case of the core–shell PCN-222@Zr-BPDC hybrid, the Fe-porphyrin moieties on PCN-222 served as the active centers for the epoxidation reaction toward olefin, whereas the selectivity of the substrates was dependent on the tunable shell. Olefins with different molecular sizes were transformed into the corresponding epoxides, showing different conversion ratios, where the small olefins demonstrated ideal conversions. The PCN-222@Zr-BPDC hybrid exhibited high accessibility and catalytic activity given that the size of the olefin was smaller than the pore size of Zr-BPDC (UiO-67), affording fast and efficient diffusion of the substrate. The catalytic results displayed that the olefin conversion decreased with an increase in the size of the olefins. Conversely, the decreasing trend of olefin conversion was not further observed for smaller olefins obtained under analogous preparation conditions. This revealed that olefins with large sizes were blocked by the shell, limiting the diffusion rates and hampering the accessibility of these molecules to the catalytic centers. Consequently, this catalytic system showed high size selectivity.[30] Similarly, Han's group proposed the core–shell PCN-222-Co@TpPa-1, which integrated the advantages of PCN-222-Co and TpPa-1. Due to the Lewis acid active sites present in PCN-222-Co, active Brønsted base sites in TpPa-1 (imine groups), and efficient interaction between the reactants and the PCN-222-Co@TpPa-1 hybrid, the PCN-222-Co@TpPa-1 heterostructure demonstrated an efficient bifunctional catalysis performance for the one-pot cascade deacetalization–Knoevenagel condensation reaction. Two sequential steps occurred in the catalytic reaction, including the reaction of benzaldehyde dimethylacetal to benzaldehyde by catalyzing with the unsaturated Zr(IV) and Co(II) centers and production of 2-benzylidenemalononitrile *via* the Knoevenagel condensation reaction by catalyzing with the imine groups in TpPa-1, giving a high yield of 99.3%.[71]

Considering that it is difficult to separate and recover the catalyst used for Knoevenagel condensation, consequently generating a large amount of waste,[152] it is vital to develop heterogeneous catalysts, which illustrate evident advantages such as less side reactions, feasible separation step, low corrosiveness and good reusability. Gong *et al.* reported a UiO-67–BPY@UiO-66 shell-structure. Combining the high stability of UiO-66 and active Lewis basic sites of the bipyridyl linker, the UiO-67–BPY@UiO-66 hybrid was then explored as a heterogeneous catalyst for catalyzing the Knoevenagel condensation. The outstanding catalytic efficiency was mainly attributed to the

homogeneous distribution of active sites (Lewis basic) present in the external layer of the UiO-67–BPY@UiO-66 heterostructure.[67]

Besides MOF-on-MOF hybrids, diverse MOF@COF hybrids have also been constructed for application in heterogeneous catalysis and organic catalysis. Cordova group's developed a 2D MOF-901, involving Ti-MOF modified with benzene-1,4-dialdehyde through imine condensation reactions. The incorporation of Ti(IV) units endowed MOF-901 with efficient photocatalysis ability by coating poly(methyl methacrylate) (polyMMA), which showed a high-number-average molar mass (26 850 g mol^{-1}).[116] Furthermore, Kim's group developed a Pd/TiATA@LZU1 composite as an excellent photocatalyst toward tandem dehydrogenation and hydrogenation reactions, where these reactions were carried out in a continuous-flow microreactor.[88] Further, Wu *et al.* presented a UiO-66@SNW-1 photocatalyst for tandem deacetalization–Knoevenagel condensation reaction. Owing to the fact that UiO-66@SNW-1 was comprised of Lewis acid sites (Zr clusters in UiO-66) and Brønsted base sites (amino groups in SNW-1), the UiO-66@SNW-1 catalyst exhibited remarkably higher catalysis ability than that of its UiO-66, SNW-1, and UiO-66–NH_2 parents. Moreover, Li's group prepared a core–shell MOF@COF composite with enhanced catalytic efficiency and fast transfer procedure. The prepared NH_2–MIL-101(Fe)@NTU-COF hybrid displayed good selectivity toward benzaldehyde, indicating that the catalytic selectivity was remarkably improved by the NTU-COF shell.[90] Zhu *et al.* constructed a UiO-66–NH_2@COP@Pd heterostructure as an efficient catalyst for reducing 4-nitrophenol (4-NP) to 4-aminophenol (4-AP). The results verified that BH_4^- and 4-NP were adsorbed on the surface of UiO-66–NH_2@COP@(2.34%)Pd *via* π–π stacking interaction. Afterward, the donor BH_4^- transferred electrons to the acceptor 4-NP, together with the reaction of BH_4^- with H_2O, affording $NaBO_2$ and H_2. Additionally, Pd nanoclusters prompted H_2 to dissociate into H–H bonds. Subsequently, the activated H atoms escaped from the Pd sites to catalyze 4-NP, further efficiently transferring to 4-AP and desorbing from the UiO-66–NH_2@COP@(2.34%)Pd surface.[84] As aforementioned, the NH_2–MIL-125(Ti) MOF has been explored as an efficient photocatalyst for degrading pollutants and photocatalytic hydrogen evolution.[154] It also has great promise for application as a molecule catalyst. Sun *et al.* proposed a core–shell NH_2–MIL-125(Ti)@DM-LZU1 heterostructure and loaded Pt NPs. The prepared Ti-MOFs@Pt@DM-LZU hybrid was used as a photocatalyst for site-selective hydrogenation reactions. Accordingly, the Pt NPs remarkably promoted the charge separation in Ti-MOFs to produce electron-rich Pt NPs, while the reactant and diffusion around the active Pt NPs were remarkably boosted owing to the high hydrophobicity and porosity of the COF shell.[85]

Owing to the fact that MOF-based heterogeneous catalysts are composed of organic and inorganic segments, multiple active sites can be integrated in MOF-on-MOF and MOF@COF heterostructures for synergistic and/or cascade organic catalysis and photocatalysis. However, aiming at the improvement of the catalytic activity and selectivity, the poor acid stability of these nanomaterials, which cannot withstand harsh conditions, have to be overcome. Moreover, given that COFs have superior catalytic activity to many MOFs, further work is needed to develop much more MOF@COF heterostructures and exploit them in the field of organic catalysis.

4.2 Gas sorption and separation

As reported, MOFs and COFs have been vastly explored as excellent adsorbents for gas adsorption and separation. In this part, the applications of MOF-on-MOF and MOF@COF heterostructures in the field of gas adsorption/separation are highlighted and discussed in detail.

4.2.1 Gas sorption or storage. Among the different energy sources, hydrogen has aroused great attention owing to its

Table 3 Some representative materials for gas sorption

Materials	S_{BET}[a] (m^2 g^{-1})	Adsorbate	Gas uptake (mmol g^{-1})	Uptake pressure (bar)	Uptake temp. (°C)	Ref.
MIL-101@UiO-66	2772	H_2	2.4 wt%	1	−196	18
MIL-101	1716		1.9 wt%			
UiO-66	1186		1.5 wt%			
IRMOF-2@MOF-5	610	H_2	1.9 wt%	25	−196	157
IRMOF-2	1700		2.78 wt%			
MOF-5	3340		5.02 wt%			
ZIF-8@ZIF-67	1402.15	H_2	2.03 wt%	1	−196	158
ZIF-8	1323.62		1.43 wt%			
ZIF-67	1392.30		1.53 wt%			
nHKUST-1⊂MOF-5	1470	CH_4	197 mg g^{-1}	80	25	66
nHKUST-1	—		169 mg g^{-1}			
MOF-5	—		126 mg g^{-1}			
UiO-66–NH_2@COF-TAPB-BTCA	1153	H_2O	0.39 g g^{-1}	0.9 P/P_0	—	17
UiO-66–NH_2	1151		0.43 g g^{-1}			
COF-TAPB-BTCA	319		0.20 g g^{-1}			

[a] BET specific surface area.

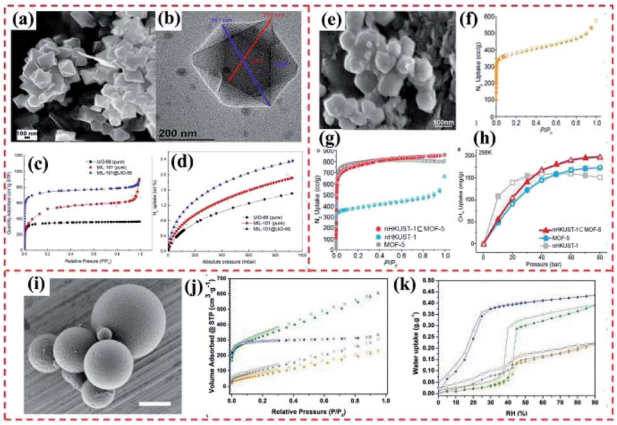

Fig. 22 (a) SEM and (b) TEM image of the core–shell nanocrystals. (c) N_2 sorption isotherms, and (d) H_2 sorption isotherms for the desolated MIL-101 (pure), UiO-66 (pure) and core–shell MIL-101@UiO-66 hybrid samples. Reproduced from ref. 18 with permission from Elsevier, Copyright 2014. (e) SEM image of nHKUST-1. (f) N_2 gas–adsorption isotherm of nHKUST-1. (g) N_2 gas adsorption isotherms of the MOF-5, nHKUST-1, and nHKUST1 ⊂ MOF-5 samples. (h) Gravimetric adsorption uptake capacity of nHKUST-1 ⊂ MOF-5, MOF-5, and nHKUST-1 for methane. Reproduced from ref. 66 with permission from the American Chemical Society, Copyright 2015. (i) FESEM images of UiO-66–NH_2@COF-TAPB-BTCA beads. (j) N_2 adsorption isotherms for UiO-66–NH_2 (blue), COFTAPB-BTCA beads (orange), physical mixture of these two components (grey), and UiO-66–NH_2@COF-TAPB-BTCA beads (green). (k) Water adsorption isotherms for UiO-66–NH_2 (blue), COF-TAPBBTCA beads (orange), physical mixture of these two components (grey), and UiO-66–NH_2@COF-TAPB-BTCA (green). Reproduced from ref. 17 with permission from Wiley, Copyright 2019.

substantial advantages such as non-toxicity, abundance, and easy preparation.[155] However, there are still some challenges in the large-scale production of H_2. Diverse adsorbent materials, such as porous materials, are used for the adsorption H_2, where among them, MOFs and COFs are superior candidates for adsorbing H_2.[156] Therefore, it is expected that diverse MOF-on-MOF and MOF@COF hybrids will be developed as promising H_2 storage nanomaterials (Table 3).

Ren *et al.* developed the MIL-101(Cr)@UiO-66(Zr) heterostructure as an efficient H_2 adsorbent (Fig. 22a and b). Basic characterizations verified that the MIL-101@UiO-66 sample displayed an enhanced surface area and large pore volume, indicating the introduction of UiO-66 in the MIL-101 framework (Fig. 22c). The enhanced hydrogen uptake capacity of MIL-101@UiO-66 was higher than that of MIL-101 by 26% and that of UiO-66 by 60% (Fig. 22d).[18] Additionally, the Janus IRMOF-2@MOF-5 heterostructure was proposed and developed as a hydrogen adsorbent. The hydrogen-storage capacity of the Janus particles was similar to that of a physical mixture of the two components. Janus particles seem to maintain their interconnected pore structures, making them good candidates for gas separation.[157] Moreover, two types of ZIF-8@ZIF-67 and ZIF-67@ZIF-8 heterostructures were prepared. The H_2 storage ability of the two core–shell ZIFs was superior to that of Co/Zn-ZIF and a physical mixture of ZIF-8 and ZIF-67 owing to their unique structures and element diversity.[158] The "nHKUST-1 ⊂ MOF-5" heterostructure was developed for adsorbing fuel molecules (Fig. 22e). Differing from the pure MOF-5 or nHKUST-1 framework, the gravimetric uptake capacity of nHKUST-1 ⊂ MOF-5 for CH_4 illustrated high volumetric fuel storage capacity and reversible CH_4 uptake efficiency (Fig. 22f–h).[66]

Besides the exploration of adsorbents based on MOF-on-MOF nanohybrids, the MOF@COF heterostructure also demonstrates a synergistic enhancement in gas adsorption. Maspoch's group presented the UiO-66–NH_2@COF-TAPB-BTCA nanohybrid (Fig. 22i). Because of its large surface area, UiO-66–NH_2@COF-TAPB BTCA displayed higher adsorption ability for water at the same P/P_0 than that of the pristine COF pores, displaying enhanced water uptake. The N_2 and H_2O adsorption isotherms of the UiO-66–NH_2@COF-TAPB-BTCA cores both exhibited around 3-fold higher S_{BET} and 2-fold higher q_{max} values due to the additional pores at the MOF/COF interface (Fig. 22j and k).[17] Further, Wang *et al.* proposed an a novel COF-MOF co-assembly strategy by combining $[M_3(OH)_{1-x}(O)_x(\text{-COO})_6]$MOF-type and $[B_3O_3(py)_3]$COF-type trimers. At 1 bar and 273 K, the CO_2 uptake capacity was 3.96 to 6.32 mmol g^{-1} in tpb-pacs. The C_2H_2 uptake of the COF-MOF was enhanced from 5.61 to 10.45 mmol g^{-1}, which was ascribed to tpb. This investigation demonstrated the introduction of C_3-symmetric fragments present in COFs in COF–MOF structures.[159] However, in comparison with the conventional MOF and COF materials, the limited types of MOF@MOF and MOF@COF hybrids restrict their applications in gas adsorption.

4.2.2 Gas separation. Owing to the fact that high adsorption selectivity and the removal of CO_2 from CH_4, N_2, and H_2 play an important role in the purification of natural gas and biogas, it is significant to develop advanced methods for the efficient separation of CO_2.[160] The membrane separation approach has been used extensively owing to its merits, such as low cost, energy efficiency, feasible operation, and reliability.[161] However, although considerable efforts have been devoted to the development of MOFs and COFs for membrane-based gas separation, the advancement of heterostructured nanohybrids based on MOFs and COFs has only recently attracted attention from researchers (Table 4). Qiu's group constructed a series of MOF@COF composites and developed them as separation membranes for H_2/CO_2 gas mixtures, which was ascribed to the chemical bonds produced between the MOF and COF of the membrane. Furthermore, due to the formation of an amorphous MOF in MOF@COF and the hermetically sealed space between the COF crystals, the obtained [COF-300]-[ZIF-8] had a high membrane selectivity toward H_2/CO_2 gas mixtures. This finding hinted the synergistic effect between the different molecular sieve materials, which endowed the COF-MOF a substantially enhanced performance as a membrane.[93] Recently, Webley's group developed a polymorphous core–shell MOF-S@MOF-C (Fig. 23a and b), which exhibited high adsorptive selectivity/capacity for CO_2 and N_2 simultaneously. The core–shell MOF-S@MOF-C hybrid with combined features showed superior gas separation ability. The 4-day exchanged MOF-S@MOF-C composite had a CO_2 adsorption capacity that was higher than that of the pure MOF-S, and higher CO_2/N_2 selectivity than that of the pristine MOF-C (Fig. 23c and d).[162]

Table 4 Some representative materials for gas separation

Materials	Pore size (nm)	S_{BET}[a] ($m^2\ g^{-1}$)	Gas separation	Capacity ($mmol^{-1}$ g, 1 bar)	Selectivity	Ref.
MOF@COF composite	COF: 2.0 ZIF-8: 1.18	COF: 2286.6 ZIF-8: 1869.5	H_2/CO_2	13.5	6.0 9.1	93
MOF-S@MOF-C	—	187.74	CO_2/N_2	2.3	32.7	162
PSF-ZIF@MOF	0.6/0.4	—	CO_2/N_2	2.33	39	58
MOF@COF-based MMMs	—	723	CO_2/CH_4	93	46.7	78
COF-LZU1-ACOF-1	0.3–0.5	386	H_2/CH_4	—	15	96
TpEBr@TpPa-SO_3Na iCON	0.4	—	H_2/CO_2	—	26	97
FeNi-M′ MOF	0.4	383	C_2H_2/CO_2	4.29	24	163

[a] BET specific surface area.

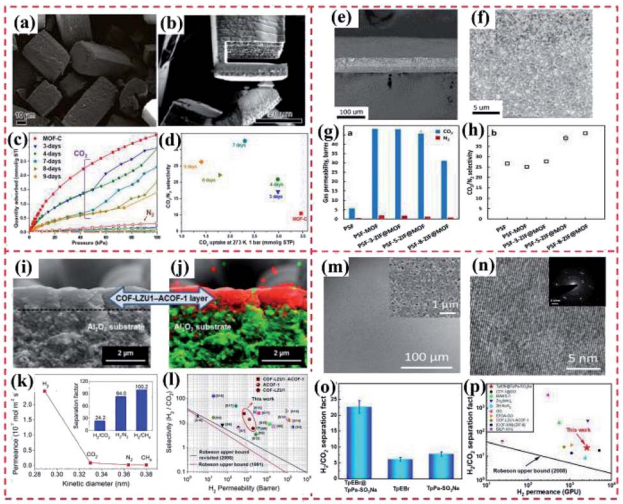

Fig. 23 SEM image of core–shell MOF-S@MOF-C composite after (a) 4-day and (b) 6-day exchange reaction. (c) CO_2 and N_2 adsorption/desorption isotherms and (d) CO_2/N_2 selectivity and CO_2 uptake (273 K, 1 bar) for MOF-S@MOF-C with 0-(MOF-C), 3-, 4-, 7-, 8- and 9-day (MOF-S) exchange. Reproduced from ref. 162 with permission from the American Chemical Society, Copyright 2019. Cross-section SEM images of PSF-5-ZIF@MOF membranes at (e) low magnification and (f) high magnification. Effect of LBL ZIF coating cycles on (g) pure gas permeability and (h) ideal gas selectivity of hybrid PSF membranes. Reproduced from ref. 58 with permission from the American Chemical Society, Copyright 2017. (i) Cross-sectional views of the supported COF-LZU1-ACOF-1 bilayer membrane. (j) EDXS mapping of the membrane cross-section and corresponding elemental distributions. (k) Single-gas performances of the COF-LZU1-ACOF-1 bilayer membrane as a function of the kinetic diameter of the permeating molecules. Mixed gas selectivity of (l) H_2/CO_2 as a function of H_2 permeability for our two pure COF membranes and the COF–COF bilayer membrane compared with literature data. Reproduced from ref. 96 with permission from the American Chemical Society, Copyright 2018. (m) Low-magnification SEM image of TpPa-SO_3Na nanosheets on α-Al_2O_3 support. (n) HRTEM image of TpPa-SO_3Na nanosheets. (o) H_2/CO_2 separation factor of these membranes in separating an equal molar mixture of H_2/CO_2 gas. (p) Comparison of H_2/CO_2 separation performance with other membranes. Reproduced from ref. 97 with permission from the American Chemical Society, Copyright 2020.

Song *et al.* reported a core–shell PSF-ZIF@MOF (PSF: polysulfone) crystalline structure and developed it as a separation membrane for CO_2/N_2 gas mixtures (Fig. 23e and f). In comparison with conventional fillers, the developed ZIF-8@UiO-66–NH_2 demonstrated some intrinsic advantages originating from each component. The large pores of the UiO-66–NH_2 MOF greatly improved molecular transport through the membrane. Further, the small pores or even smaller pores of the thin ZIF-8 shells also enhanced the molecular sieving, thus distinguishing N_2 molecules from smaller CO_2 molecules. The integrated ZIF-8@UiO-66–NH_2 hybrid membrane (40 wt% loading) exhibited enhanced hydrophobicity and substantial CO_2 separation capacity through both improved CO_2 permeability and CO_2/N_2 selectivity (Fig. 23g and h).[58]

Considering the outstanding separation performance toward mixed gases by MOFs and COFs, combined frameworks based on MOF@COF and COF@COF have also been explored as separation membranes toward gas mixtures. For instance, Chen *et al.* reported UiO-66–NH_2@TpPa-1 hybrids by combining the size selectivity of MOF fillers with the high stability of COF, which were explored as fillers in mixed matrix membranes (MMMs) for separating mixtures of CO_2/CH_4. Especially, the large pores of TpPa-1 COF efficiently prevented the blockage of the MOF pores, thus improving the gas permeation. Because of the high binding interaction between the coated COF layers and PSF, the developed UiO-66–NH_2@TpPa-1-based MMM acted as a polymer and filler. Significantly, the synergism caused by the size selectivity of the MOF pores and rigid modification of the polymer chains permitted the excellent permeation of CO_2 over CH_4 through the obtained MMMs.[78] Moreover, Fan *et al.* developed a COF-LZU1-ACOF-1 membrane with a suitable size range for gas molecules (Fig. 23i and j). Its separation selectivity toward gas mixtures of H_2/CO_2, H_2/N_2, and H_2/CH_4 outperformed that of the COF-LZU1 and ACOF-1 membranes because of its interlaced pore networks (Fig. 23k and l). Notably, the prepared membrane not only showed high permeability and selectivity but also surpassed the latest Robeson upper bounds. Its high permeability was ascribed to its thin COF-to-COF layer with a thickness of about 1 μm.[96] Ying *et al.* proposed a TpEBr@TpPa-SO_3Na iCON hybrid and employed it for the gas separation of an H_2/CO_2 mixture (Fig. 23m and n). The

TpEBr@TpPa-SO_3Na iCON hybrid demonstrated superior separation capacity, showing a high separation factor of 22.6, higher than that of the TpEBr nanosheet membrane and $TpPaSO_3Na$ membrane (Fig. 23o). Notably, the TpEBr@$TpPaSO_3Na$ iCON membrane had a good separation performance with H_2 and an H_2/CO_2 separation factor of 22.6 (Fig. 23p). This high separation factor of the TpEBr@TpPa-SO_3Na iCON was mainly ascribed to the reduced pore size caused by the staggered stacking of iCONs and the compact dense membrane structures.[97]

Although the extensive applications of MOFs and COFs have been investigated in the field of gas separation, their disadvantages such as high cost and poor stability in some organic solvents hinder their extensive industrial applications. Thus, rapid development and many efforts should focused on the construction of diverse MO-on-MOF, MOF@COF and COF-to-COF hybrids, which meet some requirements such as low cost, high aqueous and chemical stability, and high separation efficiency.

4.3 Biosensing and biomedical fields

Compared to traditional nanomaterials applied in the fields of biosensors and biomedicine, nano-sized MOFs exhibit the superior biological activity, high chemical and colloidal stability, efficient surface modification, and improved biological distribution. However, most MOFs and COFs suffer from a lack of multi-functional performance and unsatisfactory stability in various environments such as acidic and alkaline media or the physiological environment. Chemical stability and biocompatibility are crucial for the sensing performances and effective treatment. The stability of MOFs is governed by multiple factors, including their ligand structure, the oxidation state and the ionic radius of their metal ions, metal–ligand coordination geometry, and hydrophobicity of their pore surface. Among them, the metal–ligand bond strength is critical to obtain labile coordination bonds, further controlling the stability of MOFs in different sensing systems. Theoretically, the stability of the metal–ligand bond can be simply predicted using the hard/soft acid/base (HSAB) principle. Another concern in the biosensing and biomedical fields is biocompatibility, and therefore metal ions and ligands or monomers with low toxicity should be adopted for the synthesis of MOF/COF hybrids. To achieve the desired functions such as light harvesting, monomers with specific structures such as phthalocyanines and porphyrin are required. Diverse MOFs or COFs have been explored as platforms for biosensors or as drug delivery systems and nanocatalytic drugs. Thus, to extend the application range of these porous materials, some MOF@COF conjugations were prepared and have demonstrated promise in the biomedical field.

4.3.1 Biosensing strategies. As aforementioned, MOFs possess some advantages of adjustable structures, large surface area and porosity, abundant exposed active sites, and excellent biocompatibility. Moreover, due to the presence of functional groups of $-NH_2$ or –COOH on MOFs, MOFs have been used as great potential platforms with boosted immobilization ability toward antibiotics and biomolecules such as glucose, antibodies and aptamers.[164] Similarly, COFs demonstrate the advantages of unique structural properties, high specific area, and chemical and physical stability, which are comprised of strong covalent bonds and show superior biosensing performances toward different targets, together with extensive applications in the biomedical field.[165,166] Recently, many biosensors based on diverse MOFs (Zr-MOF, Al-MOF, Fe-MOF, Zn-MOF, *etc.*)[167] and COFs[168] have been developed for detecting diverse targets, such as small biomolecules (H_2O_2, dopamine, and ascorbic acid (AA)),[169] antibiotics,[170] biomarkers,[171] heavy metal ions,[172] proteins,[173] and living cancer cells,[174] *via* different determination techniques, including electrochemical methods,[175,176] fluorescence approaches,[170,177,178] electrochemiluminescence,[175] surface plasmon resonance,[179]

Table 5 Summary of the reported MOF/COF nanohybrid-based sensing applications[a]

Material	Target	Detection method	Linear range	LOD	Ref.
UiO-67@Ni-MOF	Glucose	Amperometric	5–3.9 mM	0.98 mM	189
Zn-MOF-on-Zr-MOF	PTK7	EIS	1×10^{-3} to 1 ng mL^{-1}	0.84 pg mL^{-1}	45
Tb-MOF-on-Fe-MOF	CA125	EIS	0.1–200 U mL^{-1}	58 μU mL^{-1}	46
	MCF-7 cells		1×10^2 to 1×10^5 cell per mL	19 cell per mL	
AgNCs/Apt@CuFe@FeFe	BLM	EIS	1×10^{-5} to 0.1 pg mL^{-1}	0.0082 fg mL^{-1}	192
Ce-MOF@COF	OTC	EIS	1×10^{-4} to 0.5 ng mL^{-1}	17.4 fg mL^{-1}	95
Co-MOF@TPN-COF	AMP	EIS	1×10^{-5} to 2 ng mL^{-1}	0.217 fg mL^{-1}	94
UiO@COF	ATP	Ratiometric fluorescence	0–10 μM	0.067 μM	80
	$PO4^{3-}$		0–30 μM	0.038 μM	
Cr-MOF@CoPc	CT26 cells	EIS	50–1×10^7 cells per mL	36 cells per mL	193
		DPV		8 cells per mL	
CDs@ZrHf-MOF	HER2	EIS	1×10^{-3} – 10 ng mL^{-1}	19 fg mL^{-1}	174
	MCF-7 cells		1×10^2–1×10^5 cell per mL	23 cells per mL	
Pd NPs/CMC–COF–LZU1	HeLa cells	Colorimetric	1×10^2–1×10^6 cell per mL	100 cells per mL	194

[a] PTK7: protein tyrosine kinase 7; EIS: electrochemical impedance spectroscopy; CA125: carbohydrate antigen 125; MCF-7 cells: human breast adenocarcinoma cell; BLM: bleomycin; OTC: oxytetracycline; AMP: ampicillin; ATP: adenosine triphosphate; CT26 cells: colorectal cancer cells; DPV: differential pulse voltammetry; SWV: square wave voltammetry; HER2: human epidermal growth factor receptor 2; miRNA-21: microRNA 21; and PSA: prostate specific antigen.

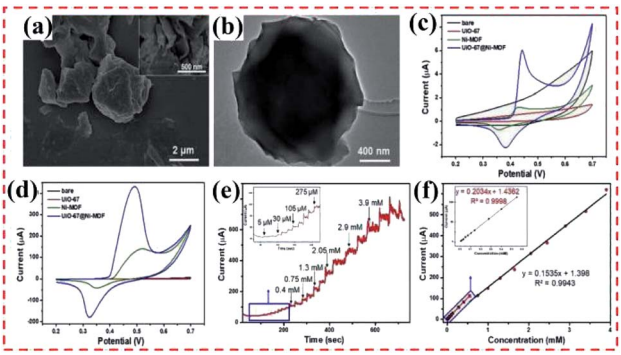

Fig. 24 (a) SEM image and (b) TEM image of prepared UiO-67@Ni-MOF. CV curves of bare GCE, UiO-67/GCE, Ni-MOF/GCE, and UiO-67@Ni-MOF/GCE in 0.1 M NaOH in the (c) absence and (d) presence of glucose. (e) Amperometric *i–t* curves of UiO-67@Ni-MOF/GCE with the successive injection of glucose in 0.1 M NaOH at 0.55 V by stirring. (f) Calibration plot of current *versus* glucose concentrations for UiO-67@Ni-MOF/GCE, corresponding to (e). Reproduced from ref. 189 with permission from Elsevier, Copyright 2020.

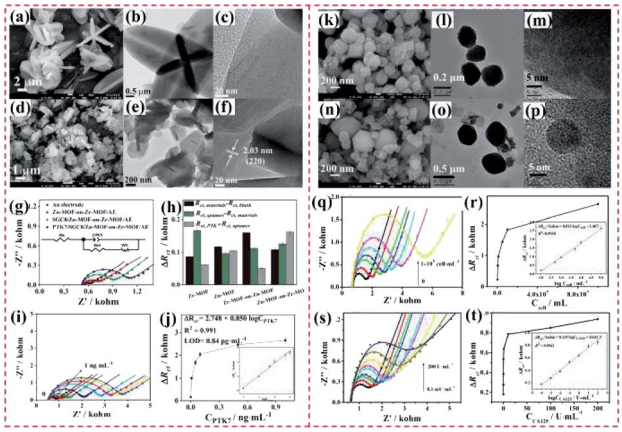

Fig. 25 (a) SEM, (b) TEM and (c) HR-TEM images of Zn-MOF-on-Zr-MOF. (d) SEM, (e) TEM and (f) HR-TEM images of Zr-MOF-on-Zn-MOF hybrids. (g) EIS Nyquist plots of Zn-MOF-on-Zr-MOF-modified Au electrode for the detection of 0.001 ng mL^{-1} PTK7. (h) Variation in the charge-transfer resistance (R_{ct}) values for each stage in the detection of PTK7. (i) EIS responses of Zn-MOF-on-Zr-MOF/AE with different PTK7 concentrations. (j) Dependence of ΔR_{ct} on the concentration of PTK7 (inset: the linear parts of the calibration curves). Reproduced from ref. 45 with permission from Elsevier, Copyright 2019. SEM, TEM and HR-TEM images of (k, l, and m) Fe-MOF-on-Tb-MOF and (n, o, and p) Tb-MOF-on-Fe-MOF, respectively. (q) EIS Nyquist plots for the detection of CA125 at different concentrations using Tb-MOF-on-Fe-MOF-based aptasensor. (r) Calibration curves between ΔR_{ct} and CA125 concentrations (inset: the linear fit plot of ΔR_{ct} as a function of the logarithm of CA125 concentration). (s) EIS responses of Tb-MOF-on-Fe-MOF-based aptasensor at different MCF-7 cell concentrations. (t) Dependence of ΔR_{ct} on the concentration of MCF-7 cells (inset: the linear parts of calibration curves). Reproduced from ref. 46 with permission from Elsevier, Copyright 2019.

colorimetric method,[180] microfluidic impedance[181] and chemiluminescence.[182] Among them, the electrochemical method is an efficient technique for the detection of biomolecules in the biological field. In the case of most individual components of MOFs and COFs, some shortcomings such as poor electrochemical activity, low stability, and narrow linear concentration range of targets greatly restrict their application as electrochemical biosensors. Thus, other components such as inorganic NPs,[183] conducting polymers,[184] quantum dots,[185] carbon nanomaterials,[186] biomolecules,[187] and other types of MOFs[188] have been combined with MOFs and COFs to overcome their disadvantages. By integrating one MOF within or on another MOF or COF layer, chemical, physical, and structural advantages of MOF-on-MOF or MOF@COF nanohybrids can be obtained, together with some unexpected synergistic effects (Table 5). Based on the electrocatalytic ability of Ni-MOF, Lu *et al.* fabricated the UiO-67@Ni-MOF composite and used it for the detection of glucose (Fig. 24a and b). Accordingly, the large specific area and highly electrocatalytic ability of UiO-67 greatly improved the electron transfer in UiO-67@Ni-MOF, while Ni-MOF showed high electrochemical catalytic ability for glucose (Fig. 24c and d). Thus, the constructed electrochemical biosensor displayed a fast response, wide detection range, and low LOD (Fig. 24e and f).[189]

Considering the immobilization interaction between aptamer strands and MOF or COF networks such as π–π stacking, van der Waals force, hydrogen bonds, and possible coordination networks,[190] MOFs or COFs can be employed as a sensitive layer for the development of biosensors. These biosensors can be further used to detect the corresponding targets of the aptamers or antibodies (biomarkers, antibiotics, or heavy metal ions).[174] By integrating the advantages of diverse MOFs and COFs, MOF-on-MOF and MOF@COF heterostructures can lead to superior sensing performances compared to their individual components. In our previous work, we developed two novel types of scaffolds for binding the PTK7-targeted aptamer (PTK7: protein tyrosine kinase 7), followed by the detection of PTK7. The Zr-MOF component remarkably enhanced the anchoring of the aptamer, while the Zn-MOF part greatly stabilized the formed G-quadruplex of the ZnZr-based MOFs (Fig. 25a–f) developed between the aptamer strands and PTK7 because of the specific recognition (Fig. 25g and h). Compared with the Zr-MOF-on-Zn-MOF-based aptasensor, the Zn-MOF-on-Zr-MOF-based aptasensor had higher sensing ability, an ultralow detection limit of 0.84 pg mL^{-1} within a wide linear PTK7 concentration (Fig. 25i and j) and comprehensive excellent sensing performances. Moreover, Tb-MOF exhibited remarkable fluorescence, while both Fe-MOF and Tb-MOF displayed outstanding detection performances, excellent electrochemical activity, and good biocompatibility.[45] Hence, our group synthesized two types of heterostructured bimetallic TbFe-MOF, *i.e.*, Tb-MOF-on-Fe-MOF and Fe-MOF-on-Tb-MOF (Fig. 25k–p). After the CA125-targeted aptamer (CA125: carbohydrate antigen 125) was anchored, the obtained bimetallic MOF-based aptasensor was effectively used to sensitively determine CA125 and cancer cells. The Tb-MOF-on-Fe-MOF-based biosensor displayed higher stabilization ability toward the formed G-quadruplex than that of the Fe-MOF-on-Tb MOF-based biosensor because of the strong immobilization of aptamer over the Tb-MOF-on-Fe-MOF substrate. Hence, the fabricated biosensor showed a very low LOD for analyzing

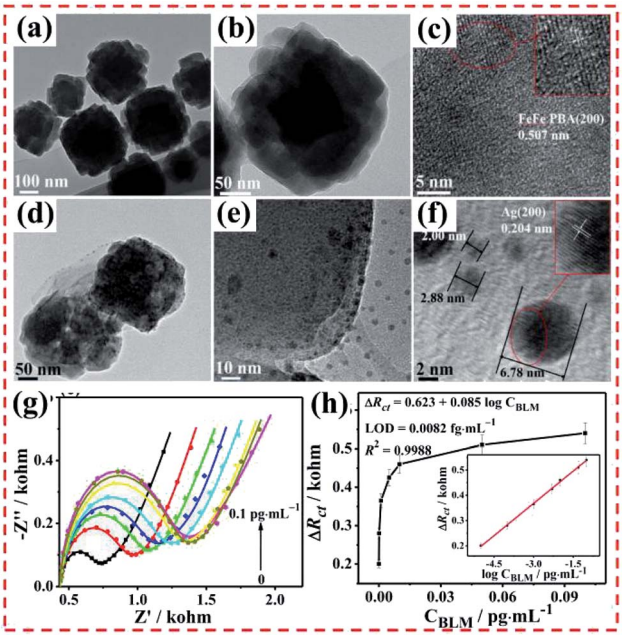

Fig. 26 TEM and HR-TEM images of (a–c) CuFe@FeFe and (d–f) AgNCs/Apt@CuFe@FeFe PBAs. (g) EIS responses of the AgNCs/Apt@CuFe@FeFe/AE with different BLM concentrations. (h) Dependence of ΔR_{ct} on the concentration of BLM based on AgNCs/Apt@CuFe@FeFe/AE (inset: linear part of the calibration curve). Reproduced from ref. 192 with permission from the American Chemical Society, Copyright 2018.

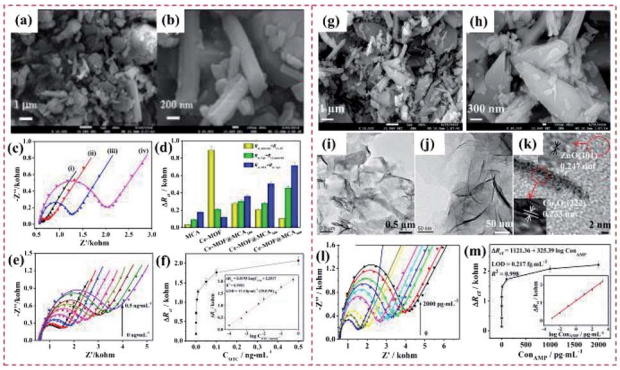

Fig. 27 (a) and (b) SEM images of Ce-MOF@MCA_{500} nanohybrids. (c) EIS Nyquist plots of the OTC detection procedures using the electrochemical aptasensors based on Ce-MOF@MCA_{500} in 5 mM $[Fe(CN)_6]^{3-/4-}$ containing 0.1 M KCl. (d) Corresponding variations in the R_{ct} values of the five types of aptasensors for detecting OTC. (e) EIS Nyquist plots for the detection of different concentrations of OTC using the Ce-MOF@MCA_{500}-based aptasensor. (f) Corresponding calibration curves between ΔR_{ct} and OTC concentrations (inset: the linear fit plot of ΔR_{ct} as a function of the logarithm of OTC concentration). Reproduced from ref. 95 with permission from Elsevier, Copyright 2019. (g) and (h) Low- and high-magnification FE-SEM images of Co-MOF@TPN-COF. (i, j, and k) TEM and HR-TEM images of Co-MOF@TPN-COF. (l) EIS responses of the Co-MOF@TPN–COF–based aptasensor with different AMP concentrations. (m) Dependence of ΔR_{ct} on the concentration of AMP. The linear parts of the calibration curves are shown in the inset of (l). Reproduced from ref. 94 with permission from Elsevier, Copyright 2019.

CA125 and cancer cells (Fig. 25q–t) owing to its superior biocompatibility and good endocytosis.[46]

Diverse aptamers have been applied to construct various aptasensors that sensitively and selectively determine antibiotics in the aqueous environment owing to the high bioaffinity between aptamers and antibiotics.[191] Thus, by anchoring aptamers on MOFs and COFs, different types of biosensors based on these porous frameworks have been developed and used to detect antibiotics.[94] In our previous work, core–shell heterostructured PBA nanospheres embedded in Ag NCs (Fig. 26a–f) were prepared and employed as a sensitive layer to immobilize bleomycin (BLM)-targeted aptamer, following by the detection of BLM. Ag nanoclusters were prepared using an aptamer that can specifically bond with BLM as the template to enhance the sensing performance and accelerate the sensing response. For this aptasensor, combining Fe(II) ions of CuFe@FeFe PBA and BLM led to the irreversible cleavage of the aptamer strands and changes in its electrochemical response. The electrochemical results showed that the developed aptasensor had a low LOD value (Fig. 26g and h), which is lower than that for other aptasensors for the detection of antibiotics.[192]

Significant work has been done on combining COFs and MOFs because MOF@COF hybrids possess the merits of each component. Our group developed a series of Ce-MOF and COF nanohybrids and exploited them as novel platforms for an oxytetracycline (OTC) aptasensor (Fig. 27a and b). Integrating the excellent sensing properties of Ce-MOF and good electrochemical activity of MCA, the Ce-MOF@MCA-based biosensor exhibited a very low LOD for detecting OTC and other good sensing ability in aqueous solution (Fig. 27c–f).[95] Recently, our group prepared a Co-MOF@TPN-COF nanoarchitecture and used it as s platform after immobilizing the AMP-targeted aptamer (AMP: ampicillin) (Fig. 27g–k). Given that a large number of aptamer molecules were anchored on the Co-MOF@TPN-COF nanosheets *via* complex interaction, the developed Co-MOF@TPN–COF–based biosensor showed a low LOD of 0.217 fg mL^{-1} (Fig. 27l and m).[94] The Ce-MOF@MCA and Co-MOF@TPN-COF heterostructures exhibited common features, as follows: (i) abundant nitrogen-functional groups in the COF component, which can greatly facilitate the adsorption of the aptamer stands; (ii) the conjugation of the COF and the electrochemically active Ce-MOF or Co-MOF can outstandingly amplify the electrochemical signal; and (iii) the porous nanostructures and large cavities in the heterostructures can allow the aptamer to adsorb over the heterostructure and permeate its interior, thus boosting the sensing ability and enhancing the G-quadruplex stability. Although great efforts have been dedicated to exploring new porous MOF@COF hybrids and to developing their applications in diverse fields, these materials are still in the early stage of advancement in the biosensing field.

In addition to their application as electrochemical biosensors, MOF-on-MOF and MOF@COF heterostructures have been used as fluorescence biosensors because of their remarkable fluorescence performances. Wang *et al.* proposed an MOF@COF to remove aggregation-caused quenching and to enhance the emission intensity of COFs (Fig. 28a and b). The abundant

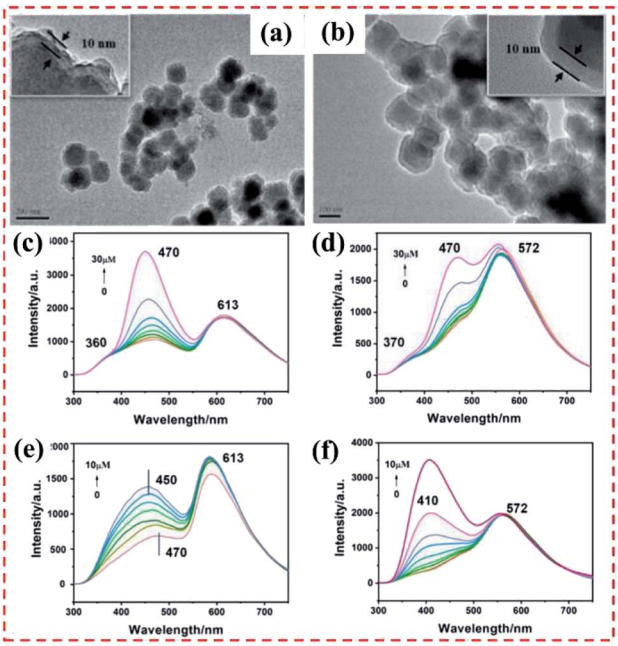

Fig. 28 TEM images of (a) UiO@COF1 and (b) UiO@COF2. Fluorescence spectra (λ_{ex} = 270 nm) of 0.1 mg mL^{-1} (c) UiO@COF1 and (d) UiO@COF2 upon the addition of PO_4^{3-} in the concentration range of 0–30 μM. Fluorescence spectra (λ_{ex} = 270 nm) of 0.1 mg mL^{-1} (e) UiO@COF-1 and (f) UiO@COF-2 upon the addition of ATP in the concentration range of 0–10 μM. Reproduced from ref. 80 with permission from the American Chemical Society, Copyright 2020.

Zr^{4+} ions present in UiO-66 led to high binding affinity with the phosphate group to enhance the sensing selectivity, while the organic linker, BDC-NH_2, which made the UiO-66 surface rich in amino groups, bound with the COF shell by covalent bonds. The multi-emission of the UiO@COF hybrids exhibited remarkable ratiometric sensing abilities toward PO_4^{3-} and ATP, showing an LOD of 0.067 μM for PO_4^{3-} and 0.038 μM for ATP, much lower than that of other types of sensors (Fig. 28c–f).[80] According to the above discussion, the development of biosensors based on MOF-on-MOF and MOF@COF heterostructures is still in its early phase. The fabrication of sensitive, feasible, and wearable electrochemical biosensors using these porous organic frameworks as electrode materials remains undeveloped, and therefore needs further investigation in the biosensing field.

4.3.2 Cancer therapy and wound healing. Cancer has become a major global problem with extremely high mortality.[195] MOFs and COFs have recently attracted attention in cancer therapy because of their unique advantages, including regular pore structure, high specific surface area/porosity, low density, adjustable pore size, easy surface modification, and chemical structure design (Table 6).[196] The exquisitely designed nanoMOFs and COFs with small sizes (approximately 200–300 nm) exhibit good biocompatibility and biodegradability, thus showing potential applications in cancer therapy.[197] Different types of MOFs containing metal ions or organic ligands with catalytic performances, such as Cu-MOF,[198,199] NH_2–MIL-88B (Fe),[200,201] Mn-MOF,[202,203] UiO-66/Zr-MOF,[204–207] and porphyrinic-based MOFs,[208–210] have been explored not only as anticancer drug carriers but also as catalysts for chemodynamic therapy (CDT) and photodynamic therapy (PDT). COFs have unique advantages, such as high crystallinity, inherent pores, and large specific surface areas, which remarkably improve their loading ability toward different cancer drugs such as ibuprofen,[211] DOX,[212] 5-fluorouracil,[213] captopril,[214] and curcumin,[215–217] as well as near infrared (NIR) dyes.[218] Most importantly, structure and function modularity can be realized by logically selecting functional monomers, which endow COFs with different functionality, such as photosensitizers for PDT and photothermal therapy (PTT).[219,220] Therefore, COFs have been explored as multifunctional cancer therapeutic reagents for tumor hypoxia relief and PDT,[221,222] chemo-PTT,[223] and PT/PDT[224] owing to their good aqueous dispersion, excellent biodegradability, strong light conversion, and efficient reactive oxygen species (ROS) generation ability.[225]

ZIF-8 is often used as a promising drug carrier owing to its nontoxicity and remarkable biocompatibility.[226] This MOF displays high pH-responsiveness as a drug-loading carrier in the acidic tumor microenvironment (pH 5.7–7.8) and high stability under normal physiological conditions. Therefore, combining PB and ZIF-8 can form a core–shell dual MOF with potential application as a drug delivery system with dual-mode-responsive abilities. Wang *et al.* reported a PB/ZIF-8 hybrid using PB as the core (Fig. 29a–c), which showed excellent chemo-PTT cancer therapy performances under NIR light. The ZIF-8 shell was then degraded and removed from the PB core. The inner PB particles were then irradiated by NIR light, generating heat to kill cancer cells. The results revealed its higher efficacy toward HeLa cancer cell lines than that of the single therapy mode (Fig. 29d). Thus, the obtained PB/ZIF-8 hybrid therapy system attained synergistic chemo-PTT therapy efficacy (Fig. 29e and f). The anti-tumor efficiency of CSD-MOFs@DOX + NIR was much higher than that of single mode

Table 6 Summary of the reported MOF/COF nanohybrids based cancer therapy and wound healing applications

Materials	Targeted sites	Application	Ref.
PB@ZIF-8	HeLa tumor	Dual-mode MRI, fluorescence imaging, photothermal therapy	62
CS-MOFs@AS	HeLa tumor	pH-responsive chemotherapy, multimodality imaging	227
H_2P-MOF@UiO-AM	HeLa cells	Photodynamic therapy	77
Hf-UiO-AM@HUC-PEG	HeLa tumor	Photodynamic and photothermal therapy, computed tomography/photothermal imaging	82
MIL-88B-on-UIO-66	MCF-7 cells	Drug delivery	52
$NMC_{TP\text{-}TTA}$	Infected wound	Catalytic microbicidal efficacy and wound healing	91

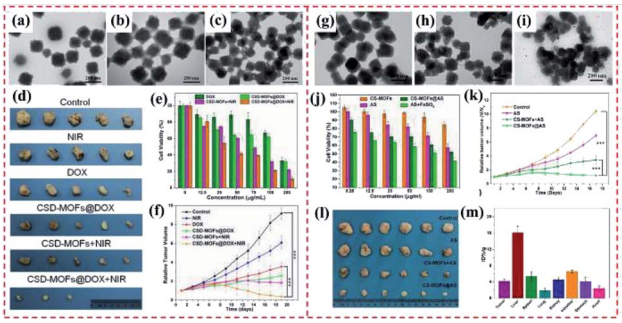

Fig. 29 (a–c) TEM images of DOX@CSD-MOFs after drug release at pH = 7.4, 6.2 and 5.0, respectively. Error bars are based on triplicate measurements. (d) Photographs of tumors harvested from mice receiving different therapeutic treatments. (e) Relative viability of HeLa cells incubated with free DOX, CSD-MOFs@DOX, CSD-MOFs and CSD-MOFs@DOX with or without laser irradiation (1.6 W cm^{-2}, 5 min). (f) Tumor growth curves of the corresponding group. Reproduced from ref. 62 with permission from Ivyspring International Publisher, Copyright 2017. (g–i) Corresponding TEM images of CSMOFs nanocubes in PBS solution with different pH values (pH 7.4 (panel (g))), pH 6.5 (panel (h)), and pH 5.0 (panel (i)) after the Fe(III) release process. (j) *In vitro* therapeutic efficacy. (k) Tumor growth curves of different groups of tumor-bearing mice after various treatments indicated every 2 days for 17 days. (l) Photographs of the tumors from different mice groups at day 17 after treatment and (m) biodistribution of CS-MOFs in HeLa-tumor-bearing mice at 24 h after IV injection. Reproduced from ref. 227 with permission from the American Chemical Society, Copyright 2017.

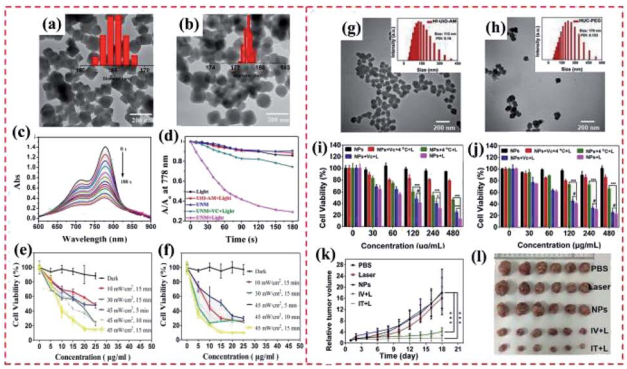

Fig. 30 TEM images and hydrodynamic size distribution (inset) of (a) UiO-AM and (b) UNM. (c) Time-dependent UV absorption spectra of ICG at 778 nm with UNM in PBS after irradiation with a 450 nm lamp from 0 to 180 s. (d) Comparison of the decay rate of ICG alone (black), UiO-AM (red), UNM in the dark (blue), and UNM upon irradiation with (green) or without (pink) the vitamin C scavenger, respectively. *In vitro* photocytotoxicity of MOF@COF nanocomposites at different laser intensities, irradiation times, and PS concentrations against (e) HepG2 cells and (f) HeLa cells. Reproduced from ref. 77 with permission from the American Chemical Society, Copyright 2017. TEM images and corresponding DLS profiles of (g) Hf-UiO-AM and (h) HUC-PEG. Cell viability of (i) HeLa cells and (j) HepG2 cells after incubation with HUC-PEG with or without 671 nm light illumination. (k) Relative tumor volume changes of mice treated with PBS, PBS + laser, only HUC-PEG, and HUC-PEG by intravenous and intratumoral injection + laser. (l) Representative tumor photographs. Reproduced from ref. 82 with permission from Elsevier, Copyright 2020.

therapy.[62] The core–shell $Mn_3[Co(CN)_6]_2$@MIL-100(Fe) (CS-MOFs) hybrid was prepared and utilized for the synchronous co-delivery of artesunate (AS) and ferric ions for cancer therapy. Owing to the fact that the $Mn_3[Co(CN)_6]_2$@MIL-100(Fe) hybrid had a mesoporous nanostructure and high binding interaction with organic linkers, it exhibited a high loading capacity toward artesunate (AS) of 531 mg g^{-1}. AS molecules were released from CS-MOFs at pH 5.0–6.5, but not released under physiological environment (pH ~ 7.4). The efficient release of AS was observed due to the decomposition of the outer MIL-100(Fe) shell, leading to the on-demand release of Fe(III) ions and AS in the tumor tissue (Fig. 29j–l). The intracellular Fe(III) ions were transferred to Fe(II), resulting in the catalysis of AS to produce carbon free radicals and ROS. In comparison with free AS alone, the CS-MOFs@AS system demonstrated remarkably improved tumor delivery specificity, which was 5.79-times higher than that of free AS (Fig. 29m).[227]

As discussed above, the surface morphologies and sizes of MOF/COF hybrids can be modulated using the template strategy and surfactant-assisted emulsion approach.[228] Zheng *et al.* reported a novel H_2P-MOF@UiO-AM hybrid, where the photoactive porphyrin-MOF (H_2P-MOF) was *in situ* grown on the outer UiO-AM–NH_2 surface. The formed hybrid had a nanosize, which was smaller than 200 nm, showing the ability to be internalized by cancer cells (Fig. 30a and b). $^1O_2$ species were generated by irradiating the H_2P-MOF@UiO-AM hybrid, thus showing potential application in PDT (Fig. 30c–f).[77] Zheng *et al.* obtained the Hf-UiO-AM@HUC-PEG hybrid (Fig. 30g and h), where its small particle size afforded improved uptake ability toward cancer cells. After endocytosis, the Hf-UiO-AM@HUC-PEG hybrid also produced cytotoxic $^1O_2$ for PDT *in vitro*. Nevertheless, the porphyrin displayed a short excitation wavelength and low molar extinction coefficient, remarkably inhibiting the *in vivo* application of this hybrid. Tetratopic chlorin-doped Hf-UiO-66 showed spatial arrangement-dependent photochemical behavior, and thus potential application in PDT and PTT (Fig. 30i and j). Owing to the features of the Hf element, the proposed Hf-UiO-AM@HUC-PEG hybrid demonstrated computed tomography/photothermal imaging functions (Fig. 30k and l).[82] In 2020, Zhang and co-workers proposed a novel MIL-88B-on-UiO-66 hybrid as a bifunctional drug delivery nanosystem. The *in vitro* anticancer effect of the prepared MIL-88B-on-UiO-66 was probed against MCF-7 breast cancer cells, and the results revealed its synergistic effect for 5-fluoracil (5-Fu) and alendronate (AL). This successful controlled drug release can provide a novel drug delivery nanosystem for combined cancer therapy.[52]

Owing to the fact that some MOFs with peroxidase features can generate ROS, which play an important role in the eradication of bacteria by catalyzing the conversion of H_2O_2 into the highly toxic hydroxyl radical ($^{\bullet}OH$), they show great potential as antibacterial agents. Qu' group reported a novel MOF@COF nanozyme as a high-efficiency peroxidase mimic, which exhibited enhanced bacterial inhibition.[91] For the synthesis of this MOF@COF nanozyme, the superficial $COF_{TP\text{-}TTA}$ was prepared on the surface of NH_2–MIL-88B(Fe) using weak acidic (phenol) and basic functional (triazine) groups as building

blocks. Due to its hierarchical nanocavities with tailored surface functional groups, $COF_{TP\text{-}TTA}$ served as enzyme binding pockets for the formation of a specific pore microenvironment around the active sites. The TEM image showed that a sparse and dendritic $COF_{TP\text{-}TTA}$ skin grew on the surface of NH_2–MIL-88B(Fe)–CHO. The NH_2–MIL-88B(Fe)@$COF_{TP\text{-}TTA}$ (denoted as $NMC_{TP\text{-}TTA}$) nanozyme efficiently captured bacteria tightly *via* multivalent topological interactions, eventually leading to the death of the bacteria by the generated ROS. Both the *in vitro* and *in vivo* studies revealed its satisfactory catalytic microbicidal efficacy, which enabled a wound to become red quickly, displaying a nature-inspired strategy that can remarkably facilitate the design and construction of versatile enzyme mimics. To date, only five samples of MOF-on-MOF and MOF@COF hybrids have been applied as delivery systems of anticancer drugs and photosensitizers for cancer therapy. Although rapid progress has been achieved in the application of MOFs/COFs in cancer therapy, the use of MOF-on-MOF and MOF@COF conjugations as nanocatalytic medicine is still in the early stage. Most studies have concentrated on the preparation approaches of nano-scale MOF-on-MOF for different therapeutic fields, and the degradation behavior and *in vivo* chronic toxicity of these MOF-based conjugations have been rarely reported.

5. Conclusions and future outlook

Great efforts have been devoted to exploring the types, formation mechanism of heterostructures, and basic characteristics of new MOFs and COFs and their applications. Synthesizing diverse MOF/COF-based heterostructures with specific morphologies and shapes, new features, and synergistic effects is essential for the further development of advanced materials. To ameliorate the inferior electrochemical activities of most MOFs and COFs, their lack of multi-functional performances, and unsatisfactory stability in various environments, such as acidic and alkaline media or the physiological environment, hybrids or composites have been developed using various techniques to improve their potential applications. The integration of MOFs or MOFs and COFs, such as MOF-on-MOF, MOF@COF, and COF-to-COF hybrids, has been achieved by synthesizing guest MOFs or COFs on preformed host MOFs or COFs to overcome the above-mentioned disadvantages. These strategies provide much more possibilities for the development of novel MOF hybrids or MOF/COF heterostructures with new structural diversities and enhanced properties. Compared with the individual MOFs or COFs, the MOF/COF heterostructures normally exhibit the following fantastic properties due to their synergistic effects.

(i) MOF/COF-based hybrid nanomaterials possess increased specific surface areas, large pores, and smaller band gaps. The properties of increased specific surface area and large pores favor the absorption of different types of pollutants, biomolecules (*i.e.*, aptamer and antibody), anticancer drugs, and gas molecules. Besides, the smaller band bap increases the absorption of visible light, while the interface of the heterostructure enhances the transportation and separation of photogenerated charge and holes. Therefore, MOF/COF-based hybrid nanomaterials present intensive applications in photocatalysis, sorption or separation, molecular recognition, and drug delivery.

(ii) The integration of MOF and COF components can complement each other. For example, MOFs usually demonstrate poor stability due to their reversible coordination bond in water and other physiological environments, while COFs are more stable because of their strong covalent bond. Therefore, the hybridization of MOFs and COFs results in increased stability in water and other physiological environments. Also, by combining with conductive COFs, the electrochemical properties of MOF/COF-based hybrids such as electrochemical catalytic ability and electrochemical sensing ability can be improved.

(iii) Excellent synergistic properties are introduced, such as irregular morphologies, micro-and mesopores at the MOF/COF interface, and strong multi-emission property. The synergism of different components in MOF/COF-based composites is of great significance for the improvement of their application-related performances, such as irregular morphology for catalytic selectivity, gas sieving, ratiometric sensing, and enhanced drug delivery and cancer synergistic therapy.

Most pristine MOF/COF-based heterostructures exhibit potential applications in gas separation/adsorption, biosensing and biomedical fields, photocatalysis, and molecular catalysis. However, research on these materials is still in its infancy and needs to be expanded and improved.

(i) Together with the development of the state-of-art of hybrid materials, fabricating ternary or even multicomponent MOF/COF-based heterostructures is urgent for their diverse applications in the near future. Therefore, to overcome the inherent restrictions of structures, new construction approaches and formation mechanisms should be proposed.

(ii) It is a great challenge to explain the functions of each component since the structure–function relationship of hybrids become more sophisticated. Complicated experiments are usually required; thus, computational simulation can give scope to reduce the amount of work and help explain the specific mechanism in complicated applications.

(iii) Although the performances of MOF/COF hybrids are enhanced, their applications in diverse scopes such as catalysis, energy storage, and cancer diagnosis and therapy are greatly restricted due to their low content of catalytic sites, absence of excellent electrochemical activity, and complicated preparation procedures. Thus, it is still urgent to explore new types of MOF-on-MOF, MOF@COF, and COF-to-COF heterostructures with remarkable electroconductivity and superior catalytic activity. The combination of MOF/COF hybrids with the currently active frontier of single-atom catalysts (SACs) is a promising field.

Together with the development of synthetic chemistry, MOFs or COFs with diverse structures and functionality will be proliferated, leading to the booming development of MOF/COF-based heterostructures. The fast-emerging synthetic strategies also pave the way for the rational design and synthesis of novel MOF/COF-based heterostructures, showing great potential for expanding the practical application of MOF materials.

Conflicts of interest

There are no conflicts to declare.

Acknowledgements

We are grateful to Henan Distinguished Youth Science Fund Project (202300410492), the National Natural Science Foundation of China (21571158) and the Key Research Project of University of Henan Province (19zx004) for financial support.

Notes and references

1 X. Zhang, Z. Chen, X. Liu, S. L. Hanna, X. Wang, R. Taheri-Ledari, A. Maleki, P. Li and O. K. Farha, *Chem. Soc. Rev.*, 2020, **49**, 7406–7427.
2 X. Kang, X. Han, C. Yuan, C. Cheng, Y. Liu and Y. Cui, *J. Am. Chem. Soc.*, 2020, **142**, 16346–16356.
3 P. M. Bhatt, V. Guillerm, S. J. Datta, A. Shkurenko and M. Eddaoudi, *Chem*, 2020, **6**, 1613–1633.
4 S. Wang, C. M. McGuirk, A. D'Aquino, J. A. Mason and C. A. Mirkin, *Adv. Mater.*, 2018, **30**, 1800202.
5 Y. Xue, S. Zheng, H. Xue and H. Pang, *J. Mater. Chem. A*, 2019, **7**, 7301–7327.
6 Y. Zheng, S. Zheng, H. Xue and H. Pang, *J. Mater. Chem. A*, 2019, **7**, 3469–3491.
7 S. Kuyuldar, D. T. Genna and C. Burda, *J. Mater. Chem. A*, 2019, **7**, 21545–21576.
8 S. Zhang, F. Rong, C. Guo, F. Duan, L. He, M. Wang, Z. Zhang, M. Kang and M. Du, *Coord. Chem. Rev.*, 2021, **439**, 213948.
9 U. Ryu, S. Jee, P. C. Rao, J. Shin, C. Ko, M. Yoon, K. S. Park and K. M. Choi, *Coord. Chem. Rev.*, 2021, **426**, 213544.
10 Q. Yang, M. Luo, K. Liu, H. Cao and H. Yan, *Appl. Catal., B*, 2020, **276**, 119174.
11 T. Sick, J. M. Rotter, S. Reuter, S. Kandambeth, N. N. Bach, M. Döblinger, J. Merz, T. Clark, T. B. Marder, T. Bein and D. D. Medina, *J. Am. Chem. Soc.*, 2019, **141**, 12570–12581.
12 H. Ma, J. Zou, X. Li, G. Chen and Y. Dong, *Chem.–Eur. J.*, 2020, **26**, 13754–13770.
13 L. Feng, C. Qian and Y. Zhao, *ACS Mater. Lett.*, 2020, **2**, 1074–1092.
14 J. Li, X. Jing, Q. Li, S. Li, X. Gao, X. Feng and B. Wang, *Chem. Soc. Rev.*, 2020, **49**, 3565–3604.
15 X. Cui, S. Lei, A. C. Wang, L. Gao, Q. Zhang, Y. Yang and Z. Lin, *Nano Energy*, 2020, **70**, 104525.
16 Z. Chen, X. Li, C. Yang, K. Cheng, T. Tan, Y. Lv and Y. Liu, *Adv. Sci.*, 2021, **8**, 2101883.
17 L. Garzón Tovar, J. Pérez Carvajal, A. Yazdi, J. Hernández Muñoz, P. Tarazona, I. Imaz, F. Zamora and D. Maspoch, *Angew. Chem. Int. Ed.*, 2019, **58**, 9512–9516.
18 J. Ren, N. M. Musyoka, H. W. Langmi, B. C. North, M. Mathe and X. Kang, *Int. J. Hydrogen Energy*, 2014, **39**, 14912–14917.
19 M. Du, Q. Li, Y. Zhao, C. Liu and H. Pang, *Coord. Chem. Rev.*, 2020, **416**, 213341.
20 L. Chen, X. Zhang, X. Cheng, Z. Xie, Q. Kuang and L. Zheng, *Nanoscale Adv.*, 2020, **2**, 2628–2647.
21 J. W. M. Osterrieth and D. Fairen-Jimenez, *Biotechnol. J.*, 2020, **16**, 2000005.
22 J. Xin, X. Wang, N. Li, L. Liu, Y. Lian, M. Wang and R. Zhao, *Food Chem.*, 2020, **330**, 127255.
23 D. Rodríguez-San-Miguel and F. Zamora, *Chem. Soc. Rev.*, 2019, **48**, 4375–4386.
24 R. Haldar and C. Wöll, *Nano Res.*, 2020, **14**, 355–368.
25 M. Wu, Y. Wang, G. Zhou and X. Liu, *Coord. Chem. Rev.*, 2021, **430**, 213735.
26 H. Zhang, C. Gu, M. Yao and S. Kitagawa, *Adv. Energy Mater.*, 2021, 2100321.
27 S. Subudhi, S. P. Tripathy and K. Parida, *Inorg. Chem. Front.*, 2021, **8**, 1619–1636.
28 X. Liao, H. Fu, T. Yan and J. Lei, *Biosens. Bioelectron.*, 2019, **146**, 111743.
29 X. Kong, H. Deng, F. Yan, J. Kim, J. A. Swisher, B. Smit, O. M. Yaghi and J. A. Reimer, *Science*, 2013, **341**, 882.
30 X. Yang, S. Yuan, L. Zou, H. Drake, Y. Zhang, J. Qin, A. Alsalme and H. Zhou, *Angew. Chem. Int. Ed.*, 2018, **57**, 3927–3932.
31 S. Furukawa, K. Hirai, K. Nakagawa, Y. Takashima, R. Matsuda, T. Tsuruoka, M. Kondo, R. Haruki, D. Tanaka, H. Sakamoto, S. Shimomura, O. Sakata and S. Kitagawa, *Angew. Chem. Int. Ed.*, 2009, **48**, 1766–1770.
32 G. Zhao, X. Xu, G. Zhu, J. Shi, Y. Li, S. Zhang, M. S. A. Hossain, K. C. W. Wu, J. Tang and Y. Yamauchi, *Microporous Mesoporous Mater.*, 2020, **303**, 110257.
33 H. Xu, L. Zhao, X. Liu, Q. Huang, Y. Wang, C. Hou, Y. Hou, J. Wang, F. Dang and J. Zhang, *Adv. Funct. Mater.*, 2020, **30**, 2006188.
34 Y. Pan, K. Sun, S. Liu, X. Cao, K. Wu, W. Cheong, Z. Chen, Y. Wang, Y. Li, Y. Liu, D. Wang, Q. Peng, C. Chen and Y. Li, *J. Am. Chem. Soc.*, 2018, **140**, 2610–2618.
35 O. Kwon, J. Y. Kim, S. Park, J. H. Lee, J. Ha, H. Park, H. R. Moon and J. Kim, *Nat. Commun.*, 2019, **10**, 3620.
36 M. Zhang, K. Yang, J. Cui, H. Yu, Y. Wang, W. Shan, Z. Lou and Y. Xiong, *Chem. Eng. J.*, 2020, **386**, 124023.
37 K. Koh, A. G. Wong-Foy and A. J. Matzger, *Chem. Commun.*, 2009, 6162–6164.
38 M. Wu, Y. Wang, G. Zhou and X. Liu, *ACS Appl. Mater. Interfaces*, 2020, **12**, 54285–54305.
39 V. Chernikova, O. Shekhah, I. Spanopoulos, P. N. Trikalitis and M. Eddaoudi, *Chem. Commun.*, 2017, **53**, 6191–6194.
40 K. Ikigaki, K. Okada, Y. Tokudome, T. Toyao, P. Falcaro, C. J. Doonan and M. Takahashi, *Angew. Chem. Int. Ed.*, 2019, **58**, 6886–6890.
41 M. Yao, J. Xiu, Q. Huang, W. Li, W. Wu, A. Wu, L. Cao, W. Deng, G. Wang and G. Xu, *Angew. Chem. Int. Ed.*, 2019, **58**, 14915–14919.
42 S. Choi, T. Kim, H. Ji, H. J. Lee and M. Oh, *J. Am. Chem. Soc.*, 2016, **138**, 14434–14440.
43 C. Wu, K. Zhang, H. Wang, Y. Fan, S. Zhang, S. He, F. Wang, Y. Tao, X. Zhao, Y. Zhang, Y. Ma, Y. Lee and T. Li, *J. Am. Chem. Soc.*, 2020, **142**, 18503–18512.
44 J. Zhuang, L. Chou, B. T. Sneed, Y. Cao, P. Hu, L. Feng and C. Tsung, *Small*, 2015, **11**, 5551–5555.

45 N. Zhou, F. Su, C. Guo, L. He, Z. Jia, M. Wang, Q. Jia, Z. Zhang and S. Lu, *Biosens. Bioelectron.*, 2019, **123**, 51–58.
46 M. Wang, M. Hu, Z. Li, L. He, Y. Song, Q. Jia, Z. Zhang and M. Du, *Biosens. Bioelectron.*, 2019, **142**, 111536.
47 H. J. Lee, Y. J. Cho, W. Cho and M. Oh, *ACS Nano*, 2013, **7**, 491–499.
48 H. Ji, S. Lee, J. Park, T. Kim, S. Choi and M. Oh, *Inorg. Chem.*, 2018, **57**, 9048–9054.
49 D. Kim, G. Lee, S. Oh and M. Oh, *Chem. Commun.*, 2019, **55**, 43–46.
50 G. Lee, S. Lee, S. Oh, D. Kim and M. Oh, *J. Am. Chem. Soc.*, 2020, **142**, 3042–3049.
51 S. Lee, S. Oh and M. Oh, *Angew. Chem. Int. Ed.*, 2020, **59**, 1327–1333.
52 X. Wang, L. Xu, M. Li and X. Zhang, *Angew. Chem. Int. Ed.*, 2020, **59**, 18078–18086.
53 W. Lee, H. Chien, Y. Lo, H. Chiu, T. Wang and D. Kang, *ACS Appl. Mater. Interfaces*, 2015, **7**, 18353–18361.
54 J. Zhang, T. Zhang, K. Xiao, S. Cheng, G. Qian, Y. Wang and Y. Feng, *Cryst. Growth Des.*, 2016, **16**, 6494–6498.
55 W. Guo, W. Xia, K. Cai, Y. Wu, B. Qiu, Z. Liang, C. Qu and R. Zou, *Small*, 2017, **13**, 1702049.
56 S. H. Yuan, A. P. Isfahani, T. Yamamoto, A. Muchtar, C. Y. Wu, G. Huang, Y. C. You, E. Sivaniah, B. K. Chang and B. Ghalei, *Small Methods*, 2020, **4**, 2000021.
57 K. C. Jayachandrababu, D. S. Sholl and S. Nair, *J. Am. Chem. Soc.*, 2017, **139**, 5906–5915.
58 Z. Song, F. Qiu, E. W. Zaia, Z. Wang, M. Kunz, J. Guo, M. Brady, B. Mi and J. J. Urban, *Nano Lett.*, 2017, **17**, 6752–6758.
59 L. Zhang, J. Wang, X. Ren, W. Zhang, T. Zhang, X. Liu, T. Du, T. Li and J. Wang, *J. Mater. Chem. A*, 2018, **6**, 21029–21038.
60 Y. Li, Y. Zhao, R. Zhang and G. Lu, *Inorg. Chem. Commun.*, 2017, **82**, 68–71.
61 H. Yi, R. Qin, S. Ding, Y. Wang, S. Li, Q. Zhao and F. Pan, *Adv. Funct. Mater.*, 2020, **31**, 2006970.
62 D. Wang, J. Zhou, R. Shi, H. Wu, R. Chen, B. Duan, G. Xia, P. Xu, H. Wang, S. Zhou, C. Wang, H. Wang, Z. Guo and Q. Chen, *Theranostics*, 2017, **7**, 4605–4617.
63 S. Wu, G. Zhuang, J. Wei, Z. Zhuang and Y. Yu, *J. Mater. Chem. A*, 2018, **6**, 18234–18241.
64 Y. Luo, J. Li, X. Liu, L. Tan, Z. Cui, X. Feng, X. Yang, Y. Liang, Z. Li, S. Zhu, Y. Zheng, K. W. K. Yeung, C. Yang, X. Wang and S. Wu, *ACS Cent. Sci.*, 2019, **5**, 1591–1601.
65 C. Li, X. Zhang, S. Wen, R. Xiang, Y. Han, W. Tang, T. Yue and Z. Li, *J. Hazard. Mater.*, 2020, **395**, 122615.
66 K. M. Choi, J. H. Park and J. K. Kang, *Chem. Mater.*, 2015, **27**, 5088–5093.
67 Y. Gong, Y. Yuan, C. Chen, P. Zhang, J. Wang, A. Khan, S. Zhuiykov, S. Chaemchuen and F. Verpoort, *J. Catal.*, 2019, **375**, 371–379.
68 M. Zhao, J. Chen, B. Chen, X. Zhang, Z. Shi, Z. Liu, Q. Ma, Y. Peng, C. Tan, X. Wu and H. Zhang, *J. Am. Chem. Soc.*, 2020, **142**, 8953–8961.
69 C. Liu, L. Lin, Q. Sun, J. Wang, R. Huang, W. Chen, S. Li, J. Wan, J. Zou and C. Yu, *Chem. Sci.*, 2020, **11**, 3680–3686.
70 Y. Gu, Y. Wu, L. Li, W. Chen, F. Li and S. Kitagawa, *Angew. Chem. Int. Ed.*, 2017, **56**, 15658–15662.
71 M. Gao, M. Qi, L. Liu and Z. Han, *Chem. Commun.*, 2019, **55**, 6377–6380.
72 H. Peng, J. Raya, F. Richard, W. Baaziz, O. Ersen, A. Ciesielski and P. Samorì, *Angew. Chem. Int. Ed.*, 2020, **59**, 19602–19609.
73 F. Li, D. Wang, Q. Xing, G. Zhou, S. Liu, Y. Li, L. Zheng, P. Ye and J. Zou, *Appl. Catal., B*, 2019, **243**, 621–628.
74 Y. Peng, M. Zhao, B. Chen, Z. Zhang, Y. Huang, F. Dai, Z. Lai, X. Cui, C. Tan and H. Zhang, *Adv. Mater.*, 2018, **30**, 1705454.
75 J. Winarta, B. Shan, S. M. Mcintyre, L. Ye, C. Wang, J. Liu and B. Mu, *Cryst. Growth Des.*, 2020, **20**, 1347–1362.
76 H. Tang, X. Sun and F. Zhang, *Dalton Trans.*, 2020, **49**, 12136–12144.
77 X. Zheng, L. Wang, Q. Pei, S. He, S. Liu and Z. Xie, *Chem. Mater.*, 2017, **29**, 2374–2381.
78 Y. Cheng, Y. Ying, L. Zhai, G. Liu, J. Dong, Y. Wang, M. P. Christopher, S. Long, Y. Wang and D. Zhao, *J. Membr. Sci.*, 2019, **573**, 97–106.
79 M. Qi, M. Gao, L. Liu and Z. Han, *Inorg. Chem.*, 2018, **57**, 14467–14470.
80 X. Wang, H. Yin and X. Yin, *ACS Appl. Mater. Interfaces*, 2020, **12**, 20973–20981.
81 Y. Chen, D. Yang, B. Shi, W. Dai, H. Ren, K. An, Z. Zhou, Z. Zhao, W. Wang and Z. Jiang, *J. Mater. Chem. A*, 2020, **8**, 7724–7732.
82 X. Zheng, L. Wang, Y. Guan, Q. Pei, J. Jiang and Z. Xie, *Biomaterials*, 2020, **235**, 119792.
83 J. L. Segura, S. Royuela and M. Mar Ramos, *Chem. Soc. Rev.*, 2019, **48**, 3903–3945.
84 Y. Zhu, W. D. Wang, X. Sun, M. Fan, X. Hu and Z. Dong, *ACS Appl. Mater. Interfaces*, 2020, **12**, 7285–7294.
85 D. Sun and D. Kim, *ACS Appl. Mater. Interfaces*, 2020, **12**, 20589–20595.
86 J. Zhu, P. Li, W. Guo, Y. Zhao and R. Zou, *Coord. Chem. Rev.*, 2018, **359**, 80–101.
87 Y. Yan, C. Li, Y. Wu, J. Gao and Q. Zhang, *J. Mater. Chem. A*, 2020, **8**, 15245–15270.
88 D. Sun, S. Jang, S. Yim, L. Ye and D. Kim, *Adv. Funct. Mater.*, 2018, **28**, 1707110.
89 S. He, Q. Rong, H. Niu and Y. Cai, *Appl. Catal., B*, 2019, **247**, 49–56.
90 M. Cai, Y. Li, Q. Liu, Z. Xue, H. Wang, Y. Fan, K. Zhu, Z. Ke, C. Su and G. Li, *Adv. Sci.*, 2019, **6**, 1802365.
91 L. Zhang, Z. Liu, Q. Deng, Y. Sang, K. Dong, J. Ren and X. Qu, *Angew. Chem. Int. Ed.*, 2021, **60**, 3469–3474.
92 S. Lv, J. Liu, F. Yang, C. Li and S. Wang, *Chem. Eng. J.*, 2021, **409**, 128269.
93 J. Fu, S. Das, G. Xing, T. Ben, V. Valtchev and S. Qiu, *J. Am. Chem. Soc.*, 2016, **138**, 7673–7680.
94 X. Liu, M. Hu, M. Wang, Y. Song, N. Zhou, L. He and Z. Zhang, *Biosens. Bioelectron.*, 2019, **123**, 59–68.
95 N. Zhou, Y. Ma, B. Hu, L. He, S. Wang, Z. Zhang and S. Lu, *Biosens. Bioelectron.*, 2019, **127**, 92–100.

96 H. Fan, A. Mundstock, A. Feldhoff, A. Knebel, J. Gu, H. Meng and J. Caro, *J. Am. Chem. Soc.*, 2018, **140**, 10094–10098.
97 Y. Ying, M. Tong, S. Ning, S. K. Ravi, S. B. Peh, S. C. Tan, S. J. Pennycook and D. Zhao, *J. Am. Chem. Soc.*, 2020, **142**, 4472–4480.
98 H. Xu, Y. Yang, X. Yang, J. Cao, W. Liu and Y. Tang, *J. Mater. Chem. A*, 2019, **7**, 8284–8291.
99 J. Ha and H. R. Moon, *CrystEngComm*, 2021, **23**, 2337–2354.
100 J. Tang, R. R. Salunkhe, J. Liu, N. L. Torad, M. Imura, S. Furukawa and Y. Yamauchi, *J. Am. Chem. Soc.*, 2015, **137**, 1572–1580.
101 Y. Pan, K. Sun, S. Liu, X. Cao, K. Wu, W. Cheong, Z. Chen, Y. Wang, Y. Li, Y. Liu, D. Wang, Q. Peng, C. Chen and Y. Li, *J. Am. Chem. Soc.*, 2018, **140**, 2610–2618.
102 Z. Hu, Z. Zhang, Z. Li, M. Dou and F. Wang, *ACS Appl. Mater. Interfaces*, 2017, **9**, 16109–16116.
103 H. Park, S. Oh, S. Lee, S. Choi and M. Oh, *Appl. Catal., B*, 2019, **246**, 322–329.
104 M. Huang, K. Mi, J. Zhang, H. Liu, T. Yu, A. Yuan, Q. Kong and S. Xiong, *J. Mater. Chem. A*, 2017, **5**, 266–274.
105 J. Yang, F. Zhang, H. Lu, X. Hong, H. Jiang, Y. Wu and Y. Li, *Angew. Chem. Int. Ed.*, 2015, **54**, 10889–10893.
106 Y. Huang, X. Sun, S. Huo, Y. Li and C. Zhong, *Appl. Surf. Sci.*, 2019, **466**, 637–646.
107 G. Zhan and H. C. Zeng, *Nat. Commun.*, 2018, **9**, 3778.
108 M. Pan, Y. Zhu, K. Wu, L. Chen, Y. Hou, S. Yin, H. Wang, Y. Fan and C. Su, *Angew. Chem. Int. Ed.*, 2017, **56**, 14582–14586.
109 A. L. Medina-Castillo, J. F. Fernández-Sánchez and A. Fernández-Gutiérrez, *Adv. Funct. Mater.*, 2011, **21**, 3488–3495.
110 S. A. A. Razavi and A. Morsali, *Chem.–Eur. J.*, 2019, **25**, 10876–10885.
111 J. A. Boissonnault, A. G. Wong-Foy and A. J. Matzger, *J. Am. Chem. Soc.*, 2017, **139**, 14841–14844.
112 C. Guo, J. Guo, Y. Zhang, D. Wang, L. Zhang, Y. Guo, W. Ma and J. Wang, *CrystEngComm*, 2018, **20**, 7659–7665.
113 X. Song, T. K. Kim, H. Kim, D. Kim, S. Jeong, H. R. Moon and M. S. Lah, *Chem. Mater.*, 2012, **24**, 3065–3073.
114 R. Lin, B. Villacorta Hernandez, L. Ge and Z. Zhu, *J. Mater. Chem. A*, 2018, **6**, 293–312.
115 F. Zhang, J. Sheng, Z. Yang, X. Sun, H. Tang, M. Lu, H. Dong, F. Shen, J. Liu and Y. Lan, *Angew. Chem. Int. Ed.*, 2018, **57**, 12106–12110.
116 H. L. Nguyen, F. Gándara, H. Furukawa, T. L. H. Doan, K. E. Cordova and O. M. Yaghi, *J. Am. Chem. Soc.*, 2016, **138**, 4330–4333.
117 L. Feng, K. Wang, X. Lv, T. Yan, J. Li and H. Zhou, *J. Am. Chem. Soc.*, 2020, **142**, 3069–3076.
118 W. Sun, X. Tang, Q. Yang, Y. Xu, F. Wu, S. Guo, Y. Zhang, M. Wu and Y. Wang, *Adv. Mater.*, 2019, **31**, 1903176.
119 F. Song, W. Li and Y. Sun, *Inorganics*, 2017, **5**, 40.
120 Y. Fu, G. Zeng, C. Lai, D. Huang, L. Qin, H. Yi, X. Liu, M. Zhang, B. Li, S. Liu, L. Li, M. Li, W. Wang, Y. Zhang and Z. Pi, *Chem. Eng. J.*, 2020, **399**, 125743.
121 Y. Li, M. Zhou, B. Cheng and Y. Shao, *J. Mater. Sci. Technol.*, 2020, **56**, 1–17.
122 X. Liu, S. Gu, Y. Zhao, G. Zhou and W. Li, *J. Mater. Sci. Technol.*, 2020, **56**, 45–68.
123 B. Gui, Y. Meng, Y. Xie, J. Tian, G. Yu, W. Zeng, G. Zhang, S. Gong, C. Yang, D. Zhang and C. Wang, *Adv. Mater.*, 2018, **30**, 1802329.
124 X. Huang, T. Shen, T. Zhang, H. Qiu, X. Gu, Z. Ali and Y. Hou, *Adv. Energy Mater.*, 2020, **10**, 1900375.
125 C. Lin, D. Zhang, Z. Zhao and Z. Xia, *Adv. Mater.*, 2018, **30**, 1703646.
126 X. Feng, X. Ding and D. Jiang, *Chem. Soc. Rev.*, 2012, **41**, 6010–6022.
127 G. Lu, X. Huang, Y. Li, G. Zhao, G. Pang and G. Wang, *J. Energy Chem.*, 2020, **43**, 8–15.
128 M. Fatima, R. Farooq, R. W. Lindström and M. Saeed, *J. Mol. Liq.*, 2017, **246**, 275–281.
129 V. Vaiano, O. Sacco, D. Sannino and P. Ciambelli, *Chem. Eng. J.*, 2015, **261**, 3–8.
130 Y. A. Attia, D. Buceta, C. Blanco-Varela, M. B. Mohamed, G. Barone and M. A. López-Quintela, *J. Am. Chem. Soc.*, 2014, **136**, 1182–1185.
131 D. Bahnemann, *Sol. Energy*, 2004, **77**, 445–459.
132 X. Yang, Z. Chen, W. Zhao, C. Liu, X. Qian, M. Zhang, G. Wei, E. Khan, Y. Hau Ng and Y. Sik Ok, *Chem. Eng. J.*, 2021, **405**, 126806.
133 Z. He, J. Zhang, X. Li, S. Guan, M. Dai and S. Wang, *Small*, 2020, **16**, 2005051.
134 Y. Liu, D. Huang, M. Cheng, Z. Liu, C. Lai, C. Zhang, C. Zhou, W. Xiong, L. Qin, B. Shao and Q. Liang, *Coord. Chem. Rev.*, 2020, **409**, 213220.
135 C. Wang, X. Wang and W. Liu, *Chem. Eng. J.*, 2020, **391**, 123601.
136 N. Askari, M. Beheshti, D. Mowla and M. Farhadian, *Chemosphere*, 2020, **251**, 126453.
137 L. Zhang, L. Feng, P. Li, X. Chen, J. Jiang, S. Zhang, C. Zhang, A. Zhang, G. Chen and H. Wang, *Chem. Eng. J.*, 2020, **395**, 125072.
138 S. S. Chen, C. Hu, C. Liu, Y. Chen, T. Ahamad, S. M. Alshehri, P. Huang and K. C. W. Wu, *J. Hazard. Mater.*, 2020, **397**, 122431.
139 W. Li, J. Cao, W. Xiong, Z. Yang, S. Sun, M. Jia and Z. Xu, *Chem. Eng. J.*, 2020, **392**, 124844.
140 Q. Wu, H. Yang, L. Kang, Z. Gao and F. Ren, *Appl. Catal., B*, 2020, **263**, 118282.
141 R. Yin, Y. Chen, S. He, W. Li, L. Zeng, W. Guo and M. Zhu, *J. Hazard. Mater.*, 2020, **388**, 121996.
142 X. Yang, C. Chen, Y. Zhang, L. Cai, B. Tan and J. Zhang, *Dalton Trans.*, 2016, **45**, 4522–4527.
143 M. Jaishankar, T. Tseten, N. Anbalagan, B. B. Mathew and K. N. Beeregowda, *Interdiscipl. Toxicol.*, 2014, **7**, 60–72.
144 J. Liu, F. Yang, Q. Zhang, W. Chen, Y. Gu and Q. Chen, *Inorg. Chem.*, 2019, **58**, 3564–3568.
145 M. Firoozi, Z. Rafiee and K. Dashtian, *ACS Omega*, 2020, **5**, 9420–9428.
146 M. A. Islam, M. J. Angove and D. W. Morton, *J. Environ. Nanotechnol.*, 2019, **12**, 100267.

147 A. Tkaczyk, K. Mitrowska and A. Posyniak, *Sci. Total Environ.*, 2020, **717**, 137222.
148 A. Ahmad, S. H. Mohd-Setapar, C. S. Chuong, A. Khatoon, W. A. Wani, R. Kumar and M. Rafatullah, *RSC Adv.*, 2015, **5**, 30801–30818.
149 Y. Tong, G. Xue, H. Wang, M. Liu, J. Wang, C. Hao, X. Zhang, D. Wang, X. Shi, W. Liu, G. Li and Z. Tang, *Nanoscale*, 2018, **10**, 16425–16430.
150 S. Cho, B. Ma, S. T. Nguyen, J. T. Hupp and T. E. Albrecht-Schmitt, *Chem. Commun.*, 2006, 2563–2565.
151 S. Huber, M. Cokoja and F. E. Kühn, *J. Organomet. Chem.*, 2014, **751**, 25–32.
152 M. P. van der Helm, B. Klemm and R. Eelkema, *Nat. Rev. Chem.*, 2019, **3**, 491–508.
153 Y. Zhong, Z. Pan, X. Wang, J. Yang, Y. Qiu, S. Xu, Y. Lu, Q. Huang and W. Li, *Adv. Sci.*, 2019, **6**, 1802243.
154 D. Sun, L. Ye and Z. Li, *Appl. Catal., B*, 2015, **164**, 428–432.
155 F. Dawood, M. Anda and G. M. Shafiullah, *Int. J. Hydrogen Energy*, 2020, **45**, 3847–3869.
156 Y. Liu, D. Liu, Q. Yang, C. Zhong and J. Mi, *Ind. Eng. Chem. Res.*, 2010, **49**, 2902–2906.
157 P. Á. Szilágyi, M. Lutz, J. Gascon, J. Juan-Alcañiz, J. van Esch, F. Kapteijn, H. Geerlings, B. Dam and R. van de Krol, *CrystEngComm*, 2013, **15**, 6003–6008.
158 D. K. Panchariya, R. K. Rai, E. Anil Kumar and S. K. Singh, *ACS Omega*, 2018, **3**, 167–175.
159 Y. Wang, X. Zhao, H. Yang, X. Bu, Y. Wang, X. Jia, J. Li and P. Feng, *Angew. Chem. Int. Ed.*, 2019, **58**, 6316–6320.
160 J. Park, N. F. Attia, M. Jung, M. E. Lee, K. Lee, J. Chung and H. Oh, *Energy*, 2018, **158**, 9–16.
161 S. Yousef, J. Šereika, A. Tonkonogovas, T. Hashem and A. Mohamed, *Environ. Technol. Innovation*, 2021, **21**, 101339.
162 Y. He, M. Sun, Q. Zhao, J. Shang, Y. Tian, P. Xiao, Q. Gu, L. Li and P. A. Webley, *ACS Appl. Mater. Interfaces*, 2019, **11**, 30234–30239.
163 J. Gao, X. Qian, R. Lin, R. Krishna, H. Wu, W. Zhou and B. Chen, *Angew. Chem. Int. Ed.*, 2020, **59**, 4396–4400.
164 S. Dong, L. Peng, W. Wei and T. Huang, *ACS Appl. Mater. Interfaces*, 2018, **10**, 14665–14672.
165 Q. Zhu, W. Zhang, H. Zhang, R. Yuan and H. He, *J. Mater. Chem. C*, 2020, **8**, 16984–16991.
166 J. Lei, R. Qian, P. Ling, L. Cui and H. Ju, *TrAC, Trends Anal. Chem.*, 2014, **58**, 71–78.
167 J. Zhou, Y. Li, W. Wang, X. Tan, Z. Lu and H. Han, *Biosens. Bioelectron.*, 2020, **164**, 112332.
168 H. Liang, M. Xu, Y. Zhu, L. Wang, Y. Xie, Y. Song and L. Wang, *ACS Appl. Nano Mater.*, 2020, **3**, 555–562.
169 M. Ko, L. Mendecki, A. M. Eagleton, C. G. Durbin, R. M. Stolz, Z. Meng and K. A. Mirica, *J. Am. Chem. Soc.*, 2020, **142**, 11717–11733.
170 S. Liu, J. Bai, Y. Huo, B. Ning, Y. Peng, S. Li, D. Han, W. Kang and Z. Gao, *Biosens. Bioelectron.*, 2020, **149**, 111801.
171 X. Qiao, B. Su, C. Liu, Q. Song, D. Luo, G. Mo and T. Wang, *Adv. Mater.*, 2018, **30**, 1702275.
172 Y. Peng, H. Huang, Y. Zhang, C. Kang, S. Chen, L. Song, D. Liu and C. Zhong, *Nat. Commun.*, 2018, **9**, 187.
173 S. Dong, D. Zhang, H. Cui and T. Huang, *Sens. Actuators, B*, 2019, **284**, 354–361.
174 C. Gu, C. Guo, Z. Li, M. Wang, N. Zhou, L. He, Z. Zhang and M. Du, *Biosens. Bioelectron.*, 2019, **134**, 8–15.
175 L. Yao, F. Yang, G. Hu, Y. Yang, W. Huang, W. Liang, R. Yuan and D. Xiao, *Biosens. Bioelectron.*, 2020, **155**, 112099.
176 M. Wang, M. Hu, J. Liu, C. Guo, D. Peng, Q. Jia, L. He, Z. Zhang and M. Du, *Biosens. Bioelectron.*, 2019, **132**, 8–16.
177 A. Afzalinia and M. Mirzaee, *ACS Appl. Mater. Interfaces*, 2020, **12**, 16076–16087.
178 H. Tan, X. Wu, Y. Weng, Y. Lu and Z. Huang, *Anal. Chem.*, 2020, **92**, 3447–3454.
179 L. He, F. Duan, Y. Song, C. Guo, H. Zhao, J. Tian, Z. Zhang, C. Liu, X. Zhang, P. Wang, M. Du and S. Fang, *2D Materials*, 2017, **4**, 25098.
180 S. Khatua, S. Goswami, S. Biswas, K. Tomar, H. S. Jena and S. Konar, *Chem. Mater.*, 2015, **27**, 5349–5360.
181 Y. H. Cheng, D. Barpaga, J. A. Soltis, V. Shutthanandan, R. Kargupta, K. S. Han, B. P. McGrail, R. K. Motkuri, S. Basuray and S. Chatterjee, *ACS Appl. Mater. Interfaces*, 2020, **12**, 10503–10514.
182 A. Yousefzadeh, J. Hassanzadeh, S. M. J. Mousavi and M. Yousefzadeh, *Sens. Actuators, B*, 2019, **286**, 154–162.
183 X. Kuang, S. Ye, X. Li, Y. Ma, C. Zhang and B. Tang, *Chem. Commun.*, 2016, **52**, 5432–5435.
184 Y. Wang, L. Wang, W. Huang, T. Zhang, X. Hu, J. A. Perman and S. Ma, *J. Mater. Chem. A*, 2017, **5**, 8385–8393.
185 X. Yang, Y. Yu, L. Peng, Y. Lei, Y. Chai, R. Yuan and Y. Zhuo, *Anal. Chem.*, 2018, **90**, 3995–4002.
186 F. Wang, X. Chen, L. Chen, J. Yang and Q. Wang, *Mater. Sci. Eng. C*, 2019, **96**, 41–50.
187 D. Zou, L. Yu, Q. Sun, Y. Hui, Tengjisi, Y. Liu, G. Yang, D. Wibowo and C. Zhao, *Colloids Surf., B*, 2020, **193**, 111108.
188 M. Ding, R. W. Flaig, H. Jiang and O. M. Yaghi, *Chem. Soc. Rev.*, 2019, **48**, 2783–2828.
189 M. Lu, Y. Deng, Y. Li, T. Li, J. Xu, S. Chen and J. Wang, *Anal. Chim. Acta*, 2020, **1110**, 35–43.
190 Z. Zhang, F. Duan, J. Tian, J. He, L. Yang, H. Zhao, S. Zhang, C. Liu, L. He, M. Chen, D. Chen and M. Du, *ACS Sens.*, 2017, **2**, 982–989.
191 Y. Seok Kim, N. H. Ahmad Raston and M. Bock Gu, *Biosens. Bioelectron.*, 2016, **76**, 2–19.
192 N. Zhou, L. Yang, B. Hu, Y. Song, L. He, W. Chen, Z. Zhang, Z. Liu and S. Lu, *Anal. Chem.*, 2018, **90**, 13624–13631.
193 F. Duan, M. Hu, C. Guo, Y. Song, M. Wang, L. He, Z. Zhang, R. Pettinari and L. Zhou, *Chem. Eng. J.*, 2020, **398**, 125452.
194 P. Sun, J. Hai, S. Sun, S. Lu, S. Liu, H. Liu, F. Chen and B. Wang, *Nanoscale*, 2020, **12**, 825–831.
195 P. Vineis and C. P. Wild, *The Lancet*, 2014, **383**, 549–557.
196 A. Pandey, N. Dhas, P. Deshmukh, C. Caro, P. Patil, M. Luisa García-Martín, B. Padya, A. Nikam, T. Mehta and S. Mutalik, *Coord. Chem. Rev.*, 2020, **409**, 213212.
197 J. Feng, W. Ren, F. Kong and Y. Dong, *Inorg. Chem. Front.*, 2021, **8**, 848–879.

198 Y. Wang, X. Liu, W. Wu, D. Mao, B. Wang, G. Tang and B. Liu, *Adv. Ther.*, 2020, **3**, 2000011.
199 Y. Weng, S. Guan, L. Wang, H. Lu, X. Meng, G. I. N. Waterhouse and S. Zhou, *Small*, 2020, **16**, 1905184.
200 B. Yang, L. Ding, H. Yao, Y. Chen and J. Shi, *Adv. Mater.*, 2020, **32**, 1907152.
201 W. Shang, L. Peng, P. Guo, H. Hui, X. Yang and J. Tian, *ACS Biomater. Sci. Eng.*, 2020, **6**, 1008–1016.
202 D. Zhang, Z. Ye, L. Wei, H. Luo and L. Xiao, *ACS Appl. Mater. Interfaces*, 2019, **11**, 39594–39602.
203 J. Lu, L. Yang, W. Zhang, P. Li, X. Gao, W. Zhang, H. Wang and B. Tang, *Chem. Commun.*, 2019, **55**, 10792–10795.
204 Y. Zhang, H. Fu, S. Chen, B. Liu, W. Sun and H. Gao, *Chem. Commun.*, 2020, **56**, 762–765.
205 Z. Deng, C. Fang, X. Ma, X. Li, Y. Zeng and X. Peng, *ACS Appl. Mater. Interfaces*, 2020, **12**, 20321–20330.
206 L. Zhang, Y. Gao, S. Sun, Z. Li, A. Wu and L. Zeng, *J. Mater. Chem. B*, 2020, **8**, 1739–1747.
207 L. He, Q. Ni, J. Mu, W. Fan, L. Liu, Z. Wang, L. Li, W. Tang, Y. Liu, Y. Cheng, L. Tang, Z. Yang, Y. Liu, J. Zou, W. Yang, O. Jacobson, F. Zhang, P. Huang and X. Chen, *J. Am. Chem. Soc.*, 2020, **142**, 6822–6832.
208 Y. Shao, B. Liu, Z. Di, G. Zhang, L. Sun, L. Li and C. Yan, *J. Am. Chem. Soc.*, 2020, **142**, 3939–3946.
209 L. Wang, X. Qu, Y. Zhao, Y. Weng, G. I. N. Waterhouse, H. Yan, S. Guan and S. Zhou, *ACS Appl. Mater. Interfaces*, 2019, **11**, 35228–35237.
210 Z. Cai, F. Xin, Z. Wei, M. Wu, X. Lin, X. Du, G. Chen, D. Zhang, Z. Zhang, X. Liu and C. Yao, *Adv. Healthcare Mater.*, 2020, **9**, 1900996.
211 Q. Fang, J. Wang, S. Gu, R. B. Kaspar, Z. Zhuang, J. Zheng, H. Guo, S. Qiu and Y. Yan, *J. Am. Chem. Soc.*, 2015, **137**, 8352–8355.
212 K. Zhao, P. Gong, J. Huang, Y. Huang, D. Wang, J. Peng, D. Shen, X. Zheng, J. You and Z. Liu, *Microporous Mesoporous Mater.*, 2021, **311**, 110713.
213 L. Bai, S. Z. F. Phua, W. Q. Lim, A. Jana, Z. Luo, H. P. Tham, L. Zhao, Q. Gao and Y. Zhao, *Chem. Commun.*, 2016, **52**, 4128–4131.
214 M. C. Scicluna and L. Vella-Zarb, *ACS Appl. Nano Mater.*, 2020, **3**, 3097–3115.
215 S. Liu, J. Yang, R. Guo, L. Deng, A. Dong and J. Zhang, *Macromol. Rapid Commun.*, 2020, **41**, 1900570.
216 S. Mitra, H. S. Sasmal, T. Kundu, S. Kandambeth, K. Illath, D. Díaz Díaz and R. Banerjee, *J. Am. Chem. Soc.*, 2017, **139**, 4513–4520.
217 G. Zhang, X. Li, Q. Liao, Y. Liu, K. Xi, W. Huang and X. Jia, *Nat. Commun.*, 2018, **9**, 2785.
218 P. Bhanja, S. Mishra, K. Manna, A. Mallick, K. Das Saha and A. Bhaumik, *ACS Appl. Mater. Interfaces*, 2017, **9**, 31411–31423.
219 H. Wang, W. Zhu, L. Feng, Q. Chen, Y. Chao, Z. Dong and Z. Liu, *Nano Res.*, 2018, **11**, 3244–3257.
220 Q. Guan, D. Fu, Y. Li, X. Kong, Z. Wei, W. Li, S. Zhang and Y. Dong, *iScience*, 2019, **14**, 180–198.
221 D. Tao, L. Feng, Y. Chao, C. Liang, X. Song, H. Wang, K. Yang and Z. Liu, *Adv. Funct. Mater.*, 2018, **28**, 1804901.
222 Q. Guan, L. Zhou, Y. Li, W. Li, S. Wang, C. Song and Y. Dong, *ACS Nano*, 2019, **13**, 13304–13316.
223 K. Wang, Z. Zhang, L. Lin, K. Hao, J. Chen, H. Tian and X. Chen, *ACS Appl. Mater. Interfaces*, 2019, **11**, 39503–39512.
224 Y. Shi, S. Liu, Y. Liu, C. Sun, M. Chang, X. Zhao, C. Hu and M. Pang, *ACS Appl. Mater. Interfaces*, 2019, **11**, 12321–12326.
225 K. Wang, Z. Zhang, L. Lin, J. Chen, K. Hao, H. Tian and X. Chen, *Chem. Mater.*, 2019, **31**, 3313–3323.
226 Z. Qin, Y. Li and N. Gu, *Adv. Healthcare Mater.*, 2018, **7**, 1800347.
227 D. Wang, J. Zhou, R. Chen, R. Shi, C. Wang, J. Lu, G. Zhao, G. Xia, S. Zhou, Z. Liu, H. Wang, Z. Guo and Q. Chen, *Chem. Mater.*, 2017, **29**, 3477–3489.
228 H. Guan, R. J. LeBlanc, S. Xie and Y. Yue, *Coord. Chem. Rev.*, 2018, **369**, 76–90.